October 2017

Smart Inverter Control and Operation for Distributed Energy Resources

Ahmad F. Tazay
University of South Florida, eng.a.tazay@hotmail.com

Smart Inverter Control and Operation for Distributed Energy Resources

by

Ahmad F. Tazay

A dissertation submitted in partial fulfillment
of the requirements for the degree of
Doctor of Philosophy
Department of Electrical Engineering
College of Engineering
University of South Florida

Major Professor: Zhixin Miao, Ph.D.
Lingling Fan, Ph.D.
Chung Seop Jeong, Ph.D.
Kaiqi Xiong, Ph.D.
Zhenyu Wang, Ph.D.

Date of Approval:
October 20, 2017

Keywords: Microgrid, Voltage Source Converter (VSC), Three-phase Hybrid Boost Converter (HBC), Droop Control, PV Charging Station

DEDICATION

I dedicate my dissertation work to my amazing parents, Fareed and Ghofran, for being the perfect parent role model, for their inspiration, continuous prayers, and belief in me. To my dear wife, Omniah, for being a perfect wife, the love of my life, being always optimistic, tolerating my excessive work and study times, and her unconditional love. I hope that you receive your degree soon. To my wonderful parents in law, Amin and Meme, for being cheerful and positive towards every decision I made. To my beautiful kids, Rawad and Rozana, for always making me smile and happy. You are my luminous future. To my lovely brothers and sister, Emad, Nader, Nezar, and Rasha, for their love, support, and understanding my situation.I love you all. You are the secret behind my success.

ACKNOWLEDGMENTS

I would like to express my deepest gratitude to my major advisor Dr. Zhixin Miao for supporting, encouraging, guidance, technical insight, and providing me with an excellent atmosphere to do research throughout the past four years. His incredible hard-working, trust in my abilities, and deep work reviews had a serious influence on my motivation and professional growth.

I would also like to thank Dr. Lingling Fan for providing me the necessary tools which were required to develop my research. I especially appreciate her great knowledge and experience, hard-working, patience, and great kindness and morality.

I would like to truly thank my committee members: Dr. Chung Seop Jeong, Dr. Kaiqi Xiong, and Dr. Zhenyu Wang, for their encouragement, constructive comments, reviewing my dissertation and participating in my dissertation.

I would also like to thank my recent colleagues from the smart grid power system lab Yan Ma, Yin Li, David Xu, Matthew Ma, Yi Zhou, Anas Almunif, Ibrahim Alsaleh, Abdullah Alburidy, Rabi Kar, Miao Zhang, Li Bao, Sulaiman Almutairi, Abdullah Alassaf, Tony Wang, and my former colleagues Dr. Mohemmed Alhaider, Dr. Hossein Aghamolki, Dr. Vahid Rasouli, Dr. Lakshan Piyasinghe, Dr. Javad Khazaei, for all the discussions, help and enjoyable time I spent with them. Special thanks go to my missing friend, Ayman Aldhmadi, who passed away before joining our lab. May Allah forgive him and his soul rest in peace.

I would also like to offer sincere thanks and gratitude to my family. I would like to thank my wife, Omniah Baghdady, my father, Fareed Tazay, my mother, Ghofran Mosatat, my father in law, Amin Baghdady, my mother in law, Meme Ghandorah,my brothers, Emad, Nader and Nezar, my sister, Rasha for all the encouragement, love and the support they provided from the beginning. I am truly grateful for their love and support.

TABLE OF CONTENTS

LIST OF TABLES

LIST OF FIGURES

ABSTRACT

The motivation of this research is to carry out the control and operation of smart inverters and voltage source converters (VSC) for distributed energy resources (DERs) such as photovoltaic (PV), battery, and plug-in hybrid electric vehicles (PHEV). The main contribution of the research includes solving a couple of issues for smart grids by controlling and implementing multifunctions of VSC and smart inverter as well as improving the operational scheme of the microgrid. The work is mainly focused on controlling and operating of smart inverter since it promises a new technology for the future microgrid. Two major applications of smart inverter will be investigated in this work based on the connection modes: microgrid at grid-tied mode and autonomous mode.

In grid-tied connection, the smart inverter and VSC are used to integrate DER such as Photovoltaic (PV) and battery to provide suitable power to the system by controlling the supplied real and reactive power. The role of a smart inverter at autonomous mode includes supplying a sufficient voltage and frequency, mitigate abnormal condition of the load as well as equally sharing the total load's power. However, the operational control of the microgrid still has a major issue on the operation of the microgrid. The dissertation is divided into two main sections which are:

- 1- Low-level control of a single smart Inverter.
- 2- High-level control of the microgrid.

The first part investigates a comprehensive research for a smart inverter and VSC technology at the two major connections of the microgrid. This involves controlling and modeling single smart inverter and VSC to solve specific issues of microgrid as well as improve the operation of the system. The research provides developed features for the smart inverter comparing with a conventional voltage sourced converter (VSC). The two main connections for a microgrid have been deeply investigated to analyze a better way to develop and improve the operational procedure of the microgrid as well as solve specific issues of connecting the microgrid to the system.

A detailed procedure for controlling VSC and designing an optimal operation of the controller is also covered in the first part of the dissertation. This section provides an optimal operation for controlling motor drive and demonstrates issues when motor load exists at an autonomous microgrid. It also provides a solution for specific issues at operating a microgrid at autonomous mode as well as improving the structural design for the grid-tied microgrid. The solution for autonomous microgrid includes changing the operational state of the switching pattern of the smart inverter to solve the issue of a common mode voltage (CMV) that appears across the motor load. It also solves the issue of power supplying to large loads, such as induction motors. The last section of the low-level section involves an improvement of the performance and operation of the PV charging station for a plug-in hybrid electric vehicle (PHEV) at grid-tied mode. This section provides a novel structure and smart controller for PV charging station using three-phase hybrid boost converter topology. It also provides a form of applications of a multifunction smart inverter using PV charging station.

The second part of the research is focusing on improving the performance of the microgrid by integrating several smart inverters to form a microgrid. It investigates the issue of connecting DER units with the microgrid at real applications. One of the common issues of the microgrid is the circulating current which is caused by poor reactive power sharing accuracy. When more than two DER units are connected in parallel, a microgrid is forming be generating required power for the load. When the microgrid is operated at autonomous mode, all DER units participate in generating voltage and frequency as well as share the load's power. This section provides a smart and novel controlling technique to solve the issue of unequal power sharing. The feature of the smart inverter is realized by the communication link between smart inverters and the main operator. The analysis and derivation of the problem are presented in this section.

The dissertation has led to two accepted conference papers, one accepted transaction IEEE manuscript, and one submitted IET transaction manuscript. The future work aims to improve the current work by investigating the performance of the smart inverter at real applications.

CHAPTER 1

INTRODUCTION

This chapter introduces the advantages of a smart inverter and microgrid technology as well as presents the main objectives of this research.

1.1 Background

Power electronics play an important role in operating and controlling the microgrid. Voltage sourced converter (VSC) is one of the commonly used power electronic devices that are recently implemented in a microgrid instead of conventional electronic devices such as thyristor-based line-commutated converters (LCC). The development in power electronics industry leads to increase the power capacity and response speed of Insulated-Gate Bipolar Transistors (IGBTs). The main benefits of using VSC instead of LCC is the implementing of IGBT components to control of switching patterns. Moreover, The IGBT based VSC is controlled by gate voltage which does not require an external circuit to turn off the device. Another advantage is the bidirectional power flow capability of VSC. The topology of VSC can be operated as dc/ac inverter and ac/dc converter based on the advanced configuration of the VSC. These advantages lead to implement VSC in several applications such as PV microgrid, high-voltage direct current (HVDC), flexible ac transmission systems (FACTS), Static Compensator (STATCOM), plug-in hybrid vehicle charging stations (PHEV), etc.

There are several topologies to represent IGBT based VSC device regarding the required power capacity of the module. For example, two-level PWM converter and three-level neutral-point clamp converter are the common topologies of VSC based on cost and efficiency aspects. It is worth to mention that IGBT has the capability to be connected in series to form a modular multilevel converter (MMC) which can be used at high-voltage applicants such as HVDC systems. In this

dissertation, the two-level three-phase bidirectional IGBT switches are implemented to represent a VSC converter. Fig. 1.1 shows a common topology of a three-phase tow-level IGBT based VSC converter. It is noticed from designing of IGBT switches that every VSC's switch has a reverse parallel diode. The key role of the diode is to achieve a bidirectional current flow without affecting the power rating of each VSC leg. This configuration allows VSC to be operated as a dc/ac inverter or an ac/dc converter without any topology change.

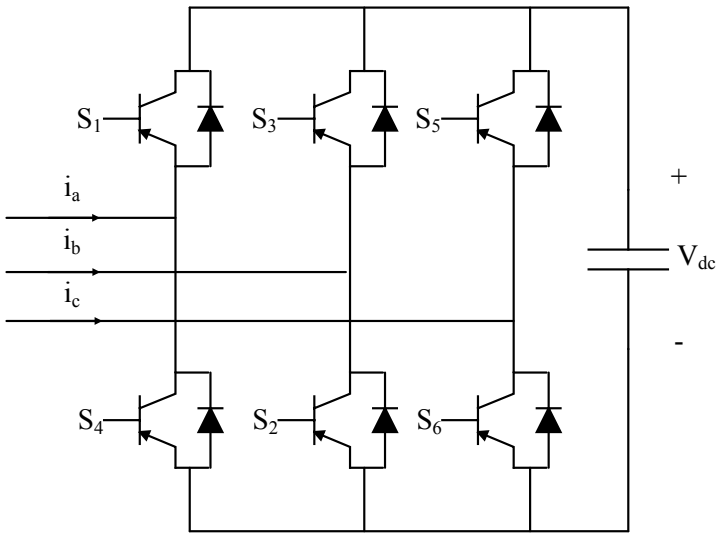

Figure 1.1. Configuration of a three-phase bidirectional VSC converter

1.1.1 Microgrid

The advanced feature and recent development of power electronic filed have convinced the electric industry to depend on distributed energy resources (DERs) to generate electric power on smart grid and microgrid. The leading action of integrating smart grid and microgrid into the main grid can solve most of the system's problems as well as improve the efficiency and reliability. The future of power systems will depend on generating electricity from the microgrid since it can supply sufficient power to its local load as well as share energy with the entire system.

Microgrid is a distributed network that provides controllable power and energy to the entire system by integrating DERs with the system and loads using power electronics technologies. These

main elements are electronically interfaced to provide controllable power, stable voltage, and steady frequency to the entire system. DER consists of Distributed Storages (DS) or a Distributed Generators (DG). Loads may include a combination of resistive, inductive and capacitive elements as well as distributed power storage equipment or motors. Generally, DG contains non-conventional and clean energy resources such as wind, solar photovoltaic, fuel-cell, etc.

The future technology of a microgrid promises to adopt more distributed generation and consumption to represent a whole unit in one system. This development requires the participation of consumer to generate and manage energy as well as store the extra energy to support neighbor microgrids. The common condition of a microgrid is a grid-connected mode where the DG is connected to the main distributed network to supply energy and support the main elements of the power system. The supplied power of DG can be controlled at grid-connected mode where the voltage and frequency are supported by the main grid. In some cases such as disturbance and fault in the grid or limitation of providing power from the main grid to an autonomous area, the DG is responsible for providing a stable voltage and frequency to the load. This condition is called autonomous mode and it is usually applied in an autonomous area.

1.1.2 Energy Resources

This section provides common energy resources that are used in the research. It is recommended to notice that there are other energy resources that will be covered in the future work such as fuel-cell and wind energy.

1.1.2.1 Photovoltaic (PV)

Photovoltaic (PV) is a renewable energy resource that converts the solar energy (photons) into dc electric energy (voltage) using the variety of materials such as silicon or cadmium telluride [1]. PV array consists of series and parallels connected modules and each module includes the variety of series cells. Generally, the PV system is connected to power electronic devices to extract maximum power and converter the generated dc power into ac power. VSC is applied in PV system to converter dc power into ac power while dc/dc converter is used to achieve maximum power point

tracking (MPPT) control. MPPT aims to tracks the maximum generated power from the PV even at changing weather or load disturbance.

There are several methods to apply MPPT on dc/dc converter or VSC. For example, incremental conductance (IC), perturb and observe (PO), hill climbing (HC), fuzzy logic control, and fractional control [2, 3]. Several studies have been investigated the advantages and disadvantages of each MPPT algorithm in order to improve the performance of MPPT. The paper in [4] claims that PO method provides error around the maximum power point. Adaptive HC is proposed in [5] to overcome the issues of PO. Even PO and HC can provide simple implementation, they suffer from steady state and dynamic stability issues. IC algorithm has an advantage of providing slow tracking of maximum power which offers high efficiency compared with other MPPT methods [6]. Several manuscripts aim to improve the performance of IC method such as variable step size method [7], IC slop change [8], and dead-band based IC algorithm [9]. In this dissertation, improved IC algorithm is applied to control of MPPT of PV array.

Distributed energy resources such as PV gains more interesting in research and industry fields. Installation of PV has been growing recently due to reliability, power quality, and low maintenance. In recent years, the penetration of PV into the smart grid has been significantly increased due to reducing operational cost and high efficiency. Considering the advantages of PV, it is forecasted that the PV microgrid will be the dominated renewable energy source in 2040 [3, 10, 11].

However, the increment penetration of PV may generate steady state and transient issues to the gird. Moreover, PV array supplies a dc power source while most of the loads and the main grid need to receive high-quality ac power. So, the need of converting dc power to ac power is essential to meet the load's requirements in microgrids [12].

1.1.2.2 Battery

Distributed energy resources (DERs) such as PV system requires energy storage elements in order to achieve stability and increase reliability. Since the operation period of the PV array is during the daytime, implementing energy storage such as a battery is important to achieve continuous power supply to the load or main grid. Energy storage application can provide several advantages

to the microgrid based on stability, efficiency, and reliability aspects. One of the advantages of the energy storage is that it can mitigate the limitation of DER. For example, battery storage can provide a sufficient power to the local load at night where the PV array cannot generate any power during weather condition such as cloud shadow and absence of sunlight [13].

Battery storage can be controlled using VSC based on the operating condition of the microgrid. Generally, the microgrid can be operated at two operational conditions which are grid-connected mode and autonomous mode. At grid-connected modes, the power electronics of battery systems will work at PQ control by providing stored power to the main grid. The battery may operate at charging or discharging condition based on the state of charge (SOC) of the battery. The application of the battery at grid-connected mode is presented in [14–16].

The autonomous mode of the microgrid requires a difficult control since it has to support the required voltage and frequency of the local loads as well as sharing the total load power. PV system alone could not be operated at autonomous condition regarding the weather condition and power limitation of the system. As a solution, battery storage has to be applied to support the voltage and frequency of the supplied PV array. VSC is used to control the voltage and frequency of the battery as well as regulate the charging and discharging procedures. The PV battery system is presented in several manuscripts such as [17–19].

Since the battery storage is important to operate the microgrid, modeling and controlling of the battery is needed. It is also required to analyze the battery limitation in order to achieve real implementation. For example, the SOC cannot be lower than a threshold and the depth of discharge (DOD) may impact the lifetime of the battery. Most of battery storage systems adopt the Li-ion battery because its high efficiency [20]. The differential equations modeling of Li-ion battery is presented in [21]. A detailed battery model of Li-ion is described in [22]. Dynamic model and experimental approach of the battery are shown in [23].

1.1.2.3 Plug-In Hybrid Electric Vehicle (PHEV)

The environmental and economic advantages of plug-in hybrid vehicle PHEV lead to the increase in a number of production and consumption. The U.S. Department of Energy forecasts that

over one million PHEVs will be sold in the U.S. during the next decade [24]. PHEV is operated at two power sources which are battery and internal combustion engine using fossils fuel energy. This feature increases the liability of the vehicle and reduces the operational cost. So, it has the advantage of long driving range since gas fuel is considered as a secondary consumption resource. The PHEV's battery can be charged using ac or dc outlet. Different charging levels are provided based on the charging speed and time [25].

Power electronics play an important role in controlling the charging of PHEV's battery. The battery chargers are classified as on-board and off-board converters with unidirectional or bidirectional power feature [26]. The benefit of PHEV's battery is not only reducing the dependency on conventional fossils fuel, but it can support the power quality by injecting energy back to the grid using the vehicle to grid feature. Modeling and controlling of a PV system interfaced with PHEV battery is a hot topic. In [27], modeling and power management of PV charging station is driven. The control strategy of battery and PV using VSC is presented in [28]. Hybrid microgrid to control of PV integrated PHEV is proposed in [29].

1.1.3 Smart Inverter

The recent improvements toward smart building and smart grids forced the power electronic industry to raise the industry's standards and regulation for designing and operating power electronics based on several issues such as:

- Power flow direction.
- Voltage flicker.
- Harmonic distortion.
- System reliability.
- Protection issues.
- Frequency stability.
- Voltage stability.

Conventional VSC could not solve these aforesaid issues and the need for defining smarter features for PV inverters are essential. Furthermore, the increasing need for satisfying the load demand and changing reliance on conventional power source support the necessity for smart features of VSC.

Unidirectional power flow is no longer be effective for controlling microgrids. Decentralized power system where bidirectional power flows between the DER and the main grid, provides an additional issue to the system. Changing power flow may cause voltage rise conditions at steady state as well as an unstable problem at the point of common coupling (PCC) due to overproduction of PV energy. In transient condition, the interconnection of PV system might lead to voltage flicker, harmonic distortion, system reliability problem and protection issues. [12].

Other observed problem of PV microgrid is that solar panels might generate frequent voltage flicker due to shadow clouds or suddenly disconnected from the grid. In addition, tripping or overproduction of PV feeders may cause frequency stability issues [30]. Even though centralized control and communication resources can mitigate the impact of frequency and voltage fluctuation, operational control of DG still difficult in modern decentralized energy systems. So, conventional inverters could not solve these issues and the need for defining smarter features for PV inverters is essential. Furthermore, the aforementioned issues and the increasing need for satisfying the load demand support the necessity for a smart inverter.

In order to improve the stability and reliability of the microgrid as well as solve the challenges of operating microgrids, several companies and research groups have issued standards and protocols for operating VSC based microgrid. The Electric power research institute (EPRI) has defined several functions and specifications that VSC need to adopt in order to be defined as smart inverter [31]. California public utilities commission created the smart inverter working group (SIWG) to issue standards for advanced inverter technologies [32]. The Society of Automotive Engineers (SAE) has also issued recommendations for operating and controlling electrical vehicles based on charging procedures and stability aspects [33].

Smart inverter is defined as an inverter that has the bidirectional communications capability, send and receive operational commands, and change the current sittings. The concept of smart inverter consists of three main components which are hardware architecture, main operator, and

communication network. The smart inverter operation is realized via two-way communication network to send and receive information between smart inverter and the main operator. The inverter needs first to monitor its real-data situation and send these data to the central controller. The central controller then collect these data and submit a command signal to each inverter to change the current operation point of the system. The command signal is transmitted based on predefined multifunction in the main operator. These functions are defined based on the need to the load and the main grid. These functions are capable to operate at centralized and decentralized systems as well as any microgrid connection modes. Fig. 1.2 shows multifunction features of smart inverter. The smart features of VSC in Fig. 1.2 can reduce the system topology as well as coordinate multiple DERs in single microgrid. It is worth to mention that the function of smart inverter is only realized via two-way communication bus between the inverters and the main operator.

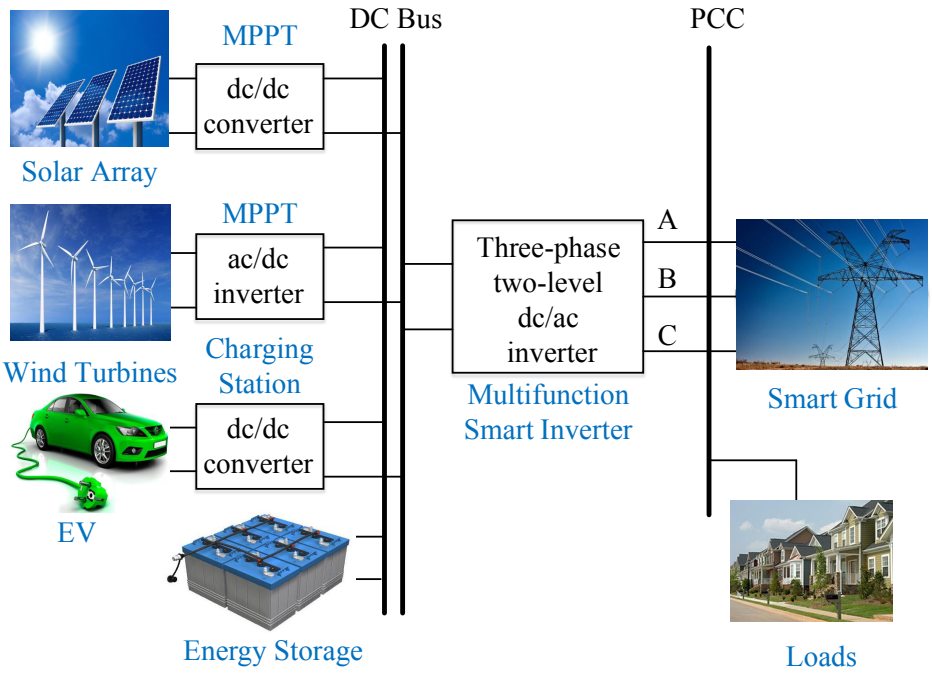

Figure 1.2. Overall view of a multifunction smart inverter

The role of smart inverters surpasses the basic functions of conventional inverters, such as maximum power point tracking, islanding detection, and power conversion. They can actually support

Table 1.1. Comparison between the functions of smart inverter and VSC

Situation	Conventional Inverter	Smart Inverter
Ride-through Utility Fault	Avoid contribution to the fault.	Involve in ride-through utility fault.
Utility Disturbance	Disconnect PV system from the grid.	Support and enhance grid V/F stability.
Power Generation	No capability to control power overproduction.	Monitor and limit power generation.
V/F variation	No contribution in supporting V/F. Only disconnected.	Monitor V/F fluctuation and generate action for stability.
Anti-island detection	Not implemented yet.	Investigate transient fault based on defined scheme.
Flicker	No contribution.	Mitigate voltage and frequency flicker.
Power factor	No contribution.	Active load balancing power factor and reactive power control.

voltage and frequency of the grid as well as provide system's stability. In real applications, the assumption of steady and stable powers are actually not an accurate by considering the unexpected behavior of the system. For example, adding new microsources, faults and disturbance in the main grid, connecting and disconnecting the DER and loads are frequent situations that affect the stability of the microgrid. So, designing an appropriate controller to handle these situations and defining multifunctions will ensure stability requirements of the load. The future development trends of smart inverter and developing its functions can help the microgrid become competitive to conventional generation resources. The key of smart inverter includes integration of PV, Battery, electric vehicle, with a smart grid for power quality achieving. Table 5.1 shows a comparison between the smart inverter and conventional inverter based on different grid situations.

1.2 Research Significance

The advanced requirements and standards of installation PV systems entail monitoring the power flow and control of smart inverter. Three main elements are used to define the control of smart inverter which is classified in this dissertation as:

- Vector Control.
- Switching Scheme.
- Schematic design.

Each part of these features needs further investigation in order to satisfy the definition of a smart inverter. The vector control is the key element of monitoring the operational and design features of the smart inverter. This part is the core of controlling the smart inverter since it provides the type of supplying element based on the microgrid's need as well as extends more stability and quality to the system. Switching scheme of the smart inverter includes applying several methods to change the switching patterns without affecting the system's quality and reliability. Comparing with other controlling method, vector control has been recently applied in most of industrial applications because of the designing advantages and methodology. By changing the switching patterns of the smart inverter, it can solve several issues of the microgrid such as harmonic distortions, common mode voltage, and voltage drop stress. A schematic design feature of the smart inverter is an advanced connection technique for extending the flexibility of the power sharing between the microgrid and the main grid. The new feature of designing smart inverter can generate both dc and ac power as well as supporting the stability of the system.

The future research on PV inverter aims to apply multifunctional smart inverter to control and monitor the system. Smart inverter functions have to fulfill the system requirements which involve connect/disconnect from the grid, power adjustment, charging/discharging storage management, voltage and frequency ride-through, voltage and frequency management, and islanding detection [34]. The future research on smart grid technology also relies on renewable energy to generate stable frequency and voltage instead of conventional energy source. This technique requires achieving ancillary services such as voltage and frequency regulation, balancing power, and blackstart. The big challenging is to practically apply the theoretical concept of conventional power sources to be operated by renewable energy. It is also required to apply the concept of smart inverter to solve the issue of connected several DER units to form the microgrid. By applying smart inverter technique, the aforementioned obstacles can be solved.

1.3 Statement of the Problem

The rapid development of power electronics enables a microgrid to participate in improving the quality and stability of the power system. However, Three problems are investigated in the dissertation which is given in the following sections:

1.3.1 Induction Motor Load at Autonomous Microgrid

A microgrid can be operated at an autonomous mode where the DER can supply sufficient voltage and stable frequency to the local load. Active loads such as induction motors occupy almost 50% of all loads in real applications [35]. The common issues of starting induction motors from stand still have no impact on a microgrid when it is connected to a strong grid. However, induction motors have a huge impact on the system in case of a weak grid or autonomous microgrid. This condition is called blackstart of induction motors and it may result in system collapse if the system cannot handle this issue. Another issue is related to the output signal from VSC. The output power from DER that involves VSC has harmonics because of the operational behavior of the switches. This feature may generate unbalanced voltage with harmonics across the motor load. The common mode voltage issue may also affect the operation of the motor's load.

1.3.1.1 Blackstart

When large induction motor's load is connected to an autonomous microgrid, the controller needs to have a good disturbance rejection in order to avoid a blackstart issue. Three important elements have to be considered in a case of blackstart of the induction motor. These components are inrush current, voltage dip, and reactive power requirements. Induction motor consumes high starting current (inrush current) during start-up condition. This current may consume almost from five up to ten times of the rated current which could destroy the motor and affect its efficiency [35]. Second, high starting current generates voltage dip which will affect the induction motor's torque since it is almost promotional to the square value of the terminal voltage. It also may affect other loads since the source voltage will be lower than the rated voltage. According to IEEE, the voltage dip during starting motors can vary between 80% to 90% of the rated voltage value [35]. So, if

voltage dip exceeds the recommended voltage dip, the motor can not generate a required torque to run the motor at the rated speed. Finally, the motor consumes high reactive power during the start-up because of high inrush current which leads to voltage dip. The lack of generating these elements may affect the efficiency and lifetime of the motor. So, voltage dip is the major concern in starting motors in a case of a weak autonomous microgrid.

1.3.1.2 Common Mode Voltage

Another issue of an autonomous microgrid is a common mode voltage. Most of the local loads at microgrid are represented as induction motors. The safe operation of the induction motors requires applying pure sinusoidal voltage without any high harmonics. However, the high penetration of DER on microgrids may generate distortion harmonics in the system which leads to common mode voltage's issue. These problems could produce high leakage current and bearing failure on motor loads. They also may cause a failure in the stator winding insulations, bearing currents, and high-frequency leakage current on the motors as well as affect the operation of circuit breakers of loads. The aforementioned issues cannot be avoided because of the structure of the inverters.

Common mode voltage (CMV) is defined as the potential difference voltage between star point of the load and the center of the $C_{\mathrm{dc-link}}$ of the DC bus. The CMV for three-phase VSC is:

$$V_{com} = \frac{V_{ao} + V_{bo} + V_{co}}{3} \tag{1.1}$$

CMV equals zero when the load receives balanced three-phase sinusoidal phase voltages. Since the inverter may generate high current harmonics, high CMV is produced on the motor's terminal. This current harmonics may affect the performance of the motor.

1.3.2 PV Charging Station

The high penetration of connecting plug-in hybrid electric vehicle (PHEV) to the main grid may generate stability issues during peak load period. Even with applying renewable energy resource such as PV systems to charge the PHEV's battery, controlling and designing the power electronic

converters are a challenging task. PV charging station requires dc/dc converter to apply MPPT algorithm while VSC is used for converting the output dc power to charge PHEV. Hybrid boost converter (HBC) has been proposed to replace a dc/dc boost converter and a dc/ac converter to achieve enhanced efficiency. A control architecture of a three-phase hybrid boost converter (3ϕ-HBC) is presented by interfacing a PV system, a dc system, and a three-phase ac system. The requirements of the main grid and local loads may present another issue of a microgrid at grid-tied mode. Challenges in control implementation for a 3ϕ-HBC compared to a conventional dc/dc boost converter with a three-phase dc/ac voltage source converter (VSC) are identified through examining the operation mechanism of the 3ϕ-HBC and the control scheme design. These challenges include the bidirectional power flow, satisfying the PHEV's charging requirements, and supplying power on different aspects based on the connection of the microgrid's busses.

1.3.3 Circulating Current

Controlling of multiple DER units at an autonomous microgrid is a challenging task since each DER needs to share the load's power and provide sufficient voltage and frequency. Coordination of DER units requires designing sufficient controller in order to guarantee stability and quality of the microgrid. Sharing load's power in an autonomous microgrid is commonly controlled by droop control technique which mimics the behavior of a synchronous generator. Achieving equal load sharing is challenging in the real application because of the mismatched line impedance and different power ratings of DER units. Droop control shows a slow dynamic behavior at the frequent disturbance. This issue can generate unequal load sharing which leads to dangerous circulating current. This circulating current is caused by mismatched reactive power across DER units which leads to overheat and damage VSC components.

1.4 Approach

Vector control is applied to control of VSC to solve the issue of blackstart and CMV. A novel design of PV charging station enhances the stability and reliability of the system. The concept of smart inverter is used for coordination multiply DER units at the microgrid.

1.4.1 VSC Control for Motor Drive

When the microgrid is operated in an autonomous mode, an attention is needed to control of the supplied voltage and frequency. This control method includes vector control to regulate the output voltage and frequency and switching scheme to operate the VSC's switches. Both techniques are required to solve the issue of blackstart and common mode voltage when large induction motor load is applied at an autonomous microgrid.

1.4.1.1 Vector Control Based Soft Start

The implementing of large induction motor's load at a weak autonomous microgrid may lead to voltage collapse during starting time. Conventional VSC could not solve this issue because of it's controlling limitation. Since controlling VSC depends on regulating the local measurement, an advanced function needs to apply to solve the issue of blackstart. This function includes regulating the voltage by applying the feature of soft start algorithm. This technique can reduce the starting current which is caused by induction motor's load as well as support the voltage and frequency profiles in the weak microgrid. It also can mitigate the reactive power requirements for a weak microgrid when motor load starting from standstill.

1.4.1.2 Switching Scheme

Several pulse width modulation (PWM) methods have been developed to control the switching pulses of a VSC. Sinusoidal pulse width modulation (SPWM) and space vector pulse width modulation (SVPWM) are commonly used methods to control of switching state patterns. The advantages of implementing SPWM and SVPWM include good ac and dc current ripple, low switching frequency and high voltage linearity range. However, they generate high common mode voltage (CMV) which may produce some problems to the system. These issues cause a failure in the stator winding insulations, bearing currents and high-frequency leakage current on the motors as well as affect the operation of circuit breakers of the loads.

Several approaches have been recently investigated to mitigate CMV [36,37]. The authors proposed hardware devices to eliminate CMV. However, using hardware elements and filters require

additional complexity and cost to the system which are not recommended solutions for economical perspective. Besides, applying software method is an effective solution to reduce common mode voltage (RCMV) at no cost.

The smart feature of VSC develops a solution for high CMV using a reduced CMV-PWM algorithm to control the switches of VSC. It also investigates the performance of V/F controller when reduced CMV-PWM technique is applied. The following approaches are implemented to provide detailed procedures for reducing CMV of VSC. First, a microgrid with V/F vector control is illustrated. Then, a reduced CMV-PWM method is investigated and compared with conventional PWM technique.

1.4.2 Hybrid Smart Converter Topology

In order to decrease the cost and enhance the efficiency of power conversion, a novel structure of hybrid converter is presented in [38]. The hybrid converter can interface a dc source, a dc load and a single-phase ac load. The hybrid converter can replace the dc/dc boost converter and the dc/ac converter. Recent research in [39] provides a hybrid single-phase converter for grid-tied applications. Another research by Ray *et al* [40] proposes a three-phase hybrid converter that serves both dc and ac loads at autonomous mode.

All previous research assumes that the hybrid converter is connected to a stiff dc voltage source. These papers do not consider the dynamic behavior of maximum power point tracking (MPPT) of PV systems. The objective of the research is to develop a control architecture for a 3ϕ-HBC that interfaces a PV system, a dc load and a three-phase ac grid. The control architecture enables MPPT, dc system voltage control, ac system reactive power control as well as bi-directional power flow to and from the ac system.

PV charging station can be used to reduce the impact of charging PHEV on the main grid. However, implementing controlling technique is complicated because of VSC needs to charge the PHEV's battery as well as generate the PV power. A novel controlling design of 3ϕ-HBC topology provides a more quality for PV charging station as well as decrease controlling complexity. It also can increase the reliability and efficiency of the PV charging station.

1.4.3 Centralized Control of Smart Inverters

The smart inverters can be upgraded to integrate multiple DER units to form a microgrid. The issue of circulating current can be solved using the smart inverter's concept. A new control strategy of the smart inverter operating DER units at an autonomous microgrid is addressed in the dissertation. The controller strategy depends on calculating the required power of the local load and regulating that power based on common communication reference bus using secondary central unit microgrid (SCUM). The injected signal from SCUM mitigates the impact of mismatched line voltage as well as achieve equal power sharing. It also provides more dynamic damping response when the droop control is not working efficiently.

Smart inverter's communication capability can provide a good solution for circulating current and reactive power problems. The coordination of DER units needs to be well controlled in order to achieve stability and efficiency of the microgrid. The steady state analysis is also driven in the research to investigate the stability criteria of the system. This method can also solve the issue of mismatched line impedance by compensating the impact of the mismatched line voltage.

1.5 Outline of the Dissertation

The structure of the proposal is organized as follows:

Chapter 1 gives a brief introduction and background of the dissertation research. This chapter includes the statement of the problems as well as proposed approaches and solutions. It also provides an overview of the contribution of the dissertation.

Chapter 2 presents a detailed literature review on a smart inverter and VSC technologies regarding controlling and application aspects. The controller of the smart inverter is designed based on the operational mode of the microgrid. Two main applications are considered in this chapter which are a low-level application for a single VSC and high-level application for the microgrid.

Chapter 3 develops vector control technique and switching scheme for VSC at autonomous microgrid. Two applications of the VSC based on the motor drive are presented in this chapter. This technique can mitigate the issue of blackstart when the weak microgrid connecting to a large motor load. It also provides a solution of common mode voltage for the microgrid.

Chapter 4 proposes a novel design and control of a PV charging station for a plug-in hybrid electric vehicle (PHEV). The topology of a three-phase hybrid boost converter is used to design a PV charging station's structure. It also shows the improvement features of PV charging station.

Chapter 5 presents a high-level control of a microgrid by integrating several smart inverters. This chapter solves the issue of circulating current which is caused by poor reactive power sharing. It also improves the stability of the microgrid when circulating current is presented.

Chapter 6 summarizes the research conclusions of the dissertation and addresses suggestions for the future work.

CHAPTER 2

CONTROL OF SMART INVERTER AND VSC

2.1 General Overview

It is important to provide a sufficient controlling technique to control power electronic's devices. The advantages of using vector control for controlling of smart inverter and VSC at a microgrid applications can be given as:

- Very fast and accurate reference response. This implies improving the quality and liability of operating the microgrid.
- Realization of a bidirectional power flow direction which can enhance the stability of the dc-link voltage of the smart inverter.
- Disturbance rejection because of the design of the inner current control. The frequency of the controller requires high bandwidth which provides more rejection of the microgrid's disturbance.
- More power can be generated from renewable resources when MPPT algorithm is applied. This advantage increases the liability of the microgrid.
- Protection of the storage resource can be enhanced using power electronic components.

This chapter focuses on modeling and controlling of smart inverter and VSC based on different connection modes of the microgrid. The following approaches are implemented to provide detailed procedures for designing and controlling of the inverters. First, an overview of different types of controllers has been provided to compare the pros and cons of each controlling methods. Second, a dynamic model is analyzed to improve system's stability. Then, two controller's schematics are

implemented based on microgrid's conditions. Finally, each controller will be designed using frequency domain. The detailed designing procedure will be illustrated as well.

Different control strategies have been implemented recently to control the smart inverter. Vector control, direct power control, and power-synchronization control are the three general effective controlling methods that are recently applied. Each control technique has advantages and disadvantages based on complexity and efficiency perspectives. Here is a brief demonstration of each controlling technique.

Direct power control is a simple controlling technique which aims to regulate the instantaneous active and reactive power directly [41, 42]. The switching table is generated based on the power error between DER unit and the grid. The configuration of a direct power controller is presented in [43]. The main concept of direct power control consists of generating the active power command by a dc-bus voltage control block while the reactive power command is directly reset. The advantage of this controller is its simplicity and directly controlling the injected power. However, the direct power control could not implement for an autonomous microgrid since the inverter needs to regulate the voltage and frequency instead of the main grid. Another disadvantage is that the controller could not protect the system from a high current that is caused by a grid fault.

The concept of power-synchronization depends on controlling the real and reactive power by controlling the phase angle and voltage of VSC, respectively. It is an improved controlling technique for direct power control. The advantage of this method is that it can be operated at weak microgrid by eliminating the dynamic impact of the phase locked loop (PLL) [44, 45]. Some problem are presented in using this method which are the low closed-loop bandwidth of a controller and failure of preventing over-current on VSC.

Vector control depends on transferring the local measured signals of the system from a three-phase time domain into synchronous rotating reference frame using Park's transformation. The controlling block includes inner current loop and out loop which includes real and reactive powers loop, dc voltage loop or ac voltage loop [46]. The inner loop is applied in both connections of the microgrid to regulate the switching pulses of VSC. The outer loop generates a reference current signal for the inner current loop. The implementation of the outer loop depends on the operational

mode of the microgrid. For example, the out loop for grid-connected VSC includes real and reactive power loops or dc and ac voltage loops. The outer loop for an autonomous microgrid involves only ac voltage controller. The advantage of the vector current control is that it can prevent over current and provide more stability to the system in case of grid's disturbance. So, it is the most powerful control method used for controlling the smart inverter [47–49]. Fig. 2.1 shows a vector controller scheme of the smart inverter and VSC.

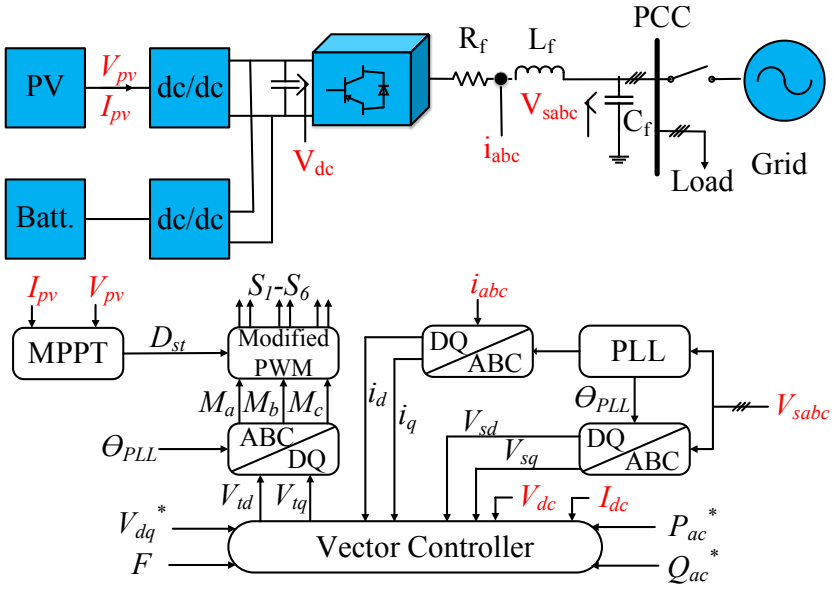

Figure 2.1. Single-line configuration of a microgrid using vector controller

2.2 Microgrid Configuration

A schematic design and controller of a microgrid is shown in Fig. 2.1. The microgrid involves a PV array as a distributed energy resource unit, battery for energy storage, dc/dc converters, smart inverter or VSC, RLC filter, breakers, and load. The breaker is controlled by a central controller to switch the microgrid from grid-connected mode to autonomous mode, and vice versa. The PV array is connected to dc/dc converter to perform MPPT algorithm. The battery is connected to dc/dc converter to support the dc-link voltage of a smart inverter as well as regulate the charging and discharging technique. The RLC line filter is an important element to extract the fundamental signals from the microgrid and reduce the current harmonics. The smart inverter or VSC is an

electronically interfacing device that converts a dc power to ac power to satisfy the requirements of the load as well as supporting the voltage and frequency. Smart inverter performs the bidirectional power conversion from dc to ac sides as well as achieve efficiency and quality aspects. Every microgrid needs a specific controlling procedure to operate the power electronic components. The smart inverter is controlled by a modern control algorithm such as PWM to be accommodated with the operation condition of the system.

This chapter aims to model and design a controller for a smart inverter for both microgrid connection modes. Designing the passive components such as a dc-link capacitor and RLC filter will also be provided. MPPT algorithm and charging/discharging methods for dc/dc converters will be covered in chapter 4.

2.2.1 Pulse Width Modulator (PWM)

The type of a smart inverter that is used in this research is a two-level three-phase VSC. It involves six IGBTs with parallel diodes to perform a bidirectional current flow. There are several methods for triggering the switches of the smart inverters which depend on controlling technique. A common method is called pulse-width modulation which mainly depends on comparing three-phase sinusoidal reference signals with a high-frequency triangular waveform. In a grid-connected mode, the sinusoidal reference signals must be synchronized with the fundamental signal of the main grid. In an autonomous mode, the microgrid provides its own three-phase reference voltage and it does not require synchronization with the grid. A phase-locked loop (PLL) device is the main component to achieve synchronization procedure.

A linear PWM is preferred to achieve continuous operation of the switches as well as reduce harmonics [50]. In order to avoid overmodulation, the dc-link voltage has to satisfy the following condition:

$$V_{dc} \geq \frac{2\sqrt{2}}{\sqrt{3}} V_{sLL} \tag{2.1}$$

where V_{sLL} is the line-line fundamental voltage of the grid. In the linear region, the amplitude modulation ratio has to be between 0 and 1 p.u.

2.2.2 RLC Filter

Applying PWM to operate the switches of smart inverters requires high-frequency switching. This injected high harmonic current is not recommended by IEEE standards [51,52]. So, passive line components can be used to filter out the high-frequency current. RLC filter consists of inductors and resistor in series and a shunted capacitor. R represents the total resistance of the filter.

The basic requirements of designing LC filter is to minimize the voltage harmonics, components' size, and power consumption [53]. The resonance frequencies for LC filter is given as:

$$f_{LCcutt} = \frac{1}{2\pi} \frac{1}{\sqrt{C_f L_f}} \tag{2.2}$$

The goal of designed the cutoff frequency is to limit switching frequency ripple to 20% of nominal current harmonic. It is also important to avoid interaction frequency with the fundamental frequency current. So, it is suggested to select the resonance frequencies to be:

$$10f_1 < f_{LCcutt} < 10f_s \tag{2.3}$$

where f_1 is the fundamental frequency and f_s is the carrier frequency of PWM.

2.2.3 Dc-Link Capacitor

A high switching harmonics from PWM may cause current ripples on the dc voltage side of VSC. Selecting an appropriate dc capacitor can improve the steady-state performance and dynamic response during disturbances. A large value of the dc capacitor may instead increase the system cost. The size of dc capacitor is designed based on a time constant τ_{dc} which is defined as the ratio between the dc stored energy over the rated apparent power of the VSC. In order to select a sufficient value of dc capacitor, the value of the capacitor is given as:

$$C_{dc} = 2\tau_{dc} S_N V_{dc}^2 \tag{2.4}$$

where S_N is the nominal apparent and V_{dc} is the nominal dc voltage. In order to achieve small voltage ripple, the time constant τ_{dc} can be selected to be less than $5ms$ [54].

2.3 Smart Inverter Control

In general, controlling a microgrid can be classified into three main levels [55]:

- Primary level [56–59].
- Secondary level [60–62].
- Tertiary control [63, 64].

The primary control is based on the droop algorithm which is called decentralized or wireless control. The main goal of the primary level is to modify the frequency and amplitude of the reference voltage based on the injected real and reactive power. This new reference voltage is injected to inner voltage and current loops to generate a switching signal to the smart inverter's switches. The common controlling design of the primary level has to include three controlling loops which are drops control, outer voltage control, and inner current control. In this dissertation, the voltage and current loops are designed based on vector control which is the common robust controlling technique to control smart inverters and VSC. Droop controller loop consists of subtracting the output average active and reactive powers from the frequency and amplitude of each DER unit to generate a reference voltage. This primary level is important in controlling the microgrid when more than one inverter is connected to the system. Accordingly, the proportional droop coefficients are adapted to regulate the output real and reactive powers of DER units as described below:

$$\omega_i = \omega_i^* - k_{Pi} P_i \tag{2.5}$$

$$V_i = V_i^* - k_{Qi} Q_i \tag{2.6}$$

where, V_i and V_i^* are the referenced and nominal amplitude voltages for ith DER unit, respectively; ω_i and ω_i^* are the referenced and preset frequencies; P_i and Q_i are the measured averages active and reactive power; k_{Pi} and k_{Qi} are the droop coefficients for real and reactive powers.

The secondary control is based on restoring of the voltage and frequency deviations that are caused by the primary droop control. The operating point of the microgrid is commonly changed based on frequency variation on the load or generator supplied energy. The primary controlling

level could not realize these changes and may submit a wrong voltage reference signal. Thus, the main role of the secondary control is to ensure that the voltage and frequency deviations are correctly regulated comparing with the preset reference signals. The important of the secondary control is not only regulate the voltage and frequency of each DER units, but it can compensate the issue of circulating current that is caused by poor reactive power sharing. The secondary control is realized via communication bus which is the key of operating the smart inverter instead of VSC at microgrid level.

The tertiary control level manages the power flow and cost between the microgrid and other distributed systems. This control level can be designed to perform multifunction quality applications such as a voltage-dip ride through, islanding detection, and power factor correction. It also can apply a cost function algorithm to improve the power flow rating and minimize the operational cost of the system. The high level controllers are realized via low-bandwidth communication bus.

This chapter studies a control scheme for a VSC and smart inverter for both connection modes of the microgrid. The microgrid is operated at autonomous and grid-connecting modes and each operational condition requires different controlling technique. In grid connection mode, the smart inverters provide real and reactive power to the main grid while the grid supplies the reference voltage, phase, and frequency to the microgrid. In an autonomous mode, the smart inverters provide a required voltage and frequency to the local loads as well as sharing the load's power. Different controlling algorithms as well as designing a microgrid topology will be discovered in details in this chapter. The vector control is adopted for the primary control which is the main operating segment of the smart inverter and VSC.

Each of these modes has a specific control and design to guarantee stability and equilibrium of the voltage, frequency, and power. Normally, the microgrid is connected to the grid at the point of common coupling (PCC). The grid provides constant voltage and frequency while the DG enhances the power in the system. Phase-locked loop (PLL) is used in this mode to lock the phase and frequency to the grid. In a case there is a fault in the main grid, the microgrid has to be disconnected from the system. In this case, the DER is responsible to provide constant voltage and frequency and the smart inverter will be controlled by VF method instead of PQ control [46, 65].

This dissertation focuses on implementing a vector control scheme for the microgrid in two connection types which are grid-connected and autonomous mode. Two vector control strategies have been implemented to provide stable and fixed power, voltage and frequency. PQ control is applied in a case of grid-connected mode and VF control is implemented for autonomous mode. The control schemes require understanding important electrical concepts and features such as PLL, vector control, PWM, current harmonics, feed-forward and decouple techniques and system dynamics.

2.3.1 Smart Inverter at Grid-Connected Mode

The common condition of operation the smart inverter is a grid-connected mode. The inverters are operated in grid following mode by exchanging powers with the grid at the point of common coupling (PCC) while the grid is responsible for providing the reference voltage and frequency. The vector current control is applied to pulse width modulation (PWM) to control of a delivered power. The real and reactive power controllers are controlled based on current control on $DQ0$ reference frame. The measured signals which are inverter current, source voltage, and control signals, are transferred into DQ reference frame. These signals are responsible for controlling the modulation index of the PWM that will be transferred back to ABC reference frame to control the smart inverter's switching components.

One of the most important segments in controlling the real and reactive power is the operating function of phase-locked loop (PLL). It is implemented to regulate the phase angle and frequency of the system in order to apply vector current control. This section also provides a detailed procedure about designing and applying PLL.

2.3.1.1 Vector Transformation Concept

The concept of vector control depends on transferring symmetrical signals from three-phase reference frame into two-phase reference axis. There are two references can be used to convert the symmetrical three-phase signals into vector signal which are classified as a synchronous reference and rotating reference frame. Synchronous reference transfers the three-phase sinusoidal signals into two-phase sinusoidal along with real and imaginary axis. Besides, rotating reference frame

transfers the sinusoidal real and imaginary components of the main vector signal into two constant components of the same vector signal.

The concept of vector transformation is illustrated in the following equations. First, the three-phase balanced signals are represented as:

$$\begin{aligned} f_a &= \hat{f}\cos(\omega t + \theta_0) \\ f_b &= \hat{f}\cos(\omega t + \theta_0 - \frac{2\pi}{3}) \\ f_c &= \hat{f}\cos(\omega t + \theta_0 + \frac{2\pi}{3}) \end{aligned} \tag{2.7}$$

where $\hat{f}$ is the amplitude's function, θ_0 is the initial phase angle and ω is the angular frequency. The space-phase of the function is represented as follow:

$$\vec{f}(t) = \frac{2}{3}[e^{j0}f_a(t) + e^{j\frac{2}{3}\pi}f_b(t) + e^{j\frac{4}{3}\pi}f_c(t)] \tag{2.8}$$

Euler's formula is applied to obtain vector signal from Equ. (2.8) which is represented as:x

$$\vec{f}(t) = (\hat{f}e^{j\theta_0})e^{j\omega t} \tag{2.9}$$

Transferring three-phase functions into real and imaginary contents or $\alpha\beta 0$ is applied by Clark transformation. The main objective of this terminology is to reduce the three ac quantities to two sinusoidal quantities. Clark transformation which converter three-phase ac signals into two phase as signals, is illustrated in the following matrix equations:

$$\begin{bmatrix} f_\alpha(t) \\ f_\beta(t) \\ f_0(t) \end{bmatrix} = \frac{2}{3}\begin{bmatrix} 1 & -\frac{1}{2} & \frac{1}{2} \\ 0 & \frac{\sqrt{3}}{2} & -\frac{\sqrt{3}}{2} \\ \frac{1}{2} & \frac{1}{2} & \frac{1}{2} \end{bmatrix}\begin{bmatrix} f_a(t) \\ f_b(t) \\ f_c(t) \end{bmatrix} \tag{2.10}$$

Transferring three-phase functions into $DQ0$ is applied by Park transformation. The objective of this method is to transfer three ac quantities to two dc quantities. The direct transformation is shown in following matrix:

$$\begin{bmatrix} f_d(t) \\ f_q(t) \\ f_0(t) \end{bmatrix} = \frac{2}{3} \begin{bmatrix} \cos(\varepsilon(t)) & \cos(\varepsilon(t)) - \frac{2\pi}{3}) & \cos(\varepsilon(t) - \frac{2\pi}{3}) \\ \sin(\varepsilon(t)) & \sin(\varepsilon(t) - \frac{2\pi}{3}) & \sin(\varepsilon(t) - \frac{2\pi}{3}) \\ \frac{1}{2} & \frac{1}{2} & \frac{1}{2} \end{bmatrix} \begin{bmatrix} f_a(t) \\ f_b(t) \\ f_c(t) \end{bmatrix} \tag{2.11}$$

The concept of vector control of the system is illustrated in Fig. 2.2. The rotating speed of the constant vector equals the speed of the grid's frequency ω. The phase angle θ is defined as the integral of the grid's frequency.

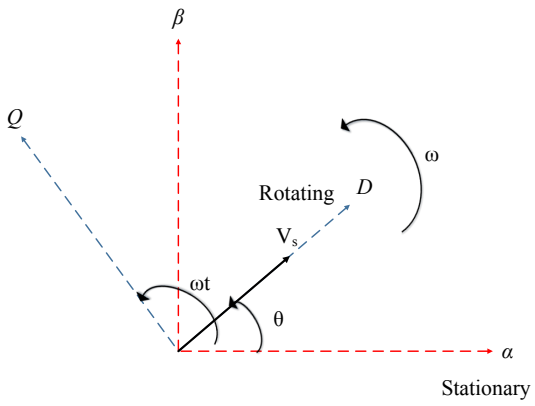

Figure 2.2. DQ and $\alpha\beta$ reference frames

Controlling and designing a system in rotating reference frame has several advantages than synchronous reference axis. The level of efficiency of the closed-loop system relies on tracking a reference command based on closed-loop bandwidth. The bandwidth and level of the order of the loop compensator depend on the type of input signal. For example, designing a compensator in synchronous reference frame requires complex and high-order compensator according to the reference signal and closed-loop bandwidth. High closed-loop bandwidth is necessary to achieve zero steady-state error in a case of sinusoidal reference command. However, transferring signals into rotating synchronous reference frame guarantees dc signals in a steady state. So, a simple proportional-integral (PI) compensator is efficient to achieve zero steady-state error since the compensator includes a pole in the origin. Another advantage is that controlling real and reactive power can be achieved independently because of using PLL.

2.3.1.2 Phase Locked Loop (PLL)

Phase-locked loop (PLL) is one of the most critical segments in synchronization systems. The main function of PLL is to lock the phase and frequency of the distributed network to the utility grid. Several models of PLL have proposed for the grid synchronization purpose. For example, Zero Crossing-Detector (ZCD), Synchronous Frame (SF-PLL), Synchronous Rotating Frame (SRF-PLL), and Double Synchronous Frame PLL (DSF-PLL) are various methods of using PLL in grid-synchronizing [66]. SRF-PLL among all other types of PLL is applied according to its simplicity and accuracy in detecting the phase and frequency in both ideal and non-ideal grid conditions such as unbalance, presence of harmonics, frequency variation, voltage dip and faults [67].

The operation of SRF-PLL depends on transferring reference axis from three-phase frame into DQ reference frame using Park's transformation. Transformation of axes is illustrated previously in subsection 2.3.1.1. Accordingly, all vector signals are transformed from three-phase reference into two-phase synchronous rotating reference. So, The voltage vectors can be found out from the following equations:

$$V_{sd} = \hat{V}\cos(\omega_0 t + \theta_0 - \rho(t)) \tag{2.12}$$

$$V_{sq} = \hat{V}\sin(\omega_0 t + \theta_0 - \rho(t)) \tag{2.13}$$

where:

$$\rho(t) = \omega_0 t + \theta_0$$

where ω_0 is the frequency angle and θ_0 is the phase angle of the main grid; V_{sdq} are the DQ signals of the grid's voltages.

The major concept of SRF-PLL is to force the vector voltage V_{sq} to be equal zero in the steady state. This concept can be applied by designing a robust compensator which guarantees zero steady state error as well as zero value for V_{sq}. Thus, the value of V_{sd} equals the nominal value of reference voltage. The operation of SRF-PLL is explained in Fig. 2.3.

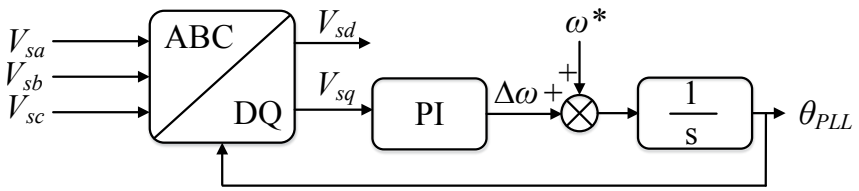

Figure 2.3. Basic schematic diagram of an SRF-PLL

The system has fast and accurate tracking of the phase and amplitude of the utility voltage vector according to a high closed-loop bandwidth in an ideal situation. However, the PLL bandwidth has to be decreased in a case of grid-disturbance which will affect the response speed and precision. Consequently, designing the loop compensator plays an important role in achieving the desired stability as well as providing a high closed-loop bandwidth in non-ideal situations [66].

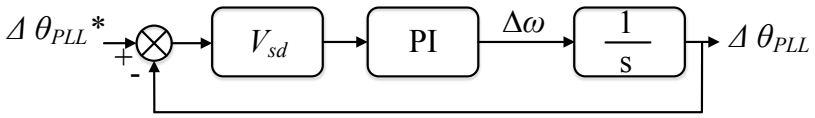

Figure 2.4. Linearized model of SRF-PLL

The model of PLL needs to be linearized in order to better understanding and designing the loop compensator. The linear model of PLL is shown in Fig. 2.4. The model of PLL includes the nominal voltage, loop compensator, and voltage controlled oscillator. The SRF-PLL is considered as a second-order system which has a following general closed-loop transfer function:

$$H_c(s) = \frac{2\zeta\omega_n s + \omega_n^2}{s^2 + 2\zeta\omega_n s + \omega_n^2} \tag{2.14}$$

The open-loop transfer function is given from the linearized model of the SRF-PLL in Fig. 2.4.

$$G_{\mathrm{PLL}}(s) = \frac{V_{sd}}{s} H(s) \tag{2.15}$$

$$G_{\mathrm{PLL}} = \frac{k_{p,\mathrm{PLL}} + k_{i,\mathrm{PLL}} s}{s} \frac{V_{sd}}{s} \tag{2.16}$$

where $k_{p,\mathrm{PLL}}$ is a loop gain and $k_{i,\mathrm{PLL}}$ represents an integral loop's gain.

The closed-loop transfer function of SRF-PLL can be represented as:

$$G(s) = \frac{H(s)V_{sd}}{s + H(s)V_{sd}} \tag{2.17}$$

subtituting Eqn. (2.17) with Eqn. (2.14) leads to the following parameters:

$$k_{i,\mathrm{PLL}} = \frac{\omega_n^2}{V_{sd}} \tag{2.18}$$

$$k_{p,\mathrm{PLL}} = \frac{2\zeta\sqrt{k_{i,\mathrm{PLL}}V_{sd}}}{V_{sd}} \tag{2.19}$$

2.3.1.3 PLL Controller Design

Tuning the parameters of the compensator depends on selecting the natural frequency ω_n and the damping ratio ζ. ω_n is assumed to equal the reference frequency of the grid and ζ provides a required damping to the system which equals $\frac{1}{\sqrt{2}}$. Based on Eqns. (2.18) and (2.19), the compensator gains $k_{p,\mathrm{PLL}}$ and $k_{i,\mathrm{PLL}}$ are calculated based on Eqn. (2.18). The parameter values are chosen based on the optimal design of PLL device as follows:

$$\omega_n = 377\frac{rad}{sec},$$

$$V_{gn} = 391.15v,$$

$$k_{p,\mathrm{PLL}} = 1.362v^{-1},$$

$$k_{i,\mathrm{PLL}} = 363.3\frac{rad}{secV},$$

Figs. 2.5 and 2.6 show the Bode plot of open-loop and closed-loop transfer function of PLL. The phase margin at the crossover frequency is 114° and the closed loop bandwidth is 597 rad/sec.

2.3.1.4 PQ Plant Model

Fig. 2.1 is analyzed to find the relationship between the controlled current and the disturbance signals [1]. These signals include the grid voltage and VSC terminal voltages. The system shows

[1]This part was published in Power & Energy Society General Meeting, 2015 IEEE 2015 July 26 (pp. 1-5). Permission is included in Appendix A.

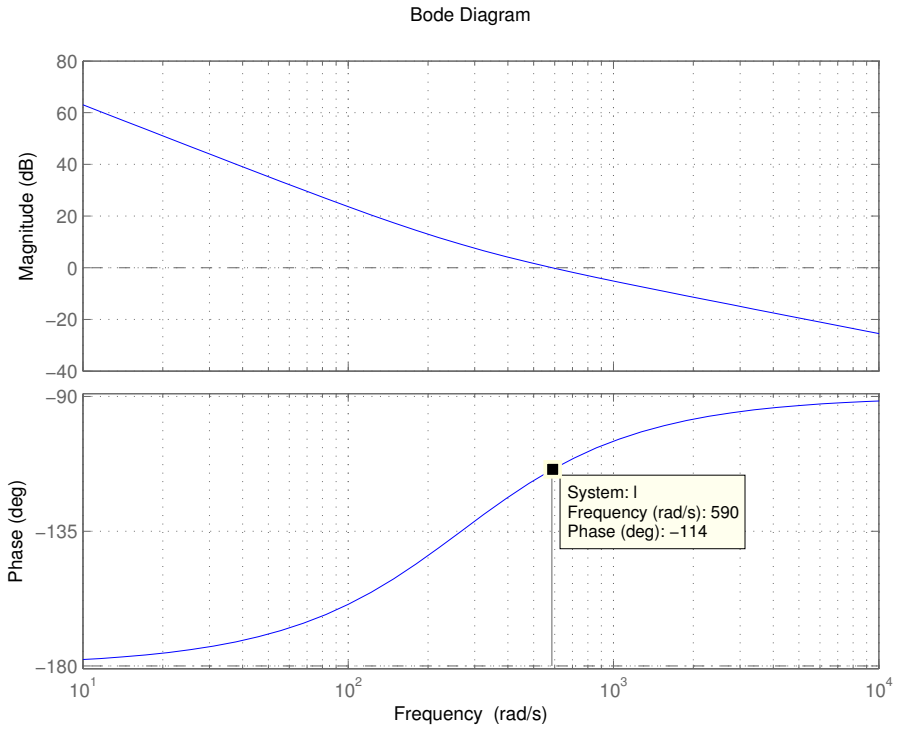

Figure 2.5. Bode plot of open-loop transfer function of SRF-PLL

that two main components have to be controlled which are the output current and powers of the DER unit. The concept of vector control depends on modeling two cascaded loops. The current loop is called inner controller and the power loop is called outer controller.

The three-phase symmetrical components are assumed to analyze the dynamic equation of the system. KVL is applied to obtain system's dynamic and load's voltage at PCC from Fig. 2.7. The advantage of vector control is limiting the high current that is caused by grid's fault. KVL is applied in the inner current loop to find the dynamic equations of the system as follows:

$$V_{tabc} = L\frac{di_{abc}}{dt} + V_{sabc} + Ri_{abc} \tag{2.20}$$

The space-phasor of three-phase signals are obtained as follows:

$$L\frac{d\vec{i}}{dt} = -R\vec{i} + \vec{V_t} - \vec{V_s} \tag{2.21}$$

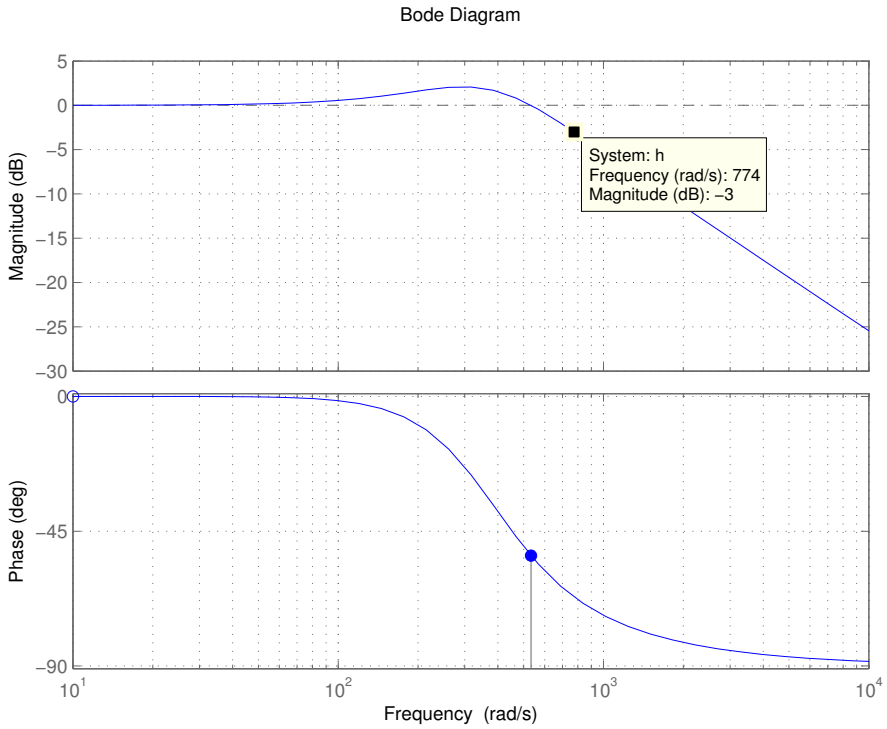

Figure 2.6. Bode plot of closed-loop transfer function of SRF-PLL

Transferring the feedforward and backward signals in Eqn. (2.21) into DQ-frame are illustrated as:

$$L\frac{di_d}{dt} = -R\vec{i_d} + Lw(t)i_q + \vec{V_{td}} - \hat{V_s} \tag{2.22}$$

$$L\frac{di_q}{dt} = -R\vec{i_q} - Lw(t)i_d + \vec{V_{tq}} \tag{2.23}$$

Eqns. (2.22) and (2.23) are used to find the state space equation where i_d and i_q are state variables, V_{td} and V_{tq} are control inputs and V_{sd} and V_{sq} are disturbance inputs. It can be seen from the previous equations that the dynamics of i_d and i_q are couple because of the appearance of cupeling inductance. So, Eqns. (2.22) and (2.23) are adjusted to achieve decouple dynamic as follows:

$$u_d = -L\omega i_q + v_d - V_{sd} \tag{2.24}$$

$$u_q = +L\omega i_d + v_q - V_{sq} \tag{2.25}$$

where

$$V_d(t) = \frac{V_{dc}}{2} m_d(t)$$
$$V_q(t) = \frac{V_{dc}}{2} m_q(t)$$

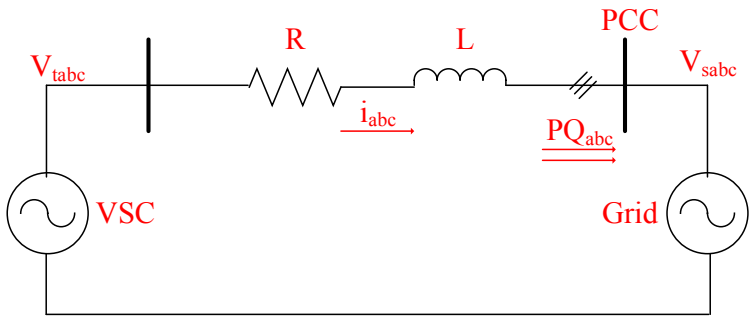

Figure 2.7. Phase circuit diagram of a smart inverter at grid-connected mode

Designing the controller is achieved by transferring the feedforward signals into s-domain by applying Laplace transformation on Eqns. (2.22)-(2.25). The current equations in s-domain is obtained as follows:

$$Ł[L\frac{di_d}{dt}] + Ł[Ri_d] = Ł[ud] \tag{2.26}$$
$$Ł[L\frac{di_q}{dt}] + Ł[Ri_q] = Ł[uq] \tag{2.27}$$

The current equations are analyzed in s-domain to find model the bandwidth of the current loop. The current equations in s-domain are shown below:

$$i_d = \frac{1}{Ls + R} u_d(s) \tag{2.28}$$
$$i_q = \frac{1}{Ls + R} u_q(s) \tag{2.29}$$
$$u_d(s) = (i_d^* - i_d)(k_{pi} + \frac{k_{ii}}{s}) \tag{2.30}$$
$$u_q(s) = (i_q^* - i_q)(k_{pi} + \frac{k_{ii}}{s}) \tag{2.31}$$

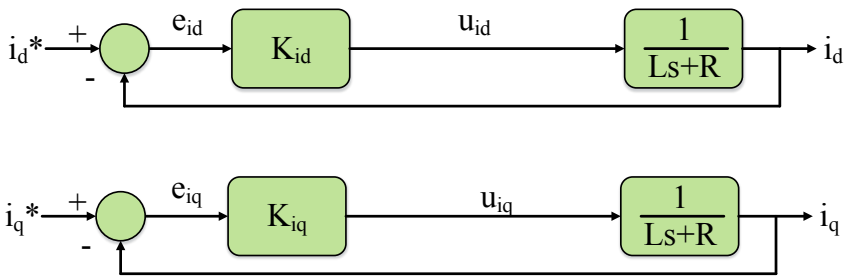

Figure 2.8. Simplified control block diagram of the inner current loop

Based on Eqns. (2.26) and (2.27), the simple current controller design is shown in Fig. 2.8. The system has two cascaded loops which includes output power loop and inner current loop. The state space representation of the real and reactive power are given as follow:

$$\begin{bmatrix} \frac{di_d}{dt} \\ \frac{di_q}{dt} \end{bmatrix} = \begin{bmatrix} \frac{-R}{L} & 0 \\ 0 & \frac{-R}{L} \end{bmatrix} \begin{bmatrix} i_d \\ i_q \end{bmatrix} + \begin{bmatrix} \frac{1}{L} & 0 \\ 0 & \frac{1}{L} \end{bmatrix} \begin{bmatrix} u_d \\ u_q \end{bmatrix}$$

$$\begin{bmatrix} P_{pcc} \\ Q_{pcc} \end{bmatrix} = \begin{bmatrix} \frac{3V_{sd}}{2} & 0 \\ 0 & \frac{3V_{sd}}{2} \end{bmatrix} \begin{bmatrix} i_d \\ i_q \end{bmatrix}$$

The outer controller loop is analyzed based on Fig. 2.2. The real and reactive power equations can be controlled independently by using PLL. Implementing PLL provides the possibility to align the vector voltage on D axis by regulate the phase angle ρ to be equal $w_0 t + \theta$ as steady state. So, the vector voltage at D axis will equal the nominal grid's voltage. Besides, the voltage vector at Q axis will equal zero. The real and reactive power equations are obtained as:

$$\begin{aligned} P_s(t) &= \frac{3}{2}(V_{sd}(t)i_d(t) + V_{sq}(t)i_q(t)) \\ &= \frac{3}{2}V_{sd}(t)i_d(t) \end{aligned} \tag{2.32}$$

$$\begin{aligned} Q_s(t) &= \frac{3}{2}(-V_{sd}(t)i_q(t) + V_{sq}(t)i_d(t) \\ &= -\frac{3}{2}V_{sd}(t)i_q(t)) \end{aligned} \tag{2.33}$$

Eqns. (2.32) and (2.33) are transferred into s-domain using Laplace transformation. The real and reactive power equations in s-domain are given as:

$$P_s(t) = \text{Ł}[\frac{3}{2}V_{sd}(t)i_d(t))]$$
$$P_s(s) = \frac{3}{2}V_{sd}(s)i_d(s) \tag{2.34}$$
$$Q_s(t) = \text{Ł}[-\frac{3}{2}V_{sd}(t)i_q(t))]$$
$$Q_s(s) = -\frac{3}{2}V_{sd}(s)i_q(s) \tag{2.35}$$

Eqns. (2.34) and (2.35) are used to control of the reference signals of the real and reactive power. The control scheme of real and reactive power is illustrated in Fig. 2.9. Since the controlling components have dc values at DQ reference frame, implementing PI compensators for power loops are sufficient to guarantee zero error between the reference and measured signals. The real and reactive controller in s-domain are given as:

$$P_s(s) = \frac{1}{1+\tau_i s}\left(\frac{3}{2}V_{sd}(s)u_P(s)\right) \tag{2.36}$$
$$Q_s(s) = \frac{1}{1+\tau_i s}\left(-\frac{3}{2}V_{sd}(s)u_Q(s)\right) \tag{2.37}$$
$$u_P(s) = (P^* - P)(k_{pP} + \frac{k_{iP}}{s}) \tag{2.38}$$
$$u_Q(s) = (Q^* - Q)(k_{pQ} + \frac{k_{iQ}}{s}) \tag{2.39}$$

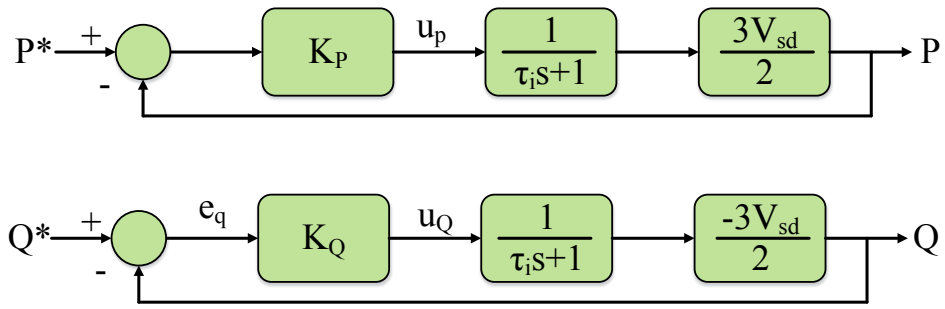

Figure 2.9. Block diagram of real and reactive power controllers

2.3.1.5 PQ Controller Design

Designing a controller for smart inverter and VSC basically depend on determining the structure of the controller and regulating the controller's parameters. These elements have to accomplish stability, speed response, and disturbance rejection. The open loop transfer function of the inner current controller is obtained from Fig. 2.8 and illustrated as:

$$\begin{aligned} l(s) &= K(s)G(s) \\ &= (k_{pi} + \frac{k_{ii}}{s})\frac{1}{Ls+R} \end{aligned} \tag{2.40}$$

where $K(s)$ and $G(s)$ are the transfer functions of the compensator and loop's plant."Modulus Optimum" is a sufficient method to tune the parameters of the inner current compensator since the order of the closed-loop transfer function is less than 3 [68]. Since the system has one dominate pole, "zero-pole canceling" method is efficient to provide fast closed loop response. The main concept of implementing this approach is to cancel the dominated pole of the plant with the zero component of the compensator. Thus, the system will reply rapidly with the reference signal according to high selected cutoff frequency.

The open-loop transfer function of the inner current loop is obtained from Fig. 2.8 as following:

$$G_{ol} = k_{pi}(\frac{s + \frac{k_{ii}}{k_{pi}}}{s})\frac{1}{L(s + \frac{R}{L})} \tag{2.41}$$

$$= \frac{k_{pi}}{R\tau_s s} \tag{2.42}$$

The dominate pole of the plant can be canceled by adjusting the compensator's zero. Assuming $k_{pi} = \frac{L}{\tau_i}$ and $k_{ii} = \frac{R}{\tau_i}$ and no time delay on the converter. The closed-loop current's time constant τ_i is calculated to equal $\tau_i = \frac{L}{R}$. The open and closed loop transfer function of the inner current will be formed as:

$$G_{ol} = \frac{k_{pi}}{Ls} \tag{2.43}$$

$$G_{cl} = \frac{k_{pi}}{Ls + k_{pi}} = \frac{1}{\tau_s s + 1} \tag{2.44}$$

Tuning the current compensator depends on the desired requirements of the system in both time and frequency domains. One of the important keys in tuning the system is to design a closed-loop bandwidth. The closed-loop bandwidth of the inner current has to be higher than the natural system frequency. However, the bandwidth has to be limited by at least 10 times lower than the switching frequency to avoid interfacing with switching frequency noise. The form of the closed loop of inner current is in a first-order transfer function where the value of τ_i regulates the desired closed-loop bandwidth as given as:

$$\omega_{switching} > 10 \times \omega_i > \omega_n. \tag{2.45}$$

The outer-power loop is shown in Fig. 2.9. The open-loop transfer function of the outer-loop of both real and reactive power are given as:

$$G_{Pol} = (k_{Pp} + \frac{kPi}{s})\frac{1}{(\tau_i s + 1)}\frac{3V_{sd}}{2} \tag{2.46}$$

$$G_{Qol} = (k_{Qp} + \frac{kQi}{s})\frac{1}{(\tau_i s + 1)}\frac{-3V_{sd}}{2} \tag{2.47}$$

Since the outer power controller only adds a constant gain to the transfer function's loop, "Modulus optimum" can be used to tune the compensator. The same procedures of tuning the inner current loop are applied to tune the outer power loop. Assuming the integral time constant $T_s = k_{Pp}/k_{Pi}$ equals the time constant of closed-loop inner current τ_i, the transfer function of open and closed loop of the outer real and reactive power controller are driven as:

$$G_{Pol} = k_{Pp}\frac{3V_d}{T_s s2} \tag{2.48}$$

$$G_{Pcl} = \frac{1}{1 + as} \tag{2.49}$$

$$Q_{Pol} = k_{Qp}\frac{-3V_d}{T_s s2} \tag{2.50}$$

$$G_{Pcl} = \frac{1}{1 + bs} \tag{2.51}$$

where $a = \frac{2T_s}{3V_{sd}k_{Pp}}$ and $b = \frac{2T_s}{-3V_{sd}k_{Qp}}$ are the gains of the output power loops.

The compensator gain has to be unity at the selected cutoff frequency. The compensator gain is obtained from solving the open-loop's amplitude on Eqns. (2.48) and (2.50) as driven below:

$$|G_{ol}|= |k_{Pp}(\frac{3V_{sd}}{T_s s2})|= 1 \tag{2.52}$$

The optimal gain of the compensator at cutoff frequency is selected as:

$$k_{Pp} = \frac{T_s \omega_c 2}{3V_{sd}} \tag{2.53}$$

The zero-pole cancelation is applied to remove the slow process pole of the open loop transfer function. So, the order of the system decreases and the dominate pole will be closed to the origin. Eqns. (2.43) and (2.44) are used to define the closed-loop and open-loop parameters of the compensator. The parameters of the grid and the controller are given in Table. 2.1.

Table 2.1. Controller's parameters for the inner current loop

System Parameters	Value	Controller Parameters	Value
Grid Frequency	$\omega_n = 377 rad/sec$	Loop Gain	$\tau_i = 1msec$
Switching Frequency	$f_s = 18.8krad/sec$	Proportional Gain	$k_{pi} = 0.048\Omega$
Resistance Filter	$R_f = 48m\Omega$	Integrator Gain	$k_{ii} = 48\frac{\Omega}{sec}$
Inductance Filter	$L_f = 48u\Omega$	Closed-loop Bandwidth	$\omega_{bw}1000\ rad/sec$

Frequency domain is used to represent the desired requirement of the inner current loop. The frequency representation of the system is plotted using Bode plot which is graph of the frequency response of the magnitude and frequency of the system. Figs. 2.10 and 2.11 show the Bode plot of the open and closed-loop inner current controller. It can be seen that the closed-loop bandwidth is 1000 rad/sec which is the desired bandwidth of the system. The high closed-loop bandwidth of the inner current loop provides more dynamic response of the system as well as participates in disturbance rejections. The Bode plot of open-loop current controller also shows that the system is stable according to the phase margin of the open-loop current. The phase margin is 90^o which indicates that the system has only one dominate pole. This dominate pole is compensated by the PI compensator which can regulate the bandwidth of the controller.

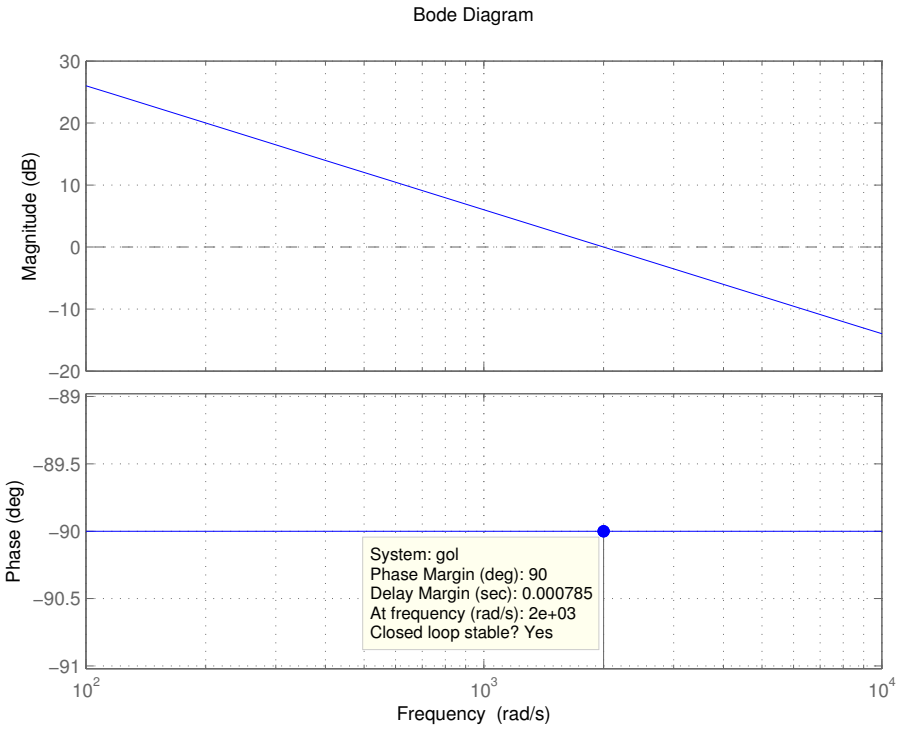

Figure 2.10. Bode plot of the open-loop transfer function of inner current controller

Analyzing the outer-loop of real and reactive power is based on modulus optimum method. Eqns. (2.48)-(2.53) are used to tune the compensator parameters of the open outer loop of real and reactive powers of Eqns. (2.46) and (2.47). The parameters of the outer power controller are given in Table 2.2.

Table 2.2. Controller's parameters for the outer power loop

System Parameters	Value	Controller Parameters	Value
Grid Frequency	$\omega_n = 377 rad/sec$	Inner Loop Gain	$\tau_i = 1 msec$
Switching Frequency	$f_s = 18.8 krad/sec$	Proportional Gain	$K_{Pp} = 0.0017 \frac{1}{v}$
Nominal Voltage	$V_{sd} = 120V$	Integrator Time Constant	$T_{sPQ} = 2 msec$
Power Factor	$\cos(\theta) = 1$	Closed-loop Bandwidth	500 rad/sec

Frequency domain is used to show the desired requirement of the inner current loop. Figs. 2.12 and 2.13 show the Bode plot of the open and closed-loop outer power controller. It can be seen that the closed-loop bandwidth is 500 rad/sec which is the desired bandwidth of the system. Also,

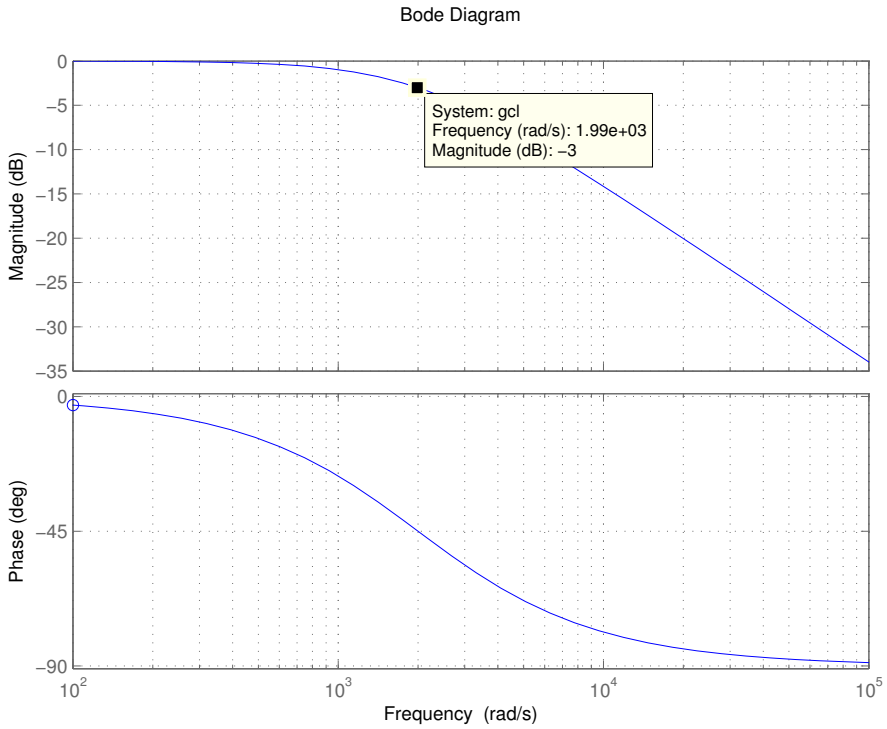

Figure 2.11. Bode plot of the closed-loop transfer function of inner current controller

the Bode plot of open-loop shows that the system is stable according to the phase margin of the open-loop current and power. Since the phase margin is located within 180^o, the system is stable. The high bandwidth of the inner current loop indicates that the system has high response to any disturbances in the microgrid.

2.3.2 Smart Inverter at Autonomous Mode

In grid-connected mode, the main grid is responsible for providing constant voltage and frequency as a reference to the system while the DER unit provides supported real and reactive power to the load and the main grid. However, in a case of any fault or disturbance in the main grid, the system has to be disconnected to protect the load. The DER unit has to change its operation mode to grid forming condition. It requires supplying reference voltage and frequency as well as sharing the power's load. The VSC controlling mode is changed to as VF control instead of PQ control.

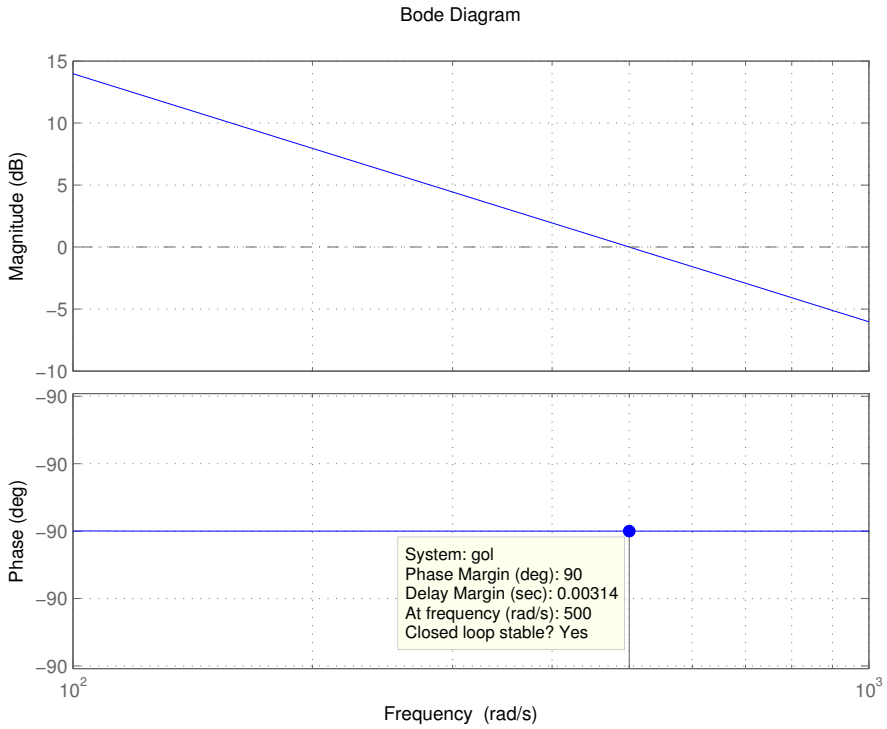

Figure 2.12. Bode plot of the open-loop transfer function of outer power controller

In Fig. 2.1, the microgrid is operated in autonomous mode when the main switch is disconnected from the main grid. PLL is not needed in this condition since the grid is disconnected. However, PLL is applied before connecting the system to resynchronization the DER with the grid. The frequency is provided from a voltage-controlled oscillator (VCO).

2.3.2.1 VF Plant Model

Fig. 2.1 illustrates a schematic design of an autonomous DER unit when the microgrid is disconnected from the main grid [2]. The measured signals which are inverter current, load current, and control signals, are transferred into DQ reference. These signals are responsible for controlling the modulation index of PWM that transfers back to ABC frame to control of smart inverter's switching components. The three-phase symmetrical component is assumed to analyze the dynamic

[2]This part was published in North American Power Symposium (NAPS), 2015 Oct 4 (pp. 1-5). IEEE. Permission is included in Appendix A.

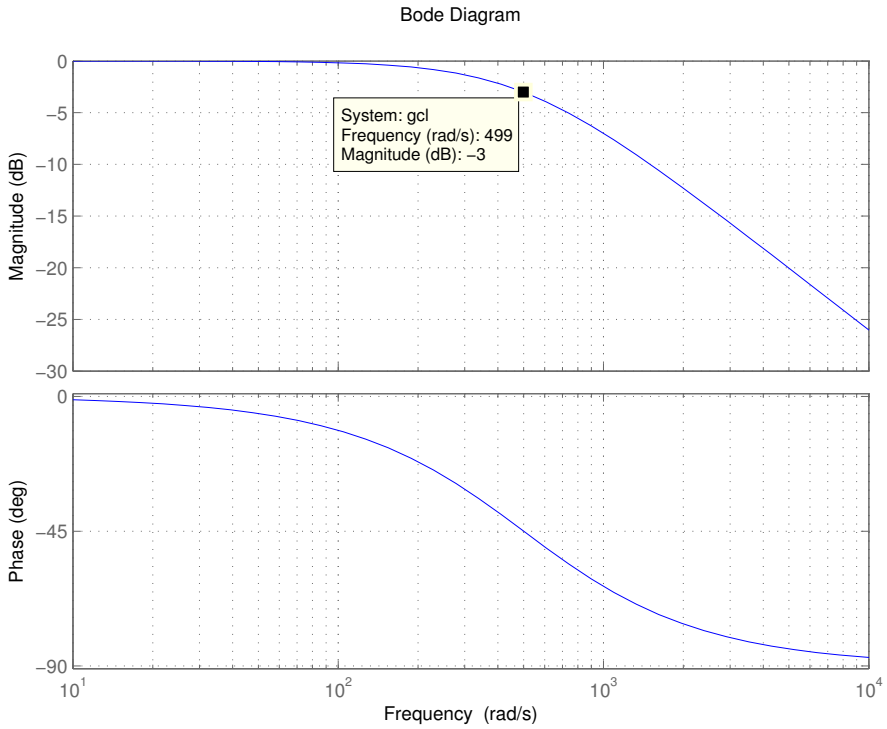

Figure 2.13. Bode plot of the closed-loop transfer function of outer power controller

equation of the system. KVL is applied to obtain system dynamic and load voltage at PCC from Fig. 2.14. The dynamic equation of the DER unit at an autonomous microgrid is driven as:

$$C\frac{dV_{sabc}}{dt} = i_{abc} - i_{labc} \tag{2.54}$$

$$L\frac{di_{abc}}{dt} = V_{t_{abc}} - V_{sabc} - Ri_{abc} \tag{2.55}$$

The measured signals of the VSC include output current and voltage. So, the cascaded controller needs to be designed based on these signals which includes the inner current loop and the outer voltage loop. The space-phasor of three-phase signals is:

$$C\frac{d\vec{V_c}}{dt} = \vec{i} - \vec{i_l} \tag{2.56}$$

$$L\frac{d\vec{i}}{dt} = \vec{V_t} - \vec{V_s}R\vec{i} \tag{2.57}$$

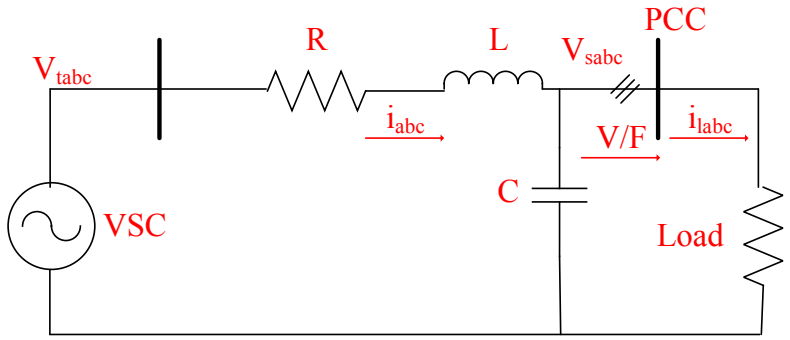

Figure 2.14. Phase circuit diagram of a smart inverter based grid-connected mode

The vector voltage equations in DQ-frame are:

$$C\frac{dV_{sd}}{dt} = C\omega V_{sq} + i_d - i_{ld} \tag{2.58}$$

$$L\frac{di_d}{dt} = -R\vec{i_d} + Lw(t)i_q + \vec{V_{td}} - \hat{V_s} \tag{2.59}$$

$$C\frac{dV_{sq}}{dt} = -C\omega V_{sd} + i_q - i_{lq} \tag{2.60}$$

$$L\frac{di_q}{dt} = -R\vec{i_q} - Lw(t)i_d + \vec{V_{tq}} \tag{2.61}$$

The system in autonomous mode has two controllers that are current and voltage controllers. The dynamics of the outer voltage are represented in the space-phase equation as:

$$\begin{aligned} \vec{i_c} &= \vec{i} - \vec{i_l} \\ C\frac{d\vec{V_s}}{dt} &= \vec{i} - \vec{i_l} \end{aligned} \tag{2.62}$$

Transforming the space-phasor on Eqn. (2.62) into $DQ - frame$ using $\vec{f} = (f_d + jf_q)e^{j\rho(t)}$ is illustrated as:

$$C\frac{dV_{sd}}{dt} = C\omega V_{sq} + i_d - i_{ld} \tag{2.63}$$

$$C\frac{dV_{sq}}{dt} = -C\omega V_{sd} + i_q - i_{lq} \tag{2.64}$$

It is noticed that the dynamics of V_{sd} and V_{sq} are couple because of the appearance of cupeling capacitance. So, Eqns. (2.63) and (2.64) are adjusted to achieve decouple dynamic using the concept of feedforward technique as :

$$u_{vd} = -C\omega V_{sq} + i_{ld} \tag{2.65}$$

$$u_{vq} = +C\omega V_{sd} + i_{lq} \tag{2.66}$$

The output voltage equations in s-domain is obtained as follow:

$$Ł[C\frac{dV_{sd}}{dt}] = Ł[C\omega V_{sq}] + Ł[i_d] - Ł[i_{dl}] \tag{2.67}$$

$$\begin{aligned} CsV_{sd}(s) &= G_i(s)U_d(s) + [1 - G_i(s)]CŁ[\omega V_{sq}] \\ &\quad - [1 - G_i(s)]I_{ld}(s) \end{aligned} \tag{2.68}$$

$$\begin{aligned} Ł[C\frac{dV_{sq}}{dt}] &= -Ł[C\omega V_{sd}] + Ł[i_q] - Ł[i_{ql}] \\ CsV_{sq}(s) &= G_i(s)U_q(s) - [1 - G_i(s)]CŁ[\omega V_{sd}] \\ &\quad - [1 - G_i(s)]I_{Iq}(s) \end{aligned} \tag{2.69}$$

where, G_i is the closed loop of inner current controller which equals $G_i = \frac{1}{\tau_s s+1}$. Substituting Eqns. (2.41) and (2.44) into Eqns. (2.68) and (2.69), the voltage dynamic equations are obtained as:

$$V_{sd}(s) = \frac{1}{Cs}U_d(s)G_i(s) \tag{2.70}$$

$$V_{sq}(s) = \frac{1}{Cs}U_q(s)G_i(s) \tag{2.71}$$

The control block diagram is shown in Fig. 2.15 based on Eqns.(2.70) and (2.71).

2.3.2.2 VF Controller Design

The desire of tuning the inner controller is to achieve a fast response. Besides, the main goal of designing the outer loop is to acquire optimum regulation and stability. Designing of voltage and frequency controller is obtained from Eqns. (2.22), (2.23), (2.63), and (2.64). The controller

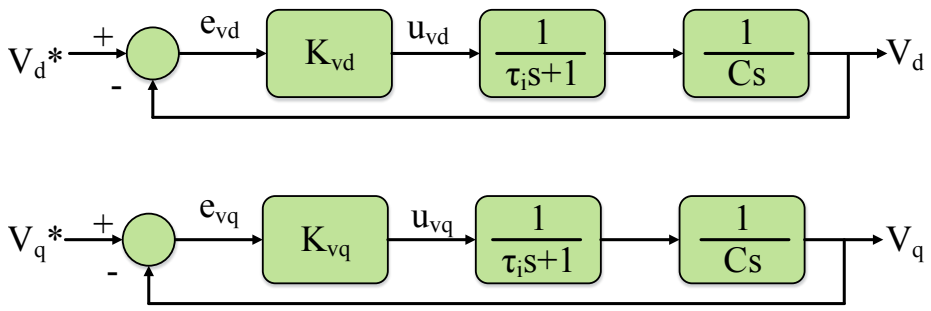

Figure 2.15. Block diagram of voltage controllers

of VSC includes an inner current controller and an outer voltage controller. The response of the inner controller is faster than the outer one and it provides regulation of the current of the VSC. Using feed-forward compensator can eliminate the decoupling between V_{sd} and V_{sq}.

Fig. 2.15 shows the block diagram of the voltage controller. It can be seen that the system has two poles in the origin based on plant and compensator transfer functions. So, zero-pole cancelation of pole adjustment cannot be applied to tune the controller. "Symmetrical optimum" method is used to provide more stability to the system by providing more delays in a certain frequency. This method depends on forcing the frequency response of the open-loop transfer function of the system as close as possible to that for low frequencies [68].

The open loop transfer function of the voltage controller is illustrated below as:

$$\begin{aligned} G_{vol}(s) &= K_v(s)G_{icl}(s)P_v(s) \\ &= (k_{pv} + \frac{k_{iv}}{s})(\frac{1}{\tau_s s + 1})(\frac{1}{Cs}) \end{aligned} \tag{2.72}$$

where $K_v(s)$,$G_i(s)$ and $P_v(s)$ are the outer loop compensator, inner closed-loop current and outer voltage plant, respectively. The phase margin of the outer voltage loop is given as :

$$\angle G_{vol} = \tan^{-1}(T_s\omega_c) - \tan^{-1}(\tau_i\omega_c) - 180^o = \Phi_m - 180 \tag{2.73}$$

where, Φ_m, T_s, τ_i and ω_c are maximum phase margin, integrator time constant and current loop time constant, cut off frequency respectively.

The maximum phase margin is obtained by differentiate Φ_m with respect to the cutoff frequency ω_c as shown below:

$$\frac{d\Phi_m}{d\omega_c} = \frac{T_s}{1+(T_s\omega_c)^2} - \frac{\tau_i}{1+(\tau_i\omega_c)^2} = 0 \tag{2.74}$$

$$\omega_c = \frac{1}{\sqrt{T_s\tau_i}} \tag{2.75}$$

Substituting Eq. (2.75) in Eqn. (2.73), the maximum phase margin is obtained as:

$$\Phi_m = \sin^{-1}\left(\frac{T_s-\tau_i}{T_s+\tau_i}\right) \tag{2.76}$$

The compensator gain has to be unity at the selected cutoff frequency. The compensator gain obtained from solving the amplitude of Eqn. (2.72) as shown below:

$$|G_{vol}| = |k_{pv}(\frac{T_s s+1}{T_s s})\frac{1}{(\tau_i s+1)}\frac{1}{Cs}| = 1 \tag{2.77}$$

The optimal gain at the cutoff frequency is expressed as:

$$k_{pv} = C\omega_c \tag{2.78}$$

So, regulating the load voltage is achieved by controlling of the magnitude of voltage components in DQ that is $V_s = \sqrt{v_{sd}^2 + v_{sq}^2}$ while the frequency is provided by voltage-controlled oscillator (VCO). The selected parameters and bandwidth of the designed inner current and outer voltage loops are given in Table 2.3.The parameters and transfer function of the inner current control are given in subsection 2.3.1.4.

Table 2.3. Controller's parameters for the outer voltage loop

System Parameters	Value	Controller Parameters	Value
Capacitor Filter	$C_f = 250uF$	Natural Frequency	$\omega_n = 1890rad/sec$
Switching Frequency	$f_s = 18.8k\ rad/sec$	Integral Time Constant	$T_s = 13.9\ msec$
Phase Voltage	$V_{sd} = 120V$	Controller Gain	$K_{pv} = 0.6699\Omega^{-1}$
Inner Time Constant	$\tau_i = 1msec$	Phase Margin	$\phi_m = 53^0$
Grid Frequency	$\omega_s = 377rad/sec$	Closed-loop Bandwidth	$400\ rad/sec$

Frequency domain is used to show the desired requirement of the outer voltage loop. Figs. 2.16 and 2.17 show the Bode plot of the open-loop and closed-loop of the outer voltage controller. The closed-loop bandwidth is 400 rad/sec which has slower bandwidth than the inner current loop. The Bode plot of open-loop shows that the system is stable according to the phase margin of 53^0.

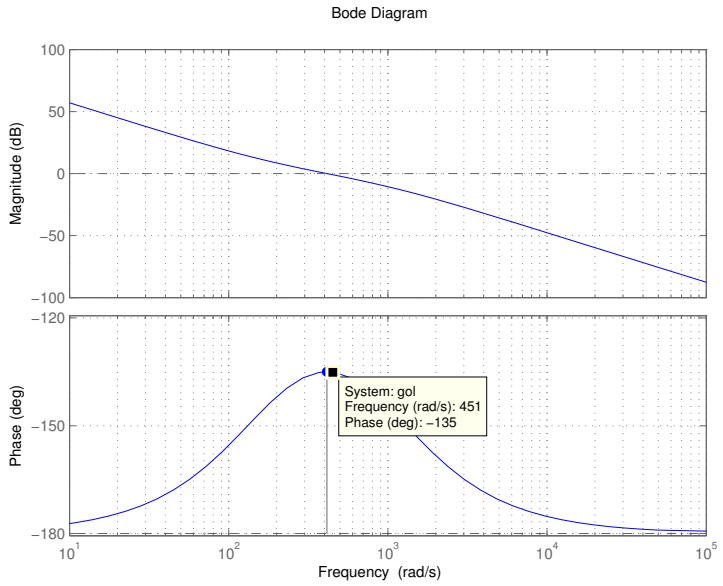

Figure 2.16. Bode plot of the open-loop of outer voltage controller

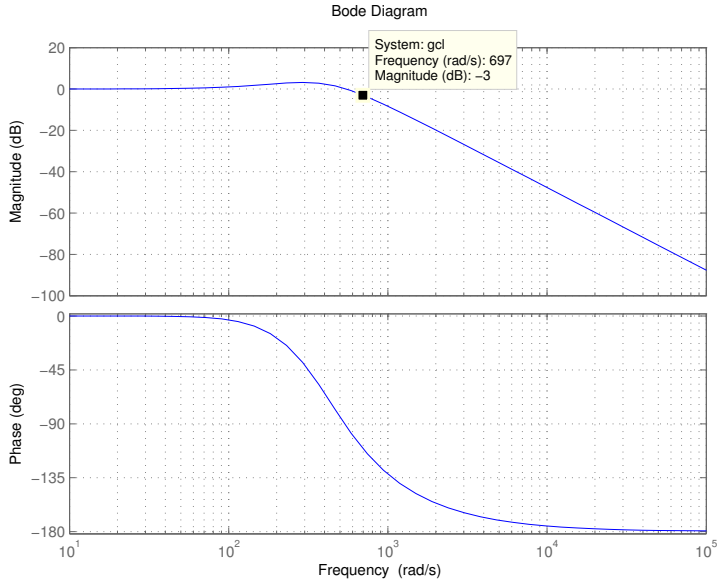

Figure 2.17. Bode plot of the closed-loop of outer voltage controller

CHAPTER 3

SMART INVERTER CONTROL FOR MOTOR DRIVES

This section provides a proposed strategy to control of motor drives for an autonomous microgrid. Two control methods have been proposed in this section which are soft start technique [1] and switching scheme [2]. These methods can solve the issue of blackstart and common mode voltage.

3.1 Review of Motor Drives

3.1.1 Blackstart Phenomena

Induction motors occupy almost 50% of all loads in real applications [35]. These loads require high current during starting up period from stand still. When a weak microgrid is presented, high reactive power is consumed during the transient state. This reactive power impacts on the voltage profile. When a DER unit could not achieve the requirements of the induction motor's load, blackstart problem is presented. Reducing applied voltage during large induction motor startup in a weak microgrid is an important approach to avoid a blackstart issue. Different methods have been used to reduce the negative effect of starting motor's load. In a case of small motors, direct online (DOL) algorithm is used because small motors consume low reactive power and current which may not produce voltage dip on the system. It also can connect starting capacitor in parallel to the motor to compensate the reactive power demand during start-up condition. This capacitor improves the power factor and generates leading current as well as improve the efficiency and reducing transient time. In a case of large induction motors, reducing applied voltage or providing higher reactive power are needed to avoid blackstart issues of the motors [35].

[1] This chapter was published in Power & Energy Society General Meeting, 2015 IEEE 2015 July 26 (pp. 1-5). Permission is included in Appendix A.

[2] This chapter was published in North American Power Symposium (NAPS), 2015 Oct 4 (pp. 1-5). IEEE. Permission is included in Appendix A

Direct online connection of large induction motor could provide high inrush current and reactive power demand. Starting induction motor may affect other loads and even the system at PCC regarding voltage dip during this transient period [69]. Conventional methods have been used to reduce inrush current during starting the motor such as passive series components, star-delta connection, auto-transformer and shunt capacitor. All these methods have different drawbacks including frequent maintenance, cost of installations and services, power dissipating etc [70].

Soft starting method is used to control of starting of the motor and provides lower current and reactive power as well as avoids the voltage dip. It also decreases the need for high reactive current as well as eliminate the negative impact of inrush current. The concept of soft start includes increasing the voltage linearly with time until the motor begins to reach steady state speed at full rated voltage. This technique can be achieved by applying smart inverter's technique to provide ramp voltage and fixed frequency. By doing so, the smart inverter can solve the issue of blackstart of the motor as well as achieve microgrid's stability in a case of a weak autonomous microgrid. This function is added to the smart inverter which is activated when blackstart issue occurs.

3.1.2 Common Mode Voltage (CMV) Concept

Several pulse width modulation (PWM) methods have been developed to control the switching pulses of VSC and smart inverter [71]. Sinusoidal pulse width modulation (SPWM) and space vector pulse width modulation (SVPWM) are commonly used methods to control of switching state patterns of VSC. The advantages of implementing SPWM and SVPWM include good ac and dc current ripple, low switching frequency and high voltage linearity range [72]. However, they generate high common mode voltage (CMV) which may produce some problems to the system. These issues cause a failure in the stator winding insulations, bearing currents and high-frequency leakage current on the motors as well as affect the operation of circuit breakers of the loads [73].

Common mode voltage (CMV) is defined as the potential difference voltage between star point of the load and the center of the $C_{\mathrm{dc-link}}$ of the DC bus. The CMV for VSC is given as:

$$V_{com} = \frac{V_{ao} + V_{bo} + V_{co}}{3} \tag{3.1}$$

Generally, CMV equals zero when the load receives balanced three-phase sinusoidal phase voltages. Since VSC generates high current harmonics, high CMV is produced on the motor load's terminal. Several approaches have been recently investigated to mitigate and eliminate CMV [36, 37]. The authors proposed hardware devices to eliminate CMV. However, using hardware elements and filters require additional complexity and cost to the system which is not a recommended solution for economical perspective. Besides, applying software method is an effective solution to reduce common mode voltage (RCMV) at no cost.

3.2 Smart Inverter Topology

A schematic design and controller of an autonomous microgrid are shown in Fig. 3.1. The DER unit consists of a distributed generator (DG), VSC, RLC filter, breakers and induction motor's load. The dc voltage source is assumed to be a controllable power source that provides constant dc voltage. The dc voltage source can be represented as battery bank, photovoltaic (PV) array or fuel cell. The VSC is controlled by a modern control algorithm such as PWM to be accommodated with the operation condition of the system. The system also has a three-phase passive filter for better reduction of current harmonic as shown in Fig. 3.1.

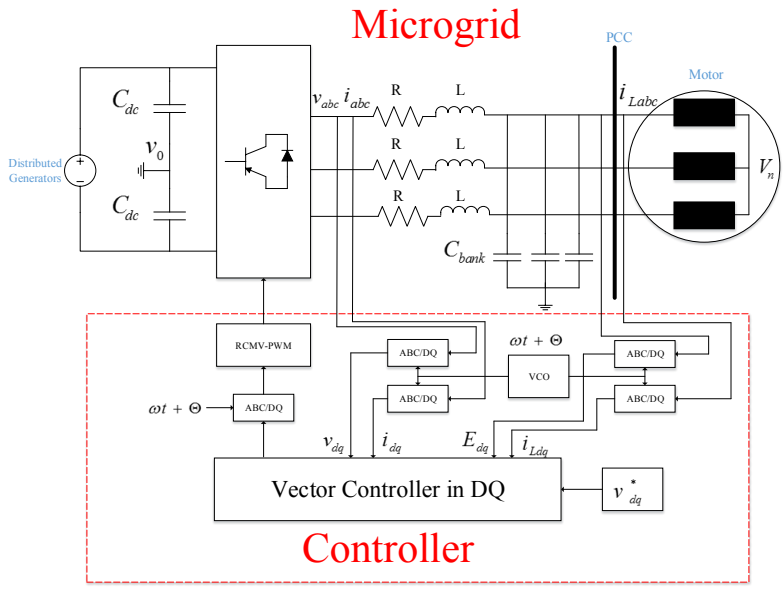

Figure 3.1. General controller scheme and topology of motor drives

3.3 Controlling Challenges of Induction Motor

3.3.1 Induction Motor's Blackstart

Starting of an induction motor from standstill at full rated voltage consumes high starting current. This high current is calculated from the relationship between the motor's stator voltage and current as follows:

$$I_{\text{stator}} = \frac{V_{\text{stator}}}{Z_{\text{thevenin}}} = I_{\text{stator}} + I_{\text{rotor}} \tag{3.2}$$

$$Z_{\text{stator}} = R_{\text{stator}} + jX_{\text{stator}} + X_m//(\frac{R_{\text{rotor}}}{\text{slip}} + jX_{\text{rotor}}) \tag{3.3}$$

where I_{stator} and I_{rotor} are the stator and rotor currents of induction motor, respectively; V_{stator} and Z_{stator} are the voltage and impedance of the motor's stator; slip is the difference between the motor's rotor speed and the stator's synchronous speed.

It can be seen from Eqn. (3.3) that the high starting current depends on to the value of the rotor resistance. The slip of the induction motor equals 1 per unit and the rotor resistance has low value at standstill. Therefore, the rotor current is high as well as the stator excitation current. This inrush current is almost five to eight times the rated current at steady state [74].

In order to investigate the impact of the starting current on the microgrid, the relationship between the voltage source and the voltage at PCC based on the line current is given as:

$$I_{\text{line}} = \frac{V_s - V_{\text{pcc}}}{X_{line}} \tag{3.4}$$

In case of a strong system where the line impedance is low, the starting current may not affect the voltage at PCC. However, if the line impedance is high, starting current can negatively impact on the magnitude of the load voltage. This negative impact may produce voltage dip on the system based on the power flow equation as:

$$Q_s = \frac{V_s V_{pcc} \cos(\theta_s) - V_{pcc}^2}{X i_{line}} \tag{3.5}$$

According to [75], the AC system is classified as a weak system if the Short Circuit Ratio (SCR) is less than 2 per unit. Consequently, if the induction motor is connected to weak system, the voltage at PCC is sensitive to any changes in the load. Therefore, the DER unit has to provide a reactive power in order to mitigate the impact voltage dip.

3.3.2 Induction Motor's Switching Scheme

Two main methods are used to control of switching patterns for VSC using pulse width modulation technique (PWM). Scalar and space vector techniques provide almost the same equivalent performance in case of practical and theoretical implementations. A scalar method such as SPWM is commonly used for controlling VSC due to its simplicity. Vector algorithm such as SVPWM is preferable due to large utilization voltage linearity [76].

The concept of SVPWM consist of implementation complex voltage vector states to approximate the reference voltage vector in a sampling time period. This technique provides controlling the sequence of switching states. The vector transformation of two-level three phase VSC into $\alpha\beta$ domain contains eight vector states, $2^3 = 8$, which include six active states and two zero states.

The representation of space vector is illustrated as following:

$$\overrightarrow{V_s}(t) = \frac{2}{3}[e^{j0}V_a(t) + e^{j\frac{2}{3}\pi}V_b(t) + e^{j\frac{4}{3}\pi}V_c(t)] \tag{3.6}$$

The reference signal has the following definition in space vector domain:

$$\overrightarrow{V_s} = \frac{2}{3}\sqrt{2}|V|e^{j(\omega t+\theta)} \tag{3.7}$$

The reference voltage V_s is calculated based on the transformation of V_{abc} into vector signals on rotating reference frame DQ. The magnitude and angle of the reference signal is given as:

$$|\vec{V_s}| = \sqrt{(V_d)^2 + (V_q)^2} \tag{3.8}$$

$$\alpha = \tan^{-1}(\frac{V_q}{V_d}) \tag{3.9}$$

The space vectors of VSC divides the complex domain into six vectors. These six active vectors $(V_1, V_2, V_3, V_4, V_5, V_6)$ and the two zero vectors $(V_0,\ V_7)$ are fixed in the rotating reference frame during sampling time and they divide the complex plan into six sectors. The fundamental signal is rotating at speed of fundamental angular speed ωt with a constant magnitude.

The reference vector in SVPWM can be synthesized by at least two active vectors and a zero vector. In order to reduce switching losses, two adjacent active vectors and two zero vectors are adapted to synthesize the reference vector as shown in Fig. 3.2 a) where the reference vector is located at sector one.

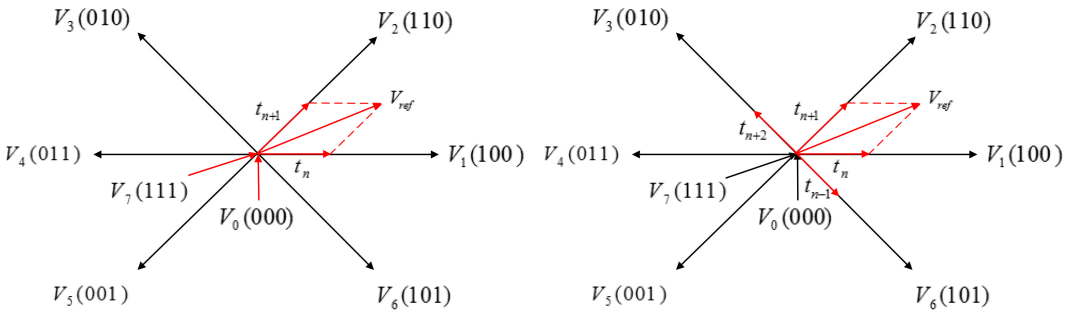

a) SVPWM b) AZPWM

Figure 3.2. SVPWM and AZPWM representation at $\alpha\beta$ reference frame

3.4 Proposed Methods for Motor Drive

3.4.1 Soft Start

The high starting current in Eqn. (3.2) cannot be avoided when the induction motor is connected to the full rated voltage. A possible solution to lower the starting current is to decrease the applied stator voltage. It is proposed to linearly increase the stator voltage from zero up to full rated voltage. Therefore, voltage dip can be avoided in case of weak system as well as limiting the starting current.

Large industrial motor is examined in this research to investigate its impact on the system. The parameters of the stator and rotor impedances are obtained from type-2 motor [77]. Fig. 3.3 shows the relationship between the starting current and consumed reactive power against the motor slip

during induction motor's startup using DOL method. It is observed that the starting current and reactive power are high when the slip equals 1 which indicates the motor starts from a standstill. So, the motor consumes high starting current according to Eqns. (3.2) and (3.3). The starting current and reactive power will be decreased when the motor reaches its steady state where the slip is approximately equal to zero. The maximum starting current and reactive power consume almost 6 per unit and 3 per unit respectively as shown in Fig. 3.3.

The proposed method depends on increasing the voltage linearly from zero to full rated voltage. The slip will change from one to zero which indicates that the operational state of the motor will change from standstill to steady state. Consequently, the starting current will increase linearly with the voltage until the slip reaches its steady state value. So, the proposed method can limit the maximum starting current. The relation between the current and voltage of the motor is shown in Fig. 3.4 where the starting current is lower than its maximum value in case of DOL method and then decreases to its steady-state value. It also can be concluded that the maximum current can be limited at 4 per unit instead of 6 per unit when a type-2 motor is used.

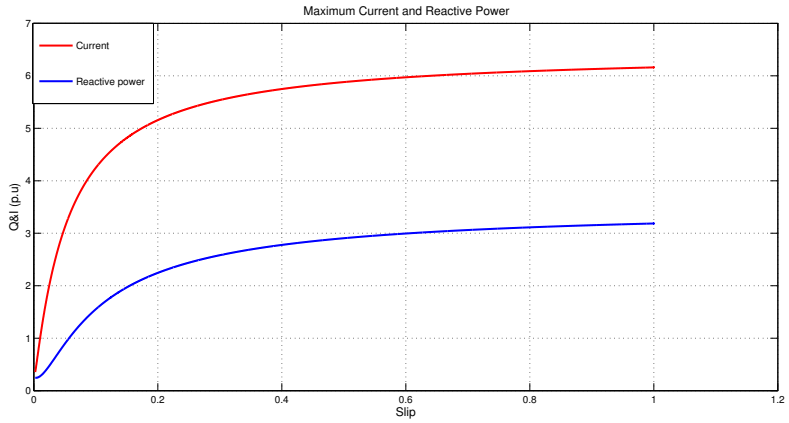

Figure 3.3. Starting current and reactive power characteristic using DOL method

3.4.2 Active Zero Pulse Width Modulation (AZPWM)

The main reason of high CMV is selecting zero state vectors to synthesize the reference signal of switching patterns of a smart inverter. SVPWM divides the zero state time between the two zero states to synthesize the reference signal. Zero state vectors actually generate high CMV which

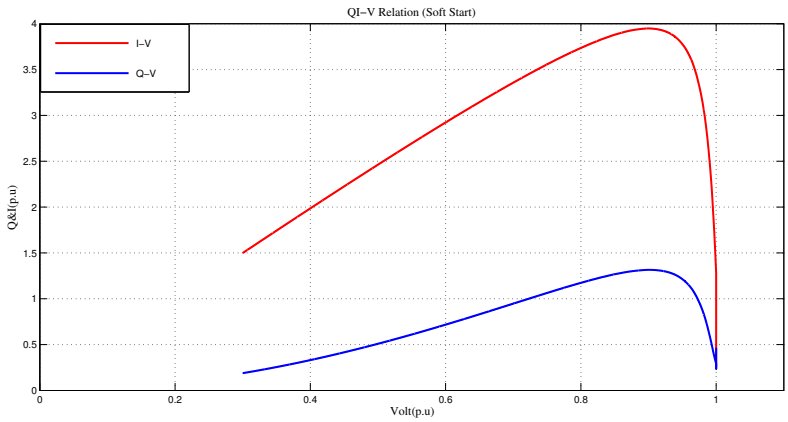

Figure 3.4. Current and reactive power relation with stator voltage at soft start

reaches up to 50% of V_{dc} while active state vectors produce 17% of V_{dc} [73]. So, avoiding selecting zero save vectors is essential to reduce CMV.

Reduce CMV-PWM implements only active vectors and avoids selecting zero-vectors which are the cause of CMV. The proposed algorithm aims to select only active space vectors to represent the reference signal. Active zero state pulse width modulation (AZPWM) algorithm implements the same concept of SVPWM to synthesize the reference signal. Besides, it selects two opposite active vectors with equal time durations to synthesize the reference signal instead of zero vectors as shown in Fig. 3.2.b).

The performance of AZPWM depends mainly on the voltage utilization level M_i. The magnitude value of the six active vectors, modulation index, and dwelling time of each sector are given as:

$$V_n = \frac{3}{2}|V_{dc}|e^{(n-1)\frac{\pi}{3}} \tag{3.10}$$

$$M_i = \frac{|V_{ref}|}{V_{steps}} = \frac{\pi V_{ref}}{2V_{dc}} \tag{3.11}$$

$$T_n = \frac{2\sqrt{(3)}T_s MI}{\pi}\left(\sin(\frac{n\pi}{3})\cos\theta\right) - \left(\cos(\frac{n\pi}{3})\sin\theta\right) \tag{3.12}$$

$$T_{n+1} = \frac{2\sqrt{(3)}T_s MI}{\pi}\left(-\sin(\frac{(n-1)\pi}{3})\cos\theta\right) - \left(\cos(\frac{(n-1)\pi}{3})\sin\theta\right) \tag{3.13}$$

$$T_s = T_a + T_b + T_{n-1} + T_{n+2} \tag{3.14}$$

$$T_{n+2} = T_{n-1} \tag{3.15}$$

The representation of reference vector depends on the notion of volt-seconds balance rule. The reference vector in Fig. 3.2.b) is synthesized by two adjacent active vectors and two opposite active vectors as shown in Eqn. (3.16):

$$\overrightarrow{V_s}T_s = \overrightarrow{V_n}T_n + \overrightarrow{V_{n+1}}T_{n+1} + \overrightarrow{V_{n+2}}T_{n+2} + \overrightarrow{V_{n-1}}T_{n-1} \tag{3.16}$$

where T_n, T_s, and V_n are dwelling times, sampling time and selected vector, respectively.

One more important segment in reducing switching losses is to determine the switching sequence. In [78], it is claimed that the time sequence of the dwelling time based on 7-segment method has lowest total harmonic distortion. Each switch has to change its states once at every switching period to achieve optimal harmonic performance and lowest switching frequency. The concept of 7-segment is shown in Fig. 3.5 for both SVPWM and AZPWM algorithms. Fig. 3.5 shows the comparison between SVPWM and AZPWM according to CMV. It can be seen from Fig. 3.5 that CMV can be reduced if only active vectors are selected. The switching sequences for SVPWM and AZPWM at each sector are given in Table 3.1.

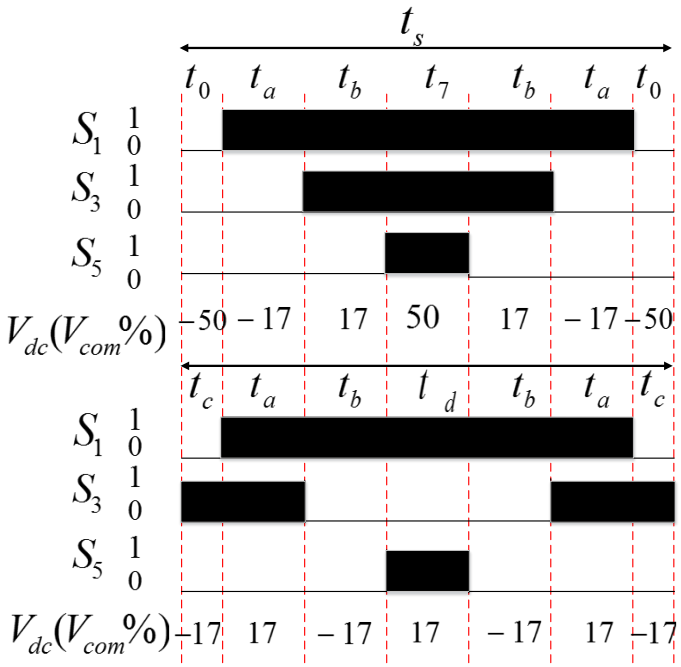

Figure 3.5. Switching sequence based on 7-segment method at sector one

Table 3.1. Switching sequences for SVPWM and AZPWM1 at different sectors

Sector	SVPWM	AZPWM
1	0127210	3216123
2	0237320	4321234
3	0437340	5432345
4	0457540	6543456
5	0657560	1654561
6	0617160	2165612

3.5 Simulation Results

3.5.1 Soft Start Algorithm for Blackstart Issue

Blackstart of the induction motor has been validated by PSCAD/EMTDC. VF controller of the smart inverter based autonomous mode is applied and examined using simulation software. The DOL method is first applied when the induction motor's load is connected to a weak system. A solution of blackstart is then evaluated by using soft start technique function of a smart inverter to drive the motor's load. Different voltage ramp cases are applied to decrease the maximum starting current. The overall scheme of the microgrid is shown in Fig. 5.1 and the rated parameters of the system are presented in Table 3.2.

Table 3.2. Parameters of an autonomous microgrid to operated the motor drives

Microgrid Components	Values	Induction Motor	Values
L	2.14 mH	P_{IM}	20 HP
C	100 uF	V_{IM}	220 V
R	1 Ω	Slip	0.028
V_{dc}	500 V	Pole	4
$C_{\mathrm{dc-link}}$	250 uF	R_{stator}	0.1062 Ω
P_{dc}	30 kW	R_{rotor}	0.0764 Ω
$F_{\mathrm{switching}}$	3000 Hz	X_{stator}	0.2145 Ω
$V_{L,rms}$	110 V	X_{rotor}	0.2145 Ω
		X_m	5.834 Ω

Voltage dip may occur when the induction motor is connected to a weak system. For example, the microgrid has SCR equals 2 per unit which indicates the system is weak. In order to validate the

proposed method, the microgrid is first examined when the induction motor is directly connected to a weak system. At $1sec$, the load breaker is closed and the motor receives a full rated voltage. The motor's parameters and the system's behavior is shown in Fig. 3.6 when DOL method is applied. It can be recognized that the starting current is very high which is almost 7 times the rated current. This high current produces voltage dip on a weak system. According to IEEE, the standard voltage dip should not be lower than 80% of the rated voltage when the motor is directly connected to the system. Since the induction motor load is connected to a weak system, voltage dip occurs which is about 70% lower than the recommended voltage as shown in Fig. 3.6.

The VF controller based on soft start is examined with a voltage ramp response. The induction motor is connected to the microgrid and the behavior of the induction motor is shown in Fig 3.7. It can be seen that the torque and speed of the induction motor are smoothly increased which provides more efficiency to the torque. The stator voltage ramps smoothly until it reached the rated value of induction motor as shown in Fig. 3.7. So, it is observed that the controller can limit the high starting current of the induction motor. It also provides a solution for voltage dip and more efficiency to the motor.

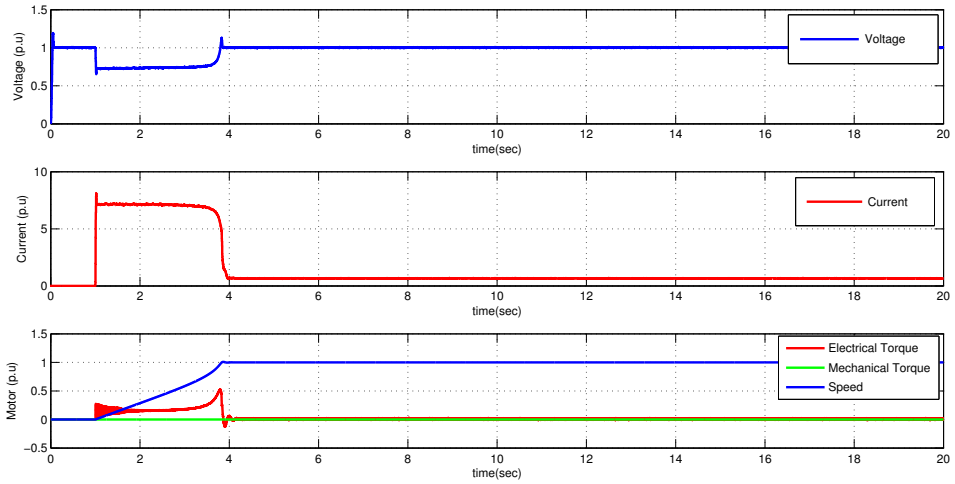

Figure 3.6. Microgrid behavior using DOL method

Different voltage ramp cases are applied to limit the maximum starting current as given in Table 3.3. The voltage magnitude is set at rated phase voltage while the transient times are varied to

limit the starting current. The trade-off between the maximum starting current and the transient time needs to be considered. For instance, long transient time leads to decreasing the maximum starting current. Therefore, limiting the current has to meet the requirements of the system. In this case, the maximum starting current should be lower by 80%. In table 3.3 the requirement of the maximum starting current is achieved where the transient time of the voltage is 19 seconds. This function of a smart inverter can reduce the blackstart of induction motor at a weak microgrid.

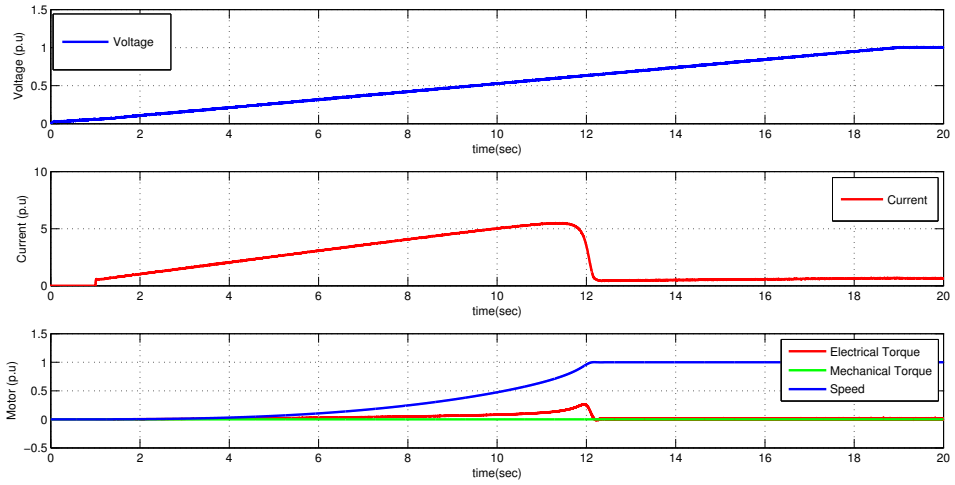

Figure 3.7. Microgrid behavior using soft start method

Table 3.3. Different cases of voltage ramp to operate a smart inverter

Voltage Ramp	T_{settling}	I_{max}	I_{max} %	T_{max}
1	5 sec	7.0 p.u	100 %	0.50 p.u
2	9 sec	6.7 p.u	95 %	0.45 p.u
3	13 sec	6.1 p.u	87 %	0.35 p.u
4	19 sec	5.5 p.u	78 %	0.25 p.u

3.5.2 AZPWM Algorithm for CMV Issue

The designing of VF vector control based on AZPWM of VSC is achieved in PSCAD/EMTDC. In order to validate the method, an induction motor is added at no load. SVPWM and AZPWM algorithm are studied to compare the impact of CMV on the load as well as investigate the robust-

ness of the controller on load's disturbance. The rated parameters of the microgrid are given in Table 3.2. The comparison of the methods are given in the simulation plots.

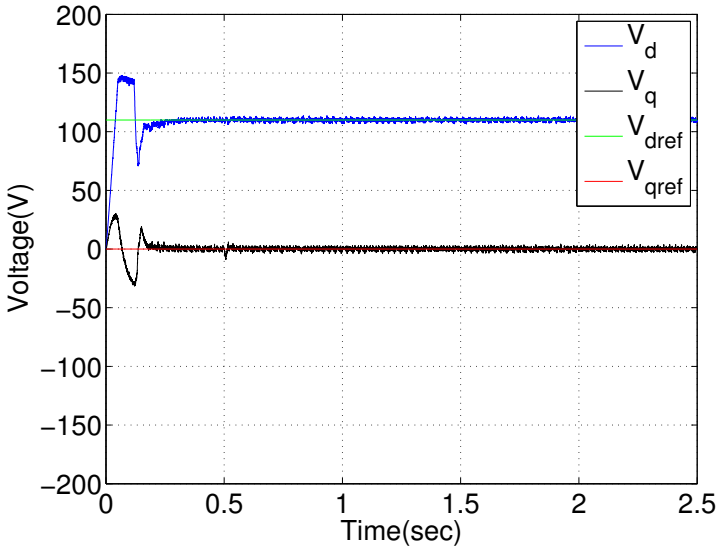

Figure 3.8. Output voltage of the microgrid using VF controller

The behavior of VF controller of smart inverter is shown in Fig. 3.8. The voltage V_d sets to equal the nominal voltage while the voltage V_q equals zero. Fig. 3.8 verifies that the controller of the smart inverter is working. The induction motor is connected at $0.5sec$ to represent the effect of CMV on the system as well as investigate the capability of the controller. From the Fig. 3.8, it can be observed the VF controller can realize the voltages at DQ-axis to the reference values which is $110V$. It also shows that the output voltage follows the reference signal in less than $0.3sec$. This figure verifies that the designed controller can provide disturbance rejection, high reliability, and good dynamic response.

Two common PWM algorithms are used to investigate the behavior of CMV which are SVPWM and AZPWM as shown in Figs. 3.9 and 3.10. The switching frequency is set at 3 kHz for both methods. The modulation index is kept constant at 0.7 since the voltage is fixed for the microgrid. Figs. 3.9 and 3.10 show the behavior of CMV when SVPWM and AZPWM algorithms are implemented. They also provide phase line current wave and motor's torques and speed. Figs. 3.9 and 3.10 show that the AZSPWM algorithms can reduce CMV variations by comparing with

the SVPWM algorithm. The reduction of CMV can be achieved by 17%. AS shown in Fig. 3.10, the proposed AZPWM can reduce the CMV without affecting the behavior of the smart inverter or changing the hardware components of the system. The simulation plots verify the proposed approach in this research. This function of operating PWM technique of the smart inverter can be implemented at any connection of the microgrid.

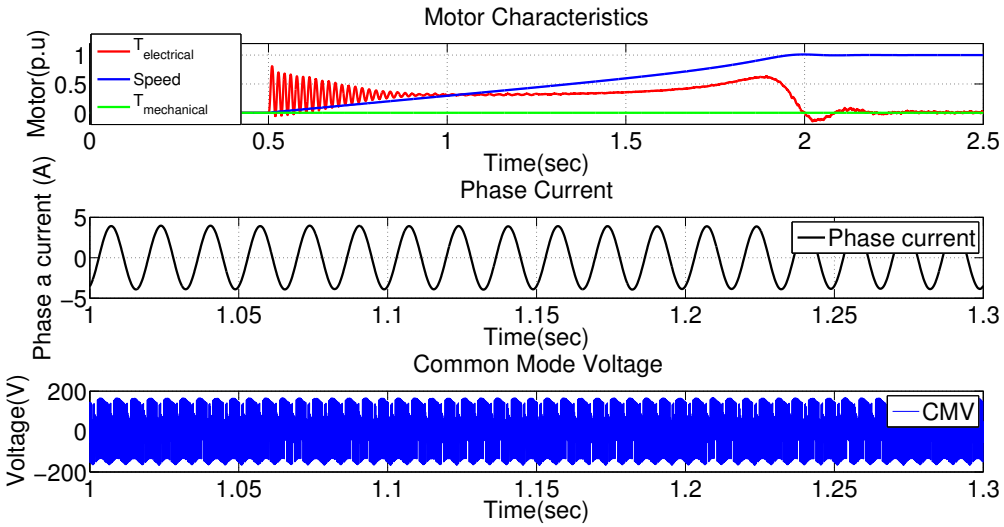

Figure 3.9. SVPWM method to operate smart inverter at autonomous microgrid

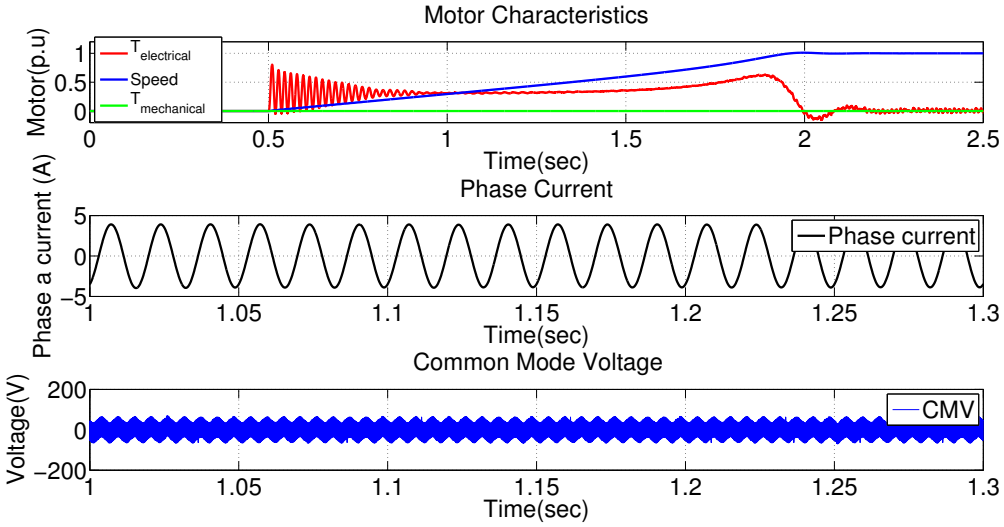

Figure 3.10. AZPWM method to operate smart inverter at autonomous microgrid

CHAPTER 4

CONTROL OF HYBRID CONVERTER FOR PV STATION

4.1 Introduction

Generating electric power from renewable energy resources instead of conventional energy sources gains more and more interesting. The need for smaller financial commitments and larger system liability necessitate utilizing microgrid to generate energy [79]. Photovoltaic (PV) among other microgrid's renewable resources such as wind and fuel-cells, shows a leading promise renewable energy at residential and commercial applications. The benefits of adopting PV technology include the availability of energy resource, low operational and maintenance cost, and reduction of carbon dioxide emissions. However, the total cost and efficiency of installed PV system are still a major issue [10, 80, 81]. Another issue of using PV system is the power requirements of the microgrid. Most of the residential and commercial applications involve both dc and ac loads on the same architecture such as hybrid electric vehicle and ships, house appliances, and dc nanogrid [81, 82]. In this case, multi-output converter dc/dc converters and cascaded voltage-sourced converter VSC stages are used to provide sufficient power to different load4. However, this technique may increase the complexity and cost of designing PV systems.

The environmental and economic advantages of a plug-in hybrid electric vehicle (PHEV) lead to the increase in a number of production and consumption. The U.S. Department of Energy forecasts that over one million PHEVs will be sold in the U.S. during the next decade [24]. Even most of PHEV's customers prefer to charge their vehicles during night time, there is a considerable PHEV load during the peak hour demand. A large-scale penetration of PHEVs may add more pressure on the grid during charging periods. One possible solution to solve this issue is to upgrade the distribution system to meet the peak demand of the PHEV's loads. However, this solution

may need additional investment cost as well as result in capacity surplus during normal operation. Another feasible solution is to design a smart charging station integrated with photovoltaic (PV) system which can minimize the load power stress the grid as well as reduce the charging price and installation cost.

The impact of PHEVs on the utility grid can be determined by three main challenges which include charging characteristics, charging timing, and PHEV's penetration level [83–85]. The comparison of different PHEV charging characteristics and techniques are reviewed in [25, 26]. To provide a fast charging time for PHEVs, various methods have been proposed in the literature [86–88]. Even the proposed topologies can provide fast charging time, they mainly depend on the main grid to charge the PHEV's battery which may generate stability issues during peak load period. The possible solution is to install PV charging stations which are analyzed in [89, 90]. A proposed architecture and controller for the PV charging station have been presented in [28] and [27] to provide the main charging source from PV while the grid supports the charging process. However, the authors did not discuss the ways to reduce the stress on the grid when high penetration level of PHEV appears. Another proposed PV charging station is presented in [91] by investigating the stability aspects of dc distribution system. However, the derived controller increases the complexity and cost of the system. In aforesaid papers, the PV charging station requires controlling at least three different power electronic converters to charge the PHEV's batteries. Each converter needs an individual controller, which increases complexity and power losses of the system. Consequently, it is urgent to investigate multi-port converters to reduce the number of converting stages and improve the overall efficiency.

In order to overcome the aforementioned issues, a novel structure of hybrid converter is presented [38]. The advantages of implementing hybrid converter are listed below [38, 92, 93]:

- 1- It has the capability to protect shoot-through behavior when both switches are closed at the same time. The availability of inductance gives the advantage to be immune to induced EMI on any converter's leg which increase the reliability of the system.

- 2- Hybrid converter does not require dead time feature which decreases current harmonics.

- 3- The power density is higher due to the integrated dc and ac output on a single architecture.
- 4- Hybrid converter has a bidirectional feature which provides flexibility to power flow.
- 5- PWM of the hybrid converter can be operated at a high switching frequency, usually above 5 kHz, which generates less harmonics output waveform.

In order to decrease the number of switching stages, the inverse Watkins-Johnson the technique is proposed in [94] by supplying power simultaneously to dc and ac loads. The switched boost inverter improves the concept of Z-source topology by generating two output ac and dc powers from a single dc power [95]. Single-phase and three-phase of hybrid boost converters (HBC) that can integrate dc power source, dc load and ac load for a microgrid are proposed in [38] and [40], respectively. Recent research in [39] also suggests that a hybrid single-phase converter can be applied in grid-connected applications. In all aforementioned manuscripts, the authors assumed that the hybrid converter is connected to a stiff dc voltage source and supply power to fixed dc and ac loads. They also did not consider the dynamic behavior of the renewable resources and loads on the controller design as well as the power flow management.

This section makes two major contributions to the area of modeling and controlling of PV charging station using three-phase bidirectional hybrid boost converter (HBC) topology. The paper is first modeling and designing a smart controller to charge PHEVs by integrating PV array, PHEV's battery, and utility grid. The dynamic behavior of maximum power point tracking algorithm (MPPT) and PHEV's battery are considered in modeling the charging controller as comparing with the hybrid converters topologies in [39,94,95]. The second contribution includes improving the charging characteristics when high penetration of PHEV. Comparing with the papers in [27, 28], the bidirectional advantages of the three-phase HBC based PV charging station can solve the stability issues during peak load power by generating energy from a grid-connected PV or the utility or both. In contrast with [91], this paper develops a smart charging technique which has the capability for MPPT algorithm, dc-link voltage regulation, and reactive power control. Fig. 4.1 shows the proposed PV charging station can integrate a dc/dc boost converter and a three-phase VSC in a single structure.

4.2 Three-Phase HBC-based PV Charging Station

A three-phase HBC uses the same amount of switches as a two-level voltage source converter (VSC). However, the HBC can realize both dc/dc conversion and dc/ac conversion. As a comparison, Fig. 4.1 shows the conventional PV charging station where a dc/dc boost converter and a three-phase VSC are used to integrate the PV system, the PHEVs, and the ac grid. A three-phase HBC replaces the two converters: the dc/dc boost converter and the dc/ac three-phase VSC to decrease the energy conversion stages and the power losses of the PV charging station. Fig. 4.1 shows the HBC-based PV charging station's topology. The main components of the configuration of the PV charging station consist of PV array, three-phase bidirectional HBC, ac grid, off-board dc/dc converter, and PHEV's batteries.

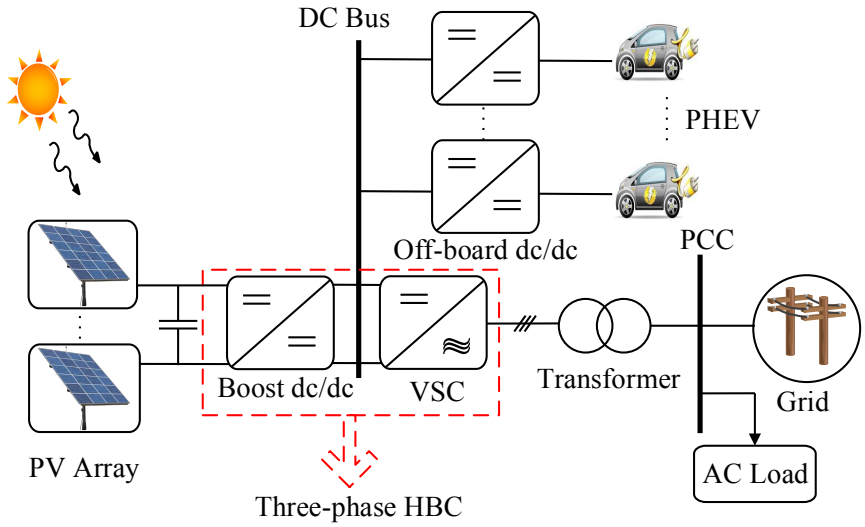

Figure 4.1. Architecture configuration of a PV charging station

The system is composed of a PV array, a dc system, a three-phase ac system, and the interfacing three-phase HBC as shown in Fig. 4.2. The PV side includes a large inductance to achieve continuous condition, and dc-link capacitance to decrease the voltage ripple. The dc side includes a switching diode, a dc bus for PHEV connection, a dc capacitor to eliminate the output current ripples, an off-board unidirectional dc/dc buck converter, and PHEV batteries. The ac system

includes a three-phase RL filter, a step-up transformer, and the point of common coupling (PCC) bus that connects the PV station to the main grid.

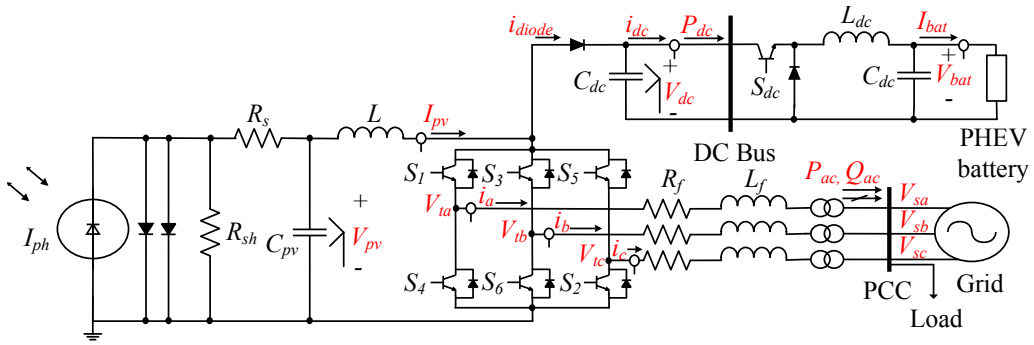

Figure 4.2. Detailed model of PV charging station

The PV array is composed of connecting series cells and parallel strings. Each PV cell has specific characteristics depending on the type and designing criteria. PV models depend mainly on Shockley diode equation [96, 97]. PV can be modeled as a photon-generated current source in parallel with a two-diode system and a shunt resistor, R_{sh}, as well as in series with a series resistor, R_s. The mathematical equations of two-diode PV cell are given in [96]. It is worth to mention that there are several configurations of PV generation system such as multi-string and centralized topologies. Considering cost and efficiency, conventional PV system generally uses multi-module dc-dc converters to activate maximum-power-point-tracking (MPPT) algorithm and central VSC to generate ac power [80]. Comparing with the conventional PV system, the HBC can improve the multi-string topology of PV generation system by integrating dc/dc converter and three-phase VSC in a single structure. It also can apply MPPT algorithm, regulate dc voltage, and generate reactive power support. So, using central HBC with PV array becomes a more attractive technique for PV applications such as PV charging station. HBC-based PV charging station has also the capability to operate at medium and high power ratings of such PV power plants. Since a single IGBT-based VSC has the capability to operate at high voltage rating (e.g., voltage limitation up to 1.2 kV [98]), the HBC configuration can be operated for high voltage PV power plans.

A schematic design and operation of three-phase HBC is shown in Fig. 4.3 where the main switch of a step-up dc/dc converter is replaced by three-phase two-level VSC. The switches of a

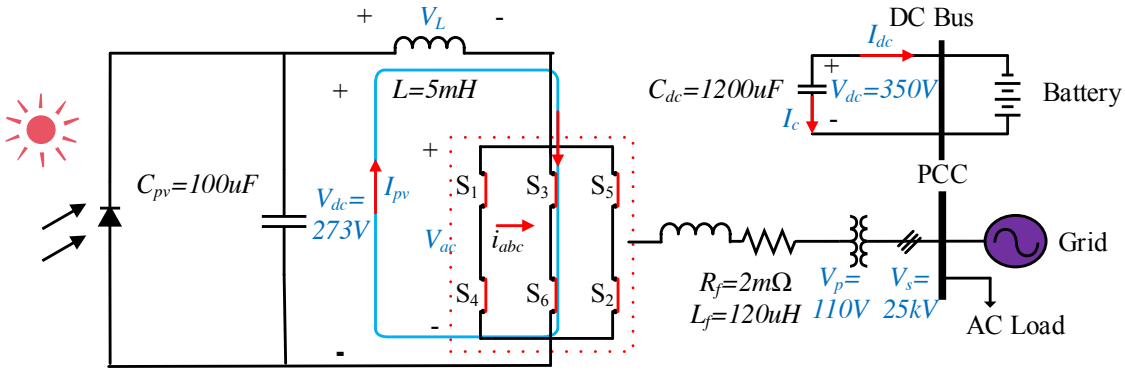

(a

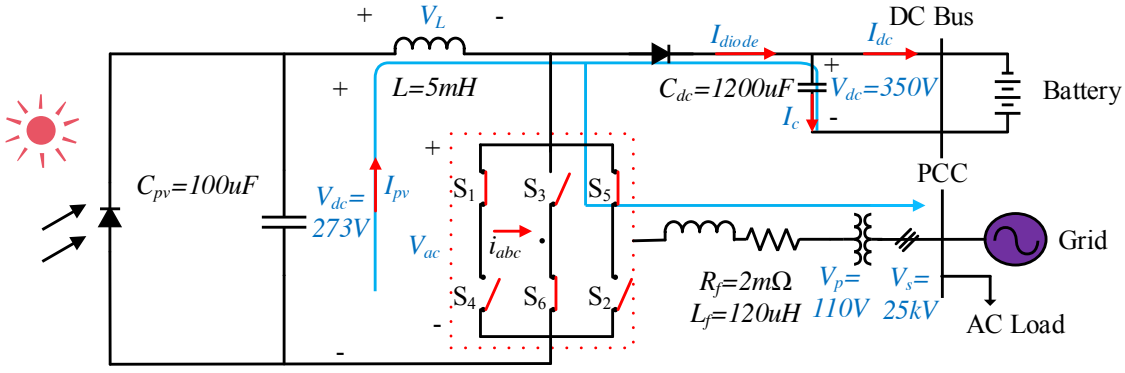

(b

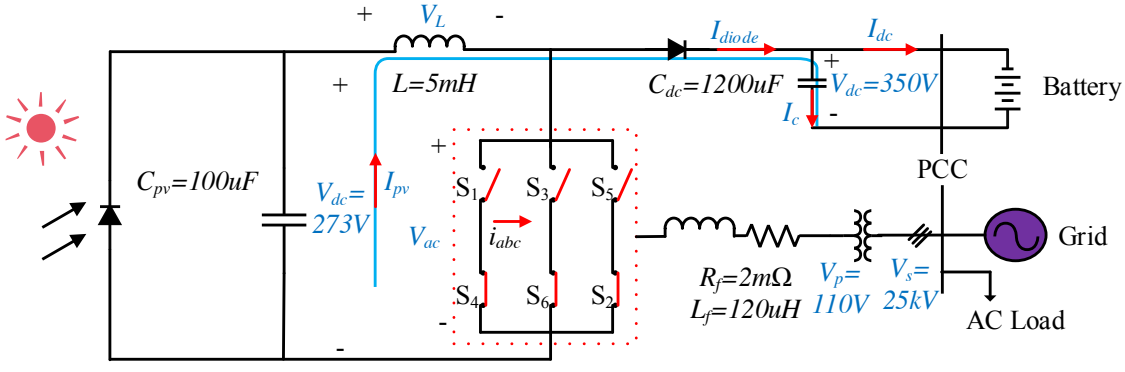

(c

Figure 4.3. The three operational intervals of the three-phase HBC

VSC are responsible for providing ac output as well as step-up dc input voltage to generate dc output. Three main operational phases of three-phase HBC are defined depending on each switching states of the three-phase HBC. The traditional dc/dc boost converter is operated in two modes which are switching on and off modes. Besides, conventional VSC is operated on active and zero periods where the power flow can have a value or equal zero. The three-phase HBC integrates the operational phases of VSC and dc/dc converter into three main modes. The three intervals include shoot-through (ST) mode, active mode (A), and zero mode (Z) which are shown in Fig. 4.3.

4.2.1 Shoot-Through Phase (ST)

This phase boosts the input dc voltage by closing both switches of any VSC's leg or all legs. The control dc signal D_{st} regulates the duration period of this phase. The power flow is shown in Fig. 4.3, a) where no output power flows to the dc bus nor PCC. The diode is operated as reverse bias and the voltage drop on VSC legs equals zero. The purpose of this phase is to boost the input voltage by charging the main inductance. So, the VSC can generate output ac and dc powers higher than the PV source power.

4.2.2 Active Phase (A)

The operational state of three-phase HBC on this phase is similar to conventional VSC. However, the output power flows to both dc and ac buses. The only difference is that the input current into three-phase inverter is continuous. The active phase is shown in Fig. 4.3, b) where the dc and ac loads share the input power for PV. The diode is holding both input inductor current and ac phase current in this phase and three-phase HBC switches are switching simultaneously to generate dc and ac power.

4.2.3 Zero Phase (Z)

When all top or bottom switches of the HBC are opened, zero phase is activated and no power flow to the ac output. The diode is holding only the input current from the inductance as shown in Fig. 4.3, c). This phase is similar to switching off period of a conventional dc/dc boost converter.

A steady-state analysis of the three-phase HBC provides a clear understanding of the operating principles and limitation of the system. The steady-state operation of the three-phase HBC is similar to boost converter where ST period represents "On" interval and non-ST period states "Off" interval. However, the switching state of the three-phase HBC involves two additional periods on a non-ST interval which are A and Z intervals. The behavior of main dc and ac components during sampling time is illustrated in Fig. 4.4. It can be seen from Fig. 4.4 that the inductance voltage and current are similar to conventional boost converter as well as the output dc voltage. However, the voltage drop and current on VSC are different from that main switch of boost converter as well as the output dc current. The reason of this diversity is that Z period affects the output ac and dc power where no power transfers to the microgrid.

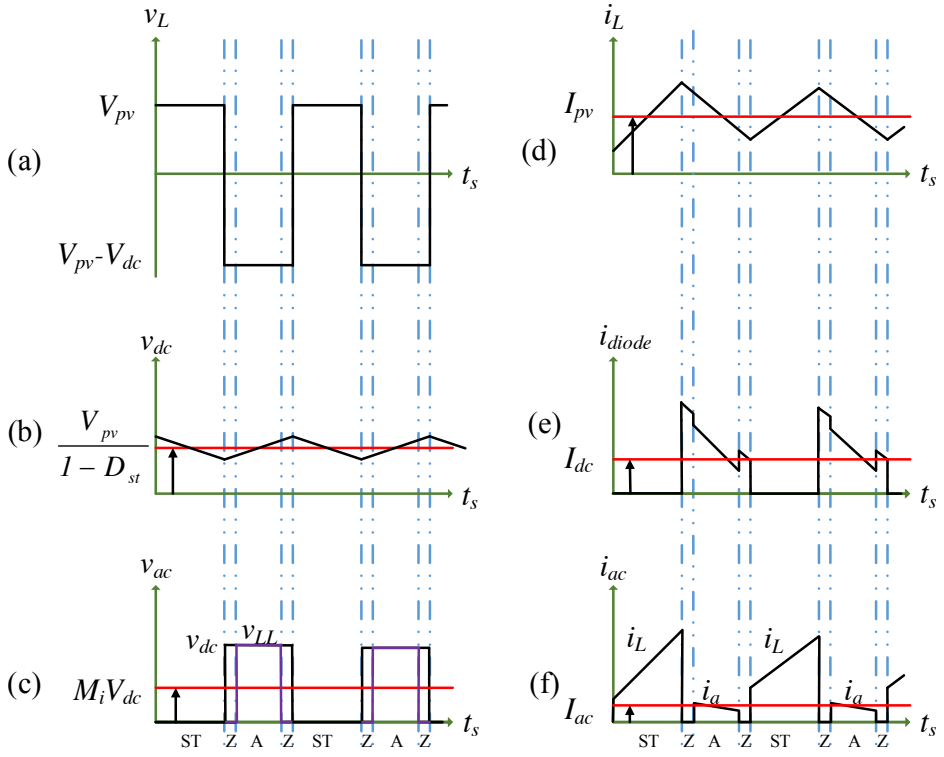

Figure 4.4. Behavior of the HBC's components during operational periods

Some assumptions are considered to better illustrate the steady state operation of the three-phase HBC. First, the system is assumed to be lossless where the damping elements equal zero. Second, the voltage drop on the switching diode is very small which can be ignored. Next, the

operational mode of the three-phase HBC is operated at inverter procedure where the power flows from the PV into the grid. Finally, the diode current is continuous during the active phase which three-phase HBC is generally operated in continuous conduction mode. So, the large and small signal analysis of three-phase HBC is similar to analyzing the dynamic equations of the boost converter with considering the impact of A and Z periods [99]. The steady state relation between the input source and output dc and ac sinks are given as follows:

$$V_{\rm dc} = \frac{V_{\rm pv}}{1 - D_{st}}, \quad \hat{V}_{\rm ac} = M_i \frac{V_{\rm dc}}{2} \tag{4.1}$$

$$V_{LL} = M_i \frac{\sqrt{3}}{\sqrt{2}} \frac{V_{\rm dc}}{2} = 0.612 \frac{M_i}{1 - D_{st}} V_{\rm pv} \tag{4.2}$$

where M_i and D_{st} are the ac voltage per-phase modulation index and duty cycle of the shoot-through period,respectively; $V_{\rm dc}$, $\hat{V_{\rm ac}}$, and V_{LL} are the peak dc voltage, peak per-phase ac voltage, and the rms value of the line-to-line output ac voltage, respectively. It can be concluded from (4.2) that the dc output depends on only D_{st} while ac output depends on both D_{st} and M_i. In order to achieve continuous control of PWM, the controlling signals have to achieve the following condition:

$$M_i + D_{st} < 1 \tag{4.3}$$

4.2.4 Modified PWM

It is mentioned in Section 4.2 that the three-phase HBC is operated at three main intervals which are integrated between boost converter and VSC's phases. Conventional sinusoidal PWM and dc PWM are not appropriate to operate the switching states of three-phase HBC. Instead of separately controlling the dc and ac outputs using the switches of three-phase HBC, a modified PWM is applied to control two outputs at the same time as shown in Fig. 4.5. It is recommended to insert the shoot-through phase within the zero mode where the output ac power equals zero in this phase [100]. During the shoot-through period, one leg of the two switchings, e.g., S_1 and S_4 are both on. This leads to PV side current flowing into S_1, S_4 only. During the shoot-through period, the inductor L gets charged. At the zero mode, all upper-level switches S_1, S_3 and S_5 are

on while the lower-level switches S_4, S_6 and S_2 are off. At this mode, the PV side current all flows to the dc side battery systems while the current to the ac system is zero. Finally, during the active mode, current will flow into the ac system.

The behavior of the open-loop control scheme for switching states of the HBC is shown in Fig. 4.5 when the reference for the phase voltages are related as $V_a > V_b > V_c$. The shoot-through operation occurs when the positive signal V_{st} is lower than carrier signal (phase C is shoot through with S_5 and S_2) and when the negative signal V_{st} is greater than the carrier signal (phase A is shoot-through with S_1 and S_4 on). Shoot through happens at the phases with the highest voltage or lowest voltage. In Fig. 4.5, phase A and Phase C are the phases with shoot-through periods. It is recommended to mention that shoot-through is forbidden in conventional VSC.

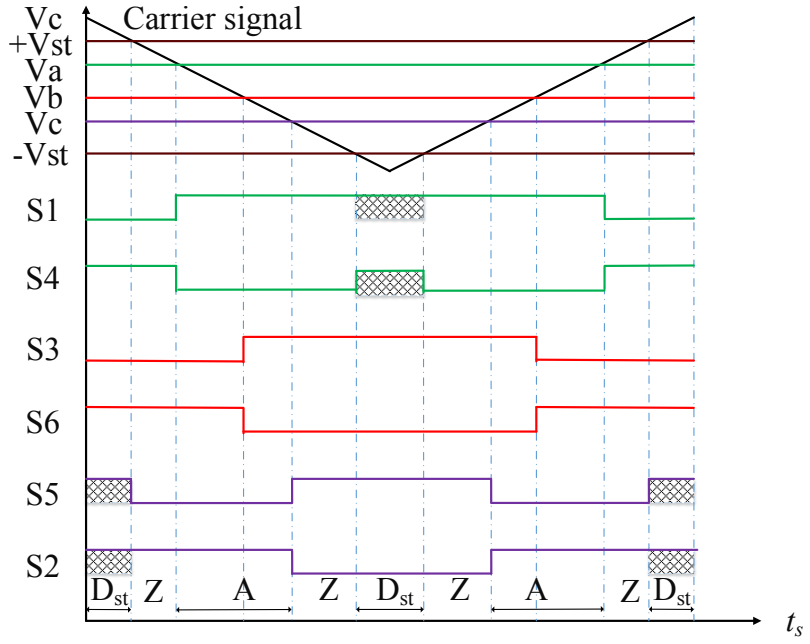

Figure 4.5. Modified PWM for the three-phase-HBC

Modified PWM regulates the switching states by controlling five signals which are three-phase ac signals V_a, V_b, V_c, and dc signals V_{st} ($V_{st} = 1 - D_{st}$), and $-V_{st}$. The ac controlling signals V_a, V_b, and V_c are controlled by modulation index M_i as well as phase angles while the dc signals $+V_{st}$, and $-V_{st}$ are regulated by duty ratio D_{st}. The advantage of using modified PWM is that both dc and ac outputs can be adjusted.

4.2.5 Modeling of PV Array

Modeling PV cell can be obtained as a photo-generated current source in parallel with two diodes and a shunt resistor, R_{sh}, as well as in series with a series resistor, R_s as shown in Fig. 4.6. Two diode model of PV has more accurate performance than the single-diode model because it represents diffusion and recombination characteristics of the charge carriers in each cell [96].

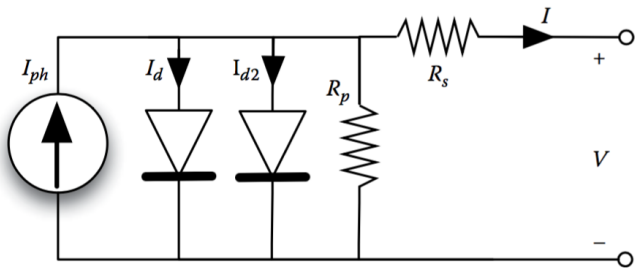

Figure 4.6. Two diode model of PV

The following equations provide output current of a single PV's cell:

$$I_{pv} = I_{ph} - I_{sat1}[e^{\frac{V_{pv}+I_{pv}R_s}{\eta_1 V_T}} - 1] - I_{sat2}[e^{\frac{V_{pv}+I_{pv}R_s}{\eta_2 V_T}} - 1] - \frac{V_{pv}+I_{pv}R_s}{R_p} \tag{4.4}$$

$$I_{ph} = I_{ph,STC}\frac{G}{G_{STC}}[1+\alpha_I(T-T_{STC})] \tag{4.5}$$

$$V_T = \frac{kT}{q} \tag{4.6}$$

$$I_{sat1} = C_1\frac{T}{T_{STC}}^{\frac{3}{\eta_1}} e^{\frac{-Egap}{\eta_1 kT}} \tag{4.7}$$

$$I_{sat2} = C_2\frac{T}{T_{STC}}^{\frac{5}{\eta_2}} e^{\frac{-Egap}{\eta_2 kT}} \tag{4.8}$$

where I_{ph} is the photo-induced current generated by the solar irradiation;I_{sat} is the reverse saturation current; V_T is the thermal voltage of the PV module; T is cell temperature on Kelvin; α_I and α_V are temperature coefficients of the current and voltage, respectively; k,q and η are Boltzmann constant, electron charge and diode ideality factor; E_{gap} and $C_{1,2}$ are the band gap of the semiconductor material and temperature coefficient; R_s and R_p are the equivalent internal and contact resistances, respectively.

4.3 Control of PV Charging Station

This section provides a detailed explanation of the framework and controller of the HBC-based PV charging station. From the steady-state relationship in (4.2), three-phase HBC utilizes D_{st} to boost the PV voltage while the modulation index M_i regulates the ac voltage V_t's magnitude. In addition, the angle of the three-phase ac voltage V_t can be adjusted to achieve active power and reactive power regulation. When the ac voltage is balanced and the ac system is symmetrical, the total three-phase instantaneous power is constant at steady-state. Thus, average power of the ac side equals to the net power at the dc side ($P_{\text{ac}} = P_{\text{pv}} - P_{\text{dc}}$).

Three main control blocks are used to control the three-phase HBC: MPPT, phase-locked loop (PLL) and vector control as shown in Fig. 4.7. Each block will be described in a subsection. The charging algorithm of off-board dc/dc converter will also be addressed in this section.

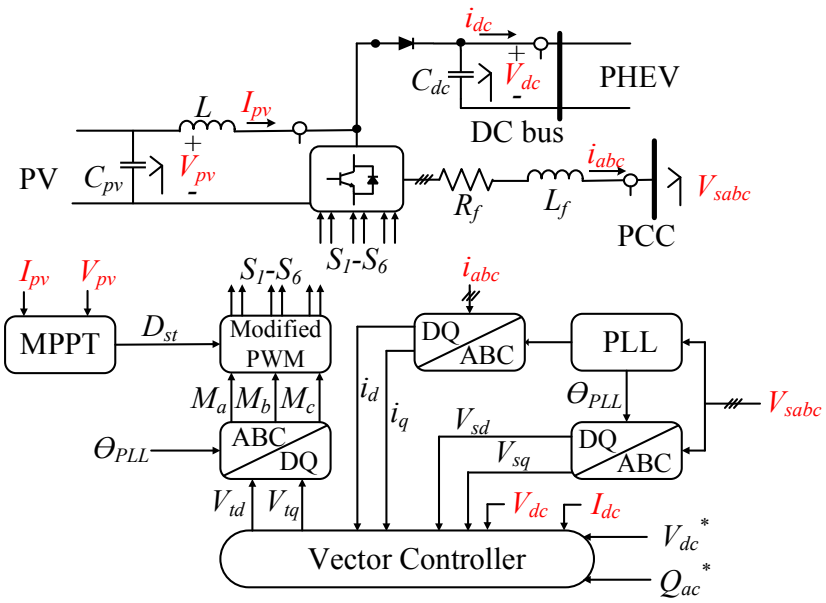

Figure 4.7. Control blocks of the HBC-based PV charging station.

4.3.1 Maximum Power Point Tracking (MPPT)

Maximum power point tracking (MPPT) algorithm is important to guarantee maximum power extraction from PV arrays. Various types of MPPT algorithms have been recently applied to control of MPP of PV modules. Hill climbing (HC), perturb and observe (PO), and incremental

conductance (IC) are the most attractive algorithms. MPPT techniques with simple structures and fast dynamic performances are demanded. IC among other MPPT methods has the benefits of fast dynamic performance [2, 101].

IC method computes the sensitive of power variation against the PV voltage. The optimal point is achieved when $\frac{dP_{\text{pv}}}{dV_{\text{pv}}} = 0$. Fig. 4.8 presents current/voltage and power/voltage relationships for a PV model based on Sunpower SPR-E20-327 which includes 60 parallel strings and 5 series modules in each string to generate maximum power of 100 KW. In the power/voltage plots, the maximum power points (MPPs) are located at the top of each plot when the gradient is zero. The slope is positive on the left-hand side of an MPP and negative on the right-hand side as shown in Fig. 4.8.

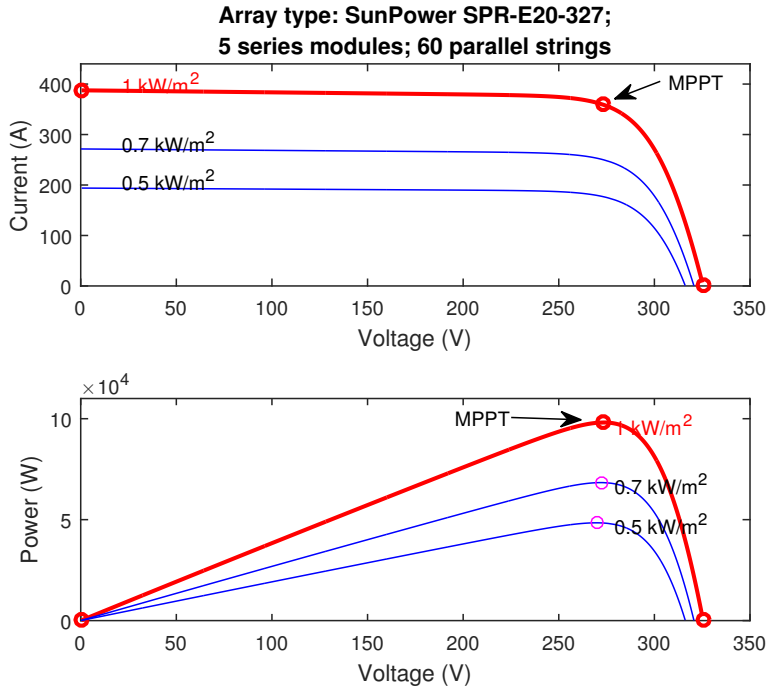

Figure 4.8. IV-curve for Sunpower SPR-E20-327

The operation of IC algorithm for MPPT is defined as:

$$\frac{dP_{\text{pv}}}{dV_{\text{pv}}} = I_{\text{pv}} + V_{\text{pv}} \frac{dI_{\text{pv}}}{dV_{\text{pv}}} \begin{cases} = 0, \text{MPP} \\ > 0, \text{left slope} \\ < 0, \text{right slope} \end{cases} \tag{4.9}$$

Instead of using $\frac{dP_{\rm pv}}{dV_{\rm pv}}$ as an indicator, the incremental conductance (IC) method relies on $\frac{dI_{\rm pv}}{dV_{\rm pv}}$. The definition of IC method can be adjusted for better dynamic performance of the MPPT. Based on the above relationship, we can also find that the following relationship:

$$\begin{cases} \frac{\Delta I_{\rm pv}}{\Delta V_{\rm pv}} + \frac{I_{\rm pv}}{V_{\rm pv}} = 0, \text{optimal point} & (a) \\ \frac{\Delta I_{\rm pv}}{\Delta V_{\rm pv}} + \frac{I_{\rm pv}}{V_{\rm pv}} > 0, \text{left slope} & (b) \\ \frac{\Delta I_{\rm pv}}{\Delta V_{\rm pv}} + \frac{I_{\rm pv}}{V_{\rm pv}} < 0, \text{right slope} & (c) \end{cases} \tag{4.10}$$

The IC method requires to have the voltage deviation. When voltage deviation is very small, the computed incremental conductance may not be accurate. It is observed that the error of comparing the instantaneous conductance ($\frac{I_{\rm pv}}{V_{\rm pv}}$) to the incremental conductance ($\frac{\Delta I_{\rm pv}}{\Delta V_{\rm pv}}$) does not achieve zero at low irradiation [101].

To avoid using $\Delta V_{\rm pv}$ in the denominator, [102] proposed a modified IC method. The modified IC method is derived based on (4.9):

$$\begin{aligned} \text{sign}(dV_{\rm pv})dP_{\rm pv} &= \text{sign}(dV_{\rm pv})(I_{\rm pv}dV_{\rm pv} + V_{\rm pv}dI_{\rm pv}) \\ &\begin{cases} = 0, \text{MPP} \\ > 0, \text{left slope} \\ < 0, \text{right slope} \end{cases} \end{aligned} \tag{4.11}$$

The control block of the modified IC based MPPT is shown in Fig. 4.9. The instantaneous conductance will be added to the incremental conductance to generate an error signal. A proportional-integral (PI) controller forces the error signal to approach zero. The output of the MPPT block is subtracted from the reference duty cycle D^* to generate D_{st}, which regulates the output dc voltage.

The subtraction is based on the relationship between $V_{\rm pv}$ and $V_{\rm dc}$ in (1a): $V_{\rm pv} = V_{\rm dc}(1 - D_{st})$. When the PV operation point is located as the left slope of the power/voltage curve, we would like to have $V_{\rm pv}$ be increased, or D_{st} be reduced if the input signal is greater than zero. Therefore, the subtraction is employed in the control block.

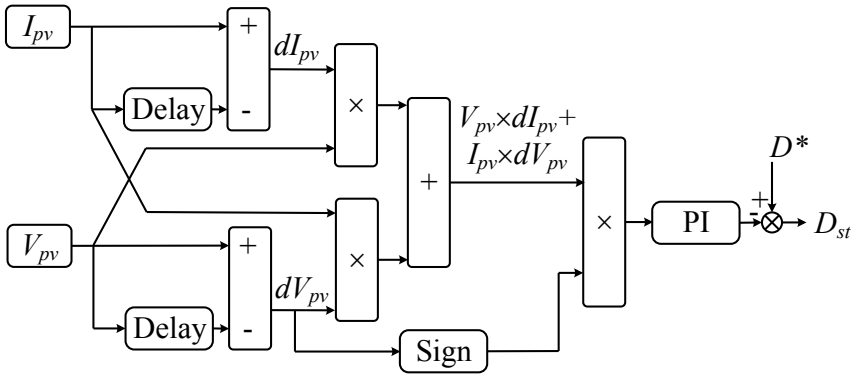

Figure 4.9. MPPT technique for PV using modified IC-MPPT method

4.3.2 Synchronous Rotating Reference Frame PLL (SRF-PLL)

The three-phase HBC is operated at grid-tied mode since the PV charging station needs ac grid as a backup supply. Integration of the three-phase HBC has to satisfy IEEE-1547 standard which requires synchrony of the phase and angular frequency of the three-phase HBC with the main grid [52,103]. The controlling and designing of Synchronous rotating frame-based phase-locked-loop (SRF-PLL) is presented in chapter 2.

4.3.3 Vector Control for PV Charging Station

Vector control technique is used for VSC. The inner loop controls the ac current while the outer loop controls the dc voltage and reactive power. The dynamic equations of the three-phase HBC are similar to those of the conventional VSC examined in [46, 104]. The main difference of HBC is the consideration of D_{st}. The inner current control loop is designed to respond much faster than the outer voltage controller for fast response and disturbance rejection. It is suggested to achieve fast transient response that the response of the inner loop to be in milliseconds, while the outer loop is 10 times slower than the inner loop. The open-loop of the inner current loop includes the transfer function of the plant and the delay of the modified PWM as well as the PI compensator.

$$G_{i,ol}(s) = \left(K_{pi} + \frac{K_{ii}}{s}\right) \frac{1}{L_f s + R_f} \frac{1}{T_{\text{PWM}} s + 1} \tag{4.12}$$

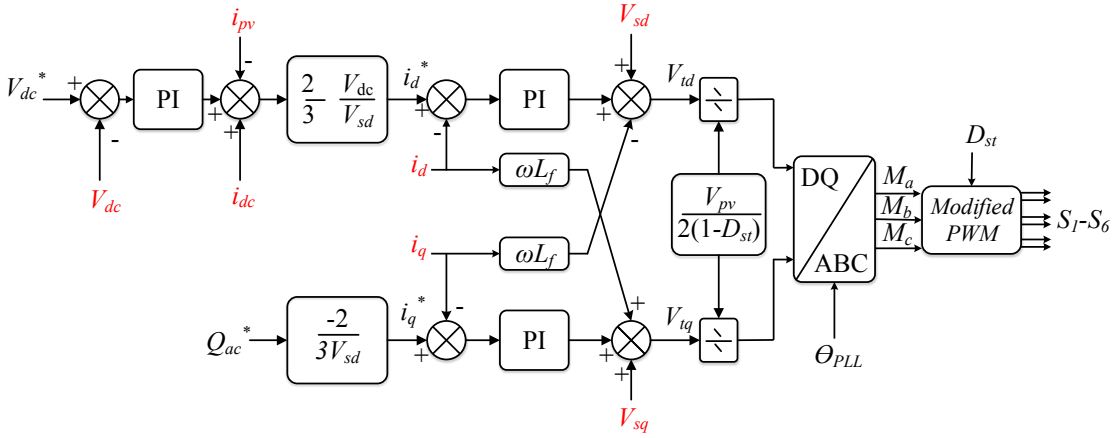

Figure 4.10. Vector control scheme of the three-phase HBC

where T_{PWM} is time delay of switching frequency of the modified PWM; K_{pi} and K_{pi} are the PI compensator's parameters for the inner current loop; L_f and R_f are the inductance and resistance filter components of the converter, respectively.

Tuning current compensator is achieved by using modulus optimum technique [104]. The concept of modulus optimum is defined as shifting the dominated poles that cause slow dynamic response and achieving unity gain for the closed-loop system. The PI controller's zero will cancel the pole dominated by the RL circuit dynamics. The open-loop transfer function becomes

$$G_{iol}(s) = \frac{1}{sT_{\mathrm{PWM}}(T_{\mathrm{PWM}}s + 1)} \tag{4.13}$$

by choosing the following parameters: $K_{pi} = \frac{L_f}{T_{\mathrm{PWM}}}$, $K_{ii} = \frac{R_f}{T_{\mathrm{PWM}}}$.

One of the advantage of the proposed HBC-based PV station is to generate a supported reactive power to the main grid. The controlling design of the reactive power loop is explained in details. The delivered reactive power of the three-phase HBC at PCC is calculated as:

$$Q_{pcc} = -\frac{3}{2}V_{sd}i_q \tag{4.14}$$

where V_{sd} is the projection of the ac voltage component on d axis of the stationary reference frame; i_q is the projection of the output current of HBC on q reference frame. The open-loop transfer

function of the reactive power controller is given as follow:

$$G_{ol}(s) = G_Q(s)G_{pi}(s)G_{sw}(s)G_i(s) = (\frac{3}{2}V_{sd})(\frac{k_{pQ}s + k_{iQ}}{s})(\frac{1}{T_{\rm PWM}s+1})(\frac{1}{L_f s + R_f}) \tag{4.15}$$

where k_{pQ} and k_{iQ} are the PI compensator's parameters. Using modulus optimum technique on Equ. (4.15), the open-loop and closed loop transfer functions of the reactive power are driven as:

$$G_{ol}(s) = \frac{1}{\tau_Q s(T_{\rm PWM}s+1)} \tag{4.16}$$

$$G_{cl}(s) = \frac{1}{T_{\rm PWM}\tau_Q s^2 + \tau_Q s + 1} \tag{4.17}$$

$$k_p = \frac{3}{2}\frac{V_{sd}L_f}{\tau_Q}; k_i = \frac{3}{2}\frac{V_{sd}R_f}{\tau_Q} \tag{4.18}$$

where τ_Q is the time constant of the resultant closed-loop system. Equ. (4.17) represents a general form of the second order system. The frequency of natural oscillation is obtained from Equ. (4.17) to be equal $\omega_n = \sqrt{(\frac{1}{T_{\rm PWM}\tau_Q})}$ while the damping factor equals $\zeta = \sqrt{(\frac{\tau_Q}{4T_{\rm PWM}})}$.

Assuming no switching power loss, the steady-state operation of the power balance is given as:

$$P_{\rm pv} = P_{\rm cap} + P_{\rm dc} + P_{\rm ac} \tag{4.19}$$

$$P_{\rm ac} = \frac{3}{2}V_{sd}i_d \tag{4.20}$$

where i_d and V_{sd} are the projections of the ac current and grid voltage space vectors on the d-axis.

The power relationship is further expressed as follows.

$$\begin{aligned} P_{\rm cap} = CV_{\rm dc}\frac{dV_{\rm dc}}{dt} &= P_{\rm pv} - P_{\rm ac} - P_{\rm dc} \\ &= V_{\rm dc}I_{\rm pv} - \frac{3}{2}V_{sd}i_d - V_{\rm dc}I_{\rm dc} \end{aligned}$$

Therefore, the dynamics of the capacitor voltage can be expressed as follows.

$$C\frac{dV_{\rm dc}}{dt} = \underbrace{I_{\rm pv} - \frac{3}{2}\frac{V_{sd}}{V_{\rm dc}}i_d - I_{\rm dc}}_{u_d} \tag{4.21}$$

A negative feedback controller will be designed to take in the dc voltage error $V_{\rm dc}^* - V_{\rm dc}$ and amplified by a PI controller. The output of the PI controller is u_d. From this signal, the reference signal i_d^* will be generated as:

$$i_d^* = \frac{2}{3}\frac{V_{\rm dc}}{V_{sd}}(u_d - I_{\rm pv} + I_{\rm dc}).$$

The open-loop transfer function of outer voltage is given as:

$$G_{v,ol}(s) = \left(K_{pv} + \frac{K_{iv}}{s}\right)\frac{1}{\tau_i s + 1}\frac{1}{Cs} \tag{4.22}$$

where τ_i is the time constant for the inner current closed loop. The open-loop transfer function for voltage controller includes two poles at origin.

Symmetrical optimum is a technique to deal with an open-loop system with double integrators [104]. The concept of symmetrical optimum is to operate the system at a low frequency to slow down the dynamic response which leads to an increased phase margin. The compensator parameters are given based on the symmetrical optimum method as follows.

$$T_{iv} = a^2\tau_i, \quad K_{\rm pv} = \frac{C}{K\sqrt{T_{iv}\tau_i}}, \quad K_{iv} = \frac{K_{\rm pv}}{T_{iv}} \tag{4.23}$$

where K equals $\frac{3V_{sd}}{2V_{\rm dc}}$ and a is the symmetrical frequency range between peak phase margin and low frequency operation area. It is important to select a high value of the symmetrical gain a to achieve high phase margin. The value of a falls between 2 and 4 [105].

The frequency respond of the open loop of inner current controller and outer voltage loop are designed by bode plot as shown in Figs. 4.11 and 4.12. The closed loop of the system is given in Fig. 4.13. It can be seen from Fig. 4.13 that the bandwidth of the inner loop is higher than the outer loop. So, the controller can response faster to the reference signal and provides stability.

4.3.4 Off-board Battery Charger

Most of the PHEV manufacturers are recently using lithium-ion batteries to operate their vehicles (e.g., Chevy Volt and Nissan Leaf). Since the PV charging station provides fast dc charging

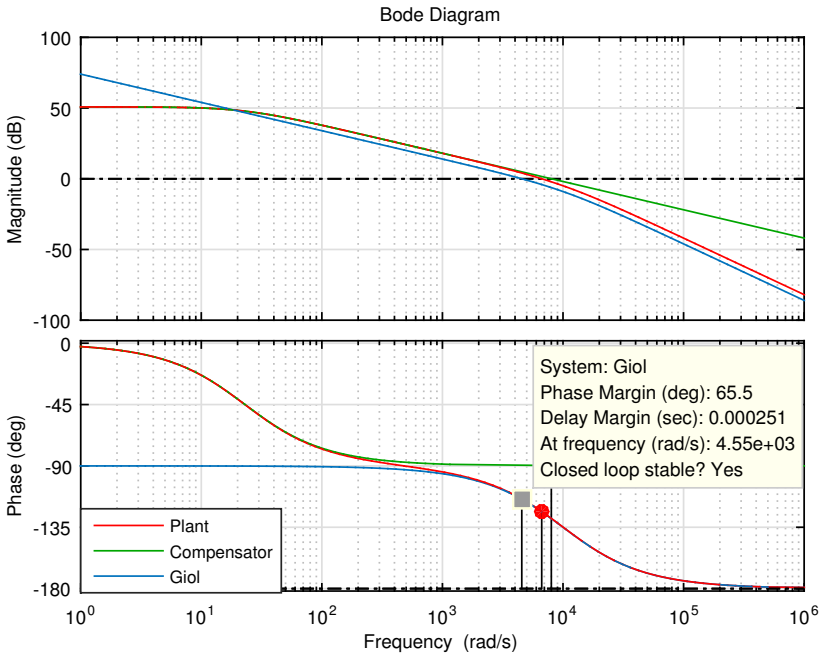

Figure 4.11. Bode plot for open loop current controller

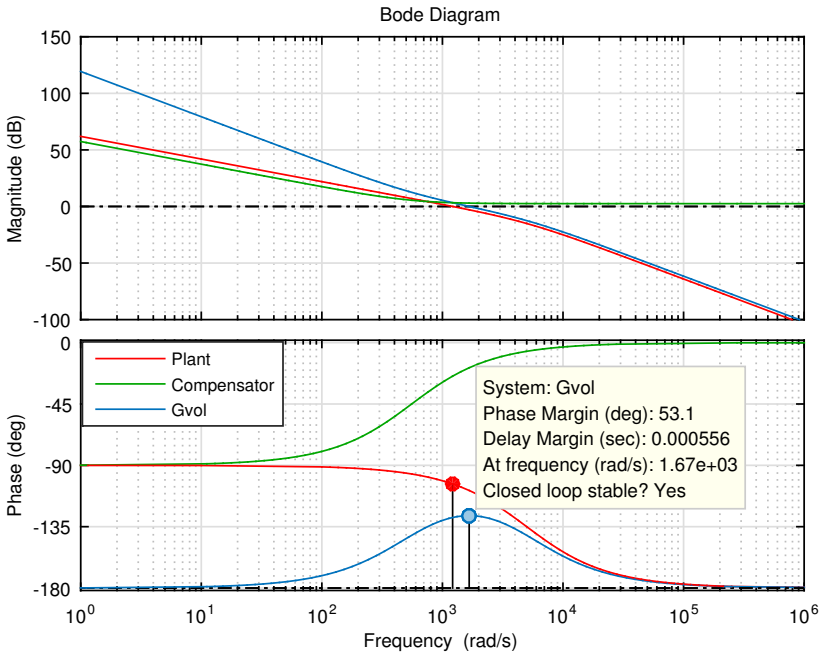

Figure 4.12. Bode plot for open loop voltage controller

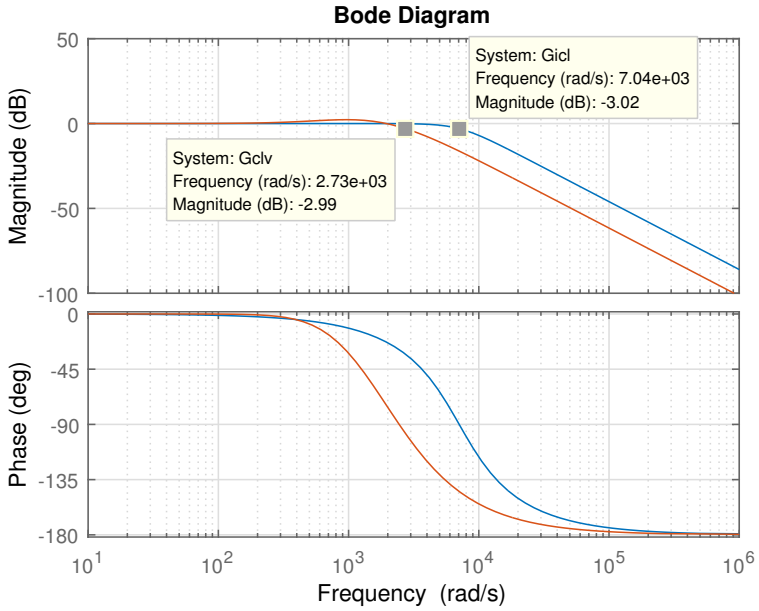

Figure 4.13. Bode plot for closed loop controller

procedure, it is important to investigate the model of lithium-ion batteries. An equivalent electrical battery cell model is shown in Fig. 4.15. The battery model is composed of capacitor $C_{Capacity}$ and a current-controlled current source that represents the battery's life. It also includes the Thevenin-based model of the transient and steady-state elements as well as a voltage-controlled open circuit voltage source. The dependent voltage source represents the amount of available energy in each battery's cell which is a function of the state of charge (SOC) of the battery. The modeling design of PV charging station load requires aggregate the charged batteries of PHEV. This paper presents an aggregated model of PHEV batteries that are connected in parallel for fast dc charging procedure. Fig. 4.15 demonstrates the equivalent circuit of connecting PHEV batteries to the PV charging station. The battery's cells are connected in series to increase the voltage of the battery while the parallel connection of the battery increases the total energy. So, each PHEV's battery consists of M branches and each branch consists of N cells. The detailed parameters of the commercial PHEV can be found in [106].

Since a battery storage system is one of the most critical and expensive elements of PHEV, charging control need to be carefully designed especially for fast charging process of PV station.

Fast charging technique may cause an excessive damage to the battery at the beginning of charging process or increase the cell temperature if the battery reaches full charge and high current charging is continued [107]. Standards such as the US NEVS and SAE J1772 [108, 109], mentioned that controlling of off-board dc/dc converter is important for fast charging procedure.

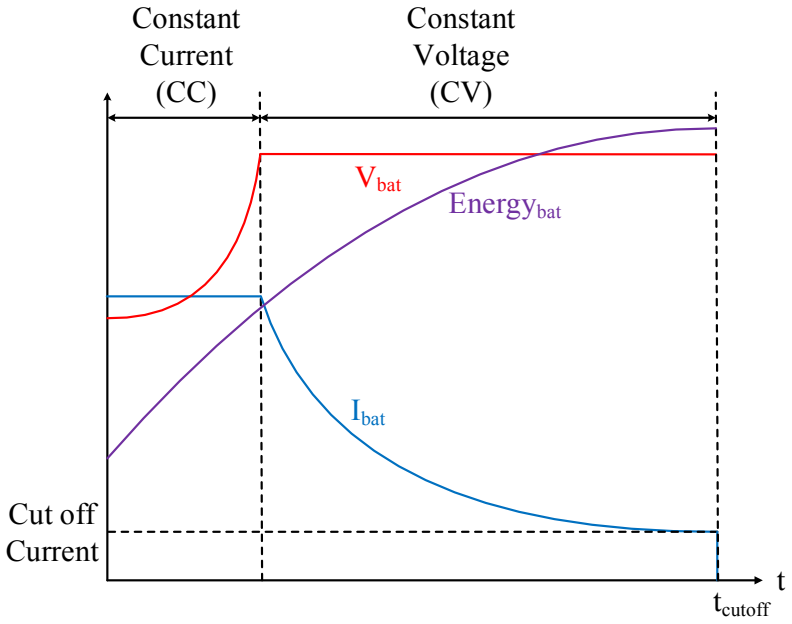

Figure 4.14. A simple diagram of CC-CV technique for PHEV's battery charging

In terms of charging schemes of a PHEV's battery, constant-current (CC) charging, constant-voltage (CV) charging, and taper-current (TC) charging are the three basic types of charging the batteries [29,110,111]. CC charging method performs a relatively uniform current charging without considering the battery state of charging (SOC) or temperature. The CC method mainly depends on low or high constant charging current which helps eliminate imbalances of cells and enhances life cycle of the battery. However, low charging current may not be acceptable to apply for dc fast charging of PV station while too high charging current could easily catalyze an excessive damage at the end of the charging procedure. Furthermore, CV procedure generally limits the voltage input to a specific level regardless of the SOC of the battery. Implementing CV method requires the knowledge of initial battery's voltage to avoid the high potential difference between the battery and charger which causes a high initial current. This requirement is difficult to apply in real

applications of PV station since each PHEV's has different battery's characteristic. The concept of TC charging method depends on decreasing the charging in proportion to the voltage rising of the battery. The advantage of this method is that it prevents the gasification and overheat issues the end of the fast charging process. However, the accuracy of implementing the charging procedure is low in real applications due to the diversity characteristics between each of the PHEV's batteries.

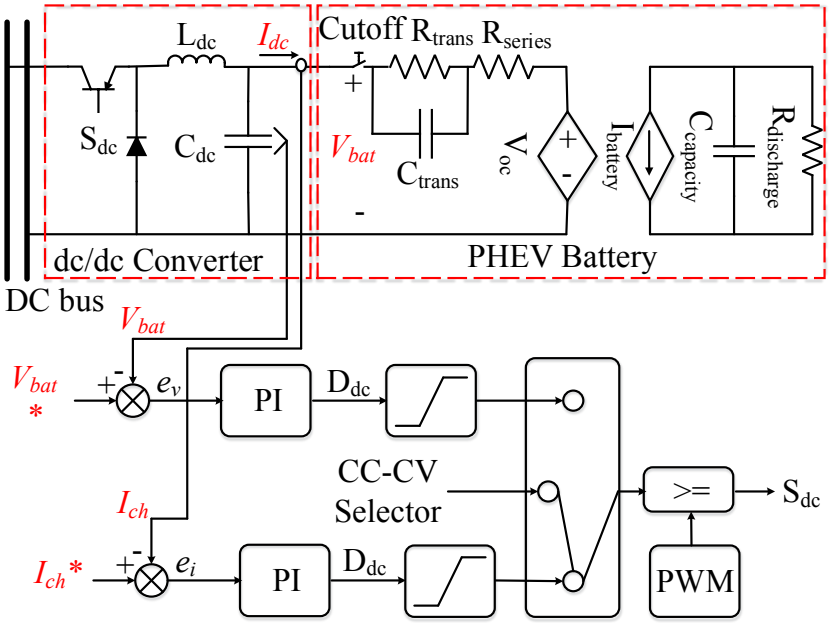

Figure 4.15. Off-board charging structure using CC-CV algorithm

Considering the features of the each aforesaid methods, this paper introduces the integration of constant-current and constant-voltage (CC-CV) methods to enhance the efficiency and reliability of the PV charging station. The procedure of implementing CC-CV on dc/dc converter is shown in Fig. 4.14 which mainly depends on controlling the charging voltage and current of battery at the same time. The charging process depends on first charging the battery with constant current to avoid the high initial current which is caused by a voltage difference between the battery and charger. When the battery's voltage reaches the rated battery's voltage, the controller switches to CV loop to avoid overcharge. Finally, when the battery's energy reaches the full charge region and the batteries current reaches the cutoff line, the controller disconnects the PHEV for protection. Implementing CC-CV method has several advantages such avoiding overheating issue and preventing overcharge.

When the charging procedure is operated at CC mode, the dc/dc converter charge the battery with constant current until the voltage reaches its preset value. Then, the control method is changed to CV mode for supplying a constant voltage. Finally, when the battery current reaches the cute off region, the dc/dc converter discount the PHEV's battery to avoid overcharge. Fig. 4.15 shows two controlling loops are used to regulate the measured components of the battery and the configuration of detailed PHEV battery and off-board dc/dc buck converter. The upper CV loop is used for measuring V_{bat} to avoid overcharging issue while the lower CC loop is applied for I_{ch} to avoid overheating problem. The goal of the selector is to choose the operational mode of the charger as well as discount the battery when it is the full charge.

4.4 Power Management and Operation Modes

Generating a sufficient power to charge PHEV is controlled based on the operation level of DC link voltage and the loading condition. The system is consist of a PV array as a main generating source, three-phase ac grid as a supported source, and PHEV load. Measuring the DC bus voltage and the available power from PV determine the procedure and direction of power flow management using a proposed V_{dc} vector control. This technique reduces the complexity of the controller as well as provides efficiency and stability of the system. The vector control which is derived and explained in the previous section, play a major contribution in the selecting of operational mode of the system.

Fig.4.16 shows the three operational modes of the PV charging station using a bidirectional three-phase HBC. Since the three-phase HBC has the capability of being operated as converter or inverter, controlling only a dc voltage across the dc bus can simplify the complexity of controlling PV charging station. The operational modes of the system are categorized into three modes.

4.4.1 Mode I: PV Powers PHEV and the Utility

During a peak solar irradiation, the PV array extracts a maximum power which exceeds the load's demand. So, the bidirectional three-phase HBC delivers a required power to charge the PHEV at DC bus as well as inverting the remaining PV power to the grid. The V_{dc} vector controller

regulates the voltage at dc bus and supply the remaining PV power to the main grid. This mode provides more reliability to the system since it generates the required power for charging electric vehicles without the need for a power from the main grid.

4.4.2 Mode II: PV and the Utility Power the PHEV

In a case of low irradiance or high penetration of PHEV, the main grid participates in stabilizing the voltage at dc bus. The bidirectional three-phase HBC is operated as a converter by absorbing the grid's ac power to charge the PHEV. In order to simplify the controller and avoid disturbance during changing mode's transient, the regulating of dc voltage using a proposed controller can control the dc voltage at a specific value. As mentioned in the previous section, the outer loop absorbs a power from the PV or the grid to regulate the voltage at dc bus. So, when the voltage falls below the reference value, the controller absorbs a power from the main grid and send a signal to the modified PWM. All the PV power is transferred to dc bus and the remaining required power for charging a PHEV is generated from the utility. This mode can provide a stable charging as well as enhance battery's life of PHEV.

4.4.3 Mode III: The Utility only Powers the PHEV

The PV power does not generate any power during from midnight to sunset regarding absent of solar irradiation. So, the vector control is changing to PQ control instead to V_{dc} mode. The bidirectional three-phase HBC operates only at converter mode to rectify the ac power and recharge the PHEV. This mode always occurred at low ac load of the main gird.

4.5 Simulation Results

Case studies for a PV charging station using a three-phase HBC with the proposed control are conducted in MATLAB/SimPowerSystems environment. The system's parameters and PV data are given in Table 4.1. The data for the PV model is based on PV array type Sunpower SPR-E20-327. The V-I and P-V curves for different irradiance values are shown in Fig. 4.8. The battery parameters of Chevrolet Volt and Nissan Leaf are used to represent the batteries of

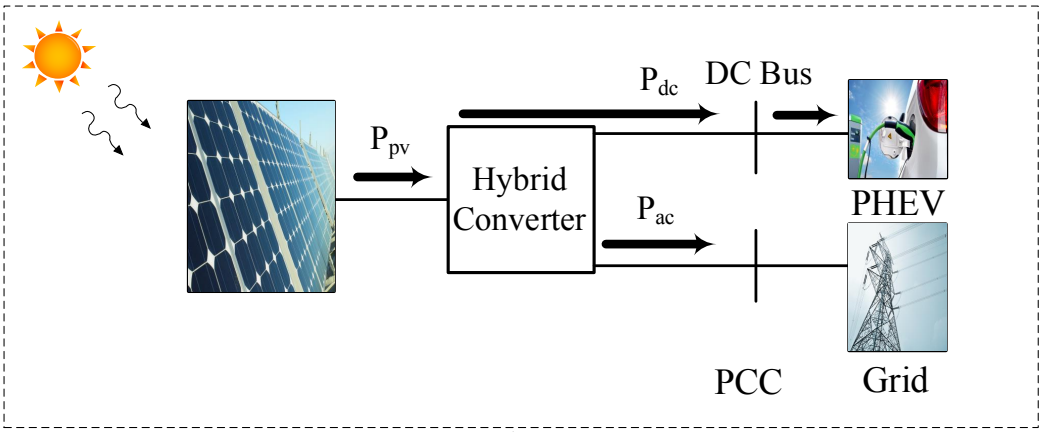

a) $P_{pv} > P_{PHEV}$

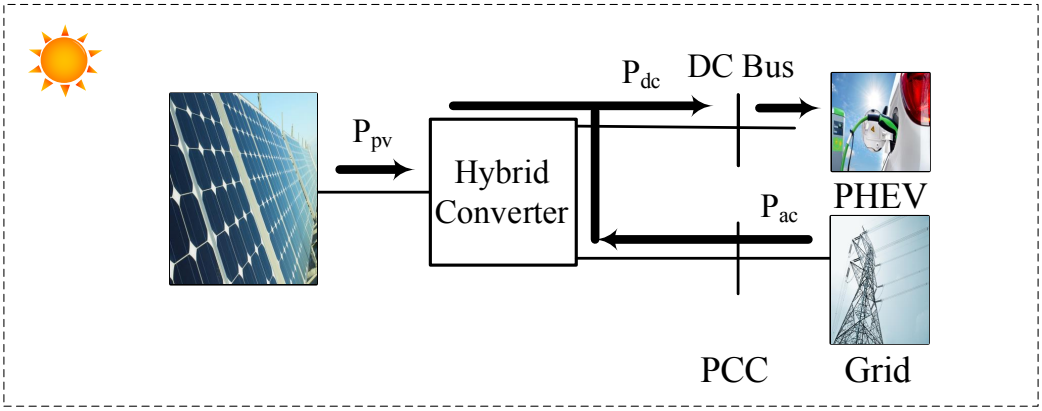

b) $P_{pv} < P_{PHEV}$

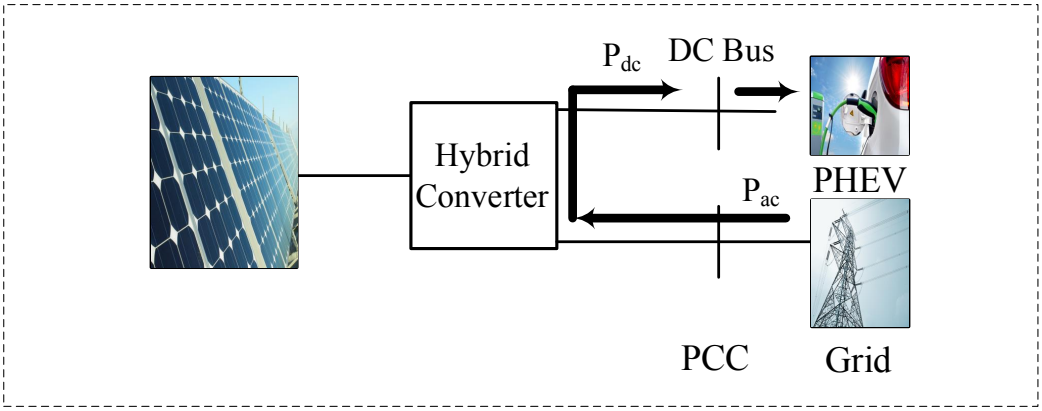

c) $P_{pv} = 0$

Figure 4.16. Operation modes of PV's charging station

PHEVs [25,112,113]. Four case studies are conducted to evaluate MPPT and vector control as well as to illustrate the operation modes and performance of the PV charging station.

Table 4.1. System parameters of a PV charging station

	Parameters		Parameters
PV	$V_{oc} = 65.1$ V $V_{mpp} = 54.7$ V $I_{sc} = 6.46$ A $I_{mpp} = 5.98$ A $R_{sh} = 298.531\ \Omega$ $R_s = 0.369\ \Omega$	AC Side	$V_{\text{grid}} = 20$ kV_{L-L} $\omega = 377$ rad/s $S = 100$ kVA $V_{ph} = 208\ V_{L-L}$ $R_f = 2\ \text{m}\Omega$ $L_f = 125\ \mu$H $Load = 20$ kW
DC Side	$V_{\text{dc}} = 350$ V $L = 5$ mH $C = 12000\ \mu$F $Load = 100$ kW $L_{dc} = 10$ mH $C_{dc} = 100\ \mu F$	AC/DC Control	$K_{pi} = 0.625\ \Omega$ $K_{ii} = 10\ \Omega$/s $K_{\text{pv}} = 0.24\ \Omega^{-1}$ $K_{iv} = 300\ \Omega^{-1}/s$ $K_{pvdc} = 0.001$ $K_{ivdc} = 25$ $K_{iidc} = 0.001$ $K_{iidc} = 3$
Chevy Volt	# of Cells: 200 $V_{\text{cell}} = 1.25$ V $Q_{\text{energy}} = 16$ kWh Type: Li-Ion	Nissan Leaf	# of cells: 160 $V_{\text{cell}} = 1.875$ V $Q_{\text{energy}} = 24$ kWh Type: Li-Ion

4.5.1 Case 1: Performance of Modified IC-MPPT

The goal of this case study is to validate the performance of the modified MPPT using the incremental conductance-PI algorithm. According to Fig. 4.8, the maximum PV power is 100 kW when the PV array generates 273.5 V at 1 kW/m^2 solar irradiance. Fig. 4.17 shows the performance of MPPT when the system is subject to solar irradiance variation. Different scenarios of solar irradiance variation have been applied such as step change and ramp change.

The dc voltage V_{dc} and the PV voltage V_{pv} are related based on the duty cycle ratio D_{st} that is generated from MPPT. The role of vector controller is to keep the dc voltage V_{dc} at its reference value $350V$ and supply reactive power Q^*_{ac} to the ac grid. The role of MPPT algorithm is to adjust the duty cycle ratio D_{st} and in turn adjust the PV output voltage V_{pv} so that the PVs are operating

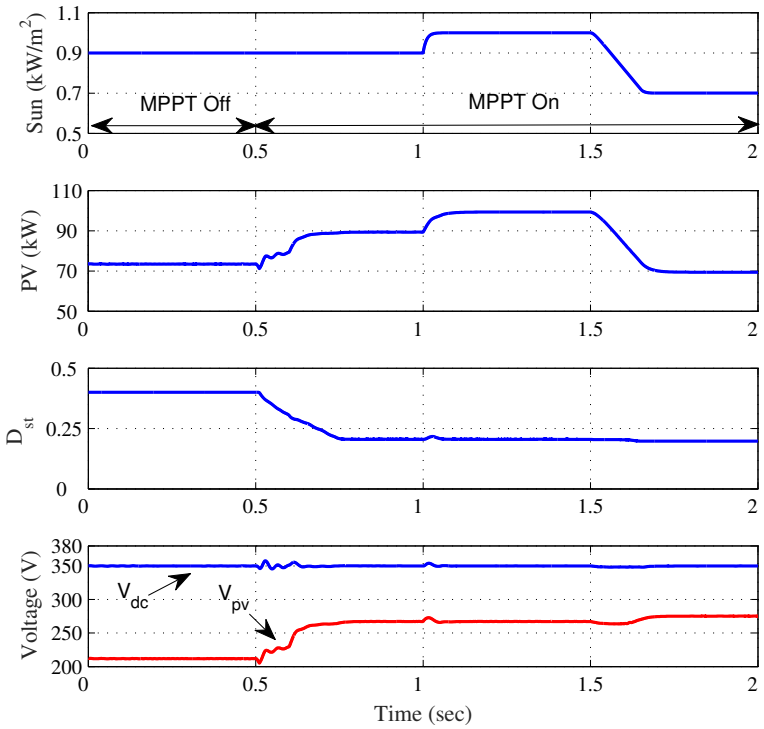

Figure 4.17. Performance of a modified IC-PI MPPT algorithm

at the maximum power extracting point. Fig. 4.17 provides the performance of MPPT based on four different intervals. From $0 - 0.5$ seconds, the sun irradiance is 0.9 kW/m^2 and the MPPT control is not activated. The output PV power supplies approximately 70 kW. At $t = 0.5$ seconds, MPPT is activated, the duty cycle ratio is decreased and the PV voltage is improved. This, in turn, improves the PV power output to be 90 kW.

Note that whether the MPPT is on or off, $V_{\rm dc}$ is kept at 350 V. At $t = 1$ second and $t = 1.5$ seconds, the sun irradiance increases and decreases. Due to the MPPT control, the optimal PV output voltage is kept at the optimal level. Further, the PV output power tracks the maximum point at each irradiance level. Fig. 4.17 validates the good tracking performance of MPPT when different solar irradiations are applied to the PV. The simulation results also show that the vector controller can regulate the dc voltage at 350 V and reject disturbances. This case study verifies that the proposed MPPT algorithm can provide maximum performance during disturbances.

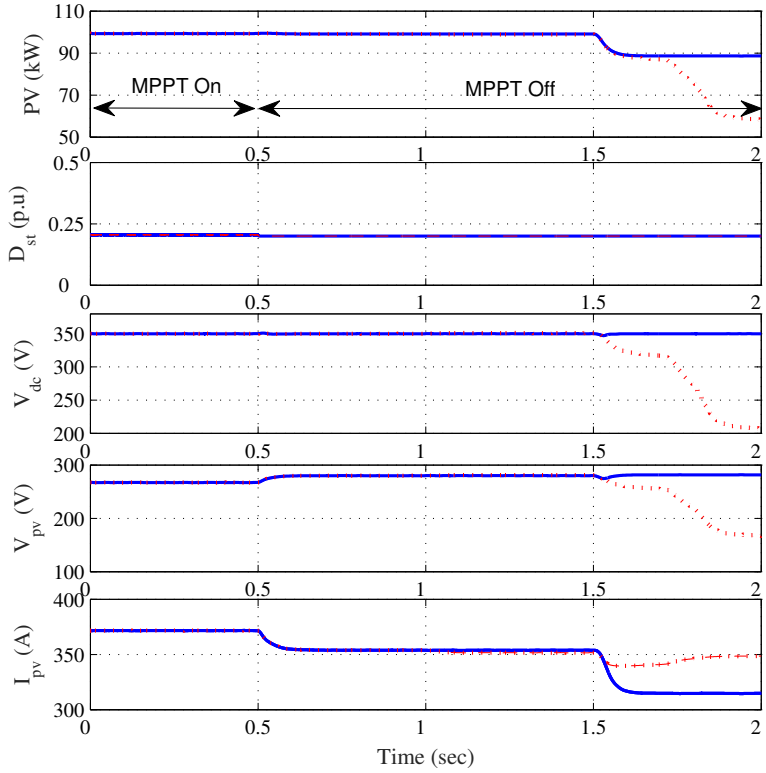

Figure 4.18. Performance of the dc voltage control in the vector control

4.5.2 Case 2: Performance of the DC Voltage Controller

The advantages of implementing the three-phase HBC on PV charging station is its capability to supply dc and ac power simultaneously. The main objective of a PV charging station is to supply continuous dc power to electric vehicles. Case 2 investigates the ability of the proposed controller to provide constant dc voltage with PV power variation and MPPT control status change.

Fig. 4.18 shows that when the dc voltage control is enabled, whether the MPPT control is on or off and whether the PV power has change or not, the dc voltage $V_{\rm dc}$ is kept at 350 V.As a comparison, when the dc voltage control is disabled and the MPPT control is off, the PV voltage will vary. Since the MPPT control is off, the duty cycle ratio D_{st} is kept constant and the dc voltage $V_{\rm dc}$ varies as well. This case study shows that the dc voltage control in the vector control provides an additional measure to keep the dc voltage constant.

4.5.3 Case 3: Reactive Power and Grid Fault

Another advantage of the three-phase HBC control is that it can support the ac grid by supplying or absorbing reactive power. The vector controller of PV charging station using three-phase HBC is well designed in previous sections to achieve decouple controlling for real and reactive power. This feature is applied in this case study to investigate the ability of the vector controller to quickly track the reactive power reference as well as maintain a constant dc voltage. The system is first in steady-state and the vector controller regulates the dc voltage and supply ac power at unity power factor as shown in Fig. 4.19. At $t = 0.5$ sec the reference reactive power absorbs 10 kVAr while at $t = 1$ sec it is changed to supply 10 kVAr to the main ac grid. The controller shows a good performance to track the reactive power reference as well as regulate the dc voltage at 350 V. Fig. 4.19 illustrates that the vector controller's M_d and M_q respond to the reactive power variation.

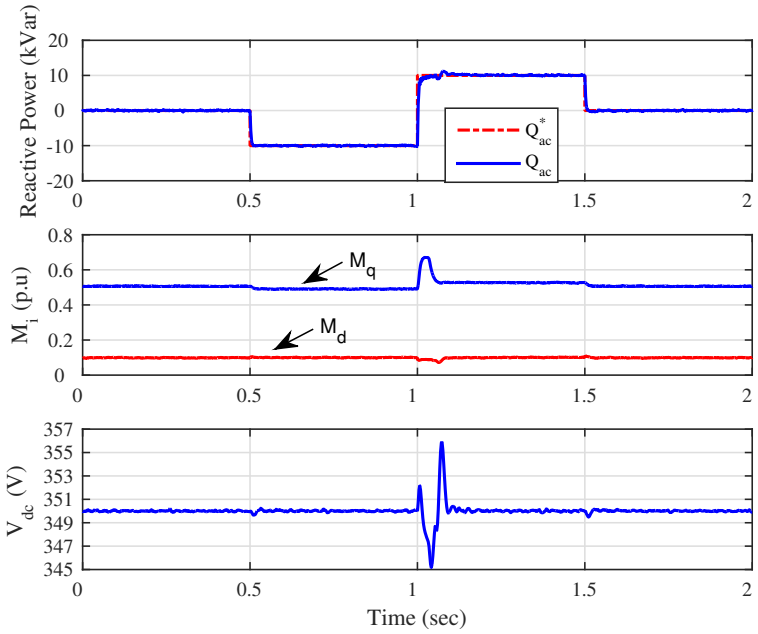

Figure 4.19. Performance of a proposed vector control using reactive power

Another important aspect of the three-phase HBC based PV charging station is its capability to charge PHEV's batteries during grid's fault. The controller is designed to provide a stable dc voltage even when grid fault is occurred. Generally, when the main grid voltage sages below 80% of the nominal voltage, the power quality standards recommend to disconnect the charged PHEV

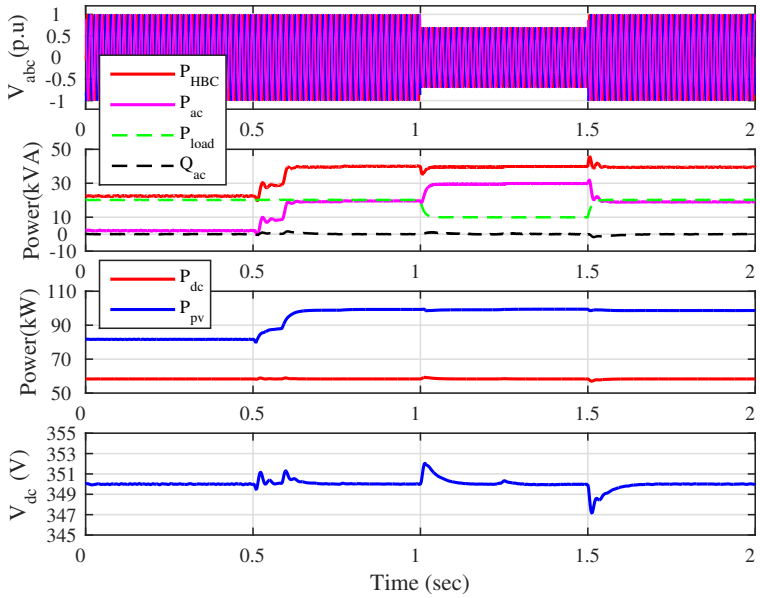

Figure 4.20. System performance under 50% grid's voltage drop

to protect the battery's life cycle [114]. The goal of designing the PV charging station's controller is to achieve constant charging procedure when a fault is occurred at the main grid. The method of achieve this goal is to isolate the PHEV's charger from the grid and provide sufficient power to charge the PHEV's batteries as well as maintain constant dc-link voltage. As a result, it is unnecessary to disconnect the PHEVs during grid fault.

The PV charging station is operated at steady state where the MPPT is not activated yet. The PV station generates dc power to charge the PHEV's batteries and satisfies the required the load power. When the MPPT controller is activate at $t = 0.5$ sec, the remaining power is supplied to the main ac gird as shown in Fig. 4.20. The main grid is facing a symmetrical 70% voltage sage at $t = 0.5$ sec and both the dc bus voltage and the ac load are expected to be affected. n nominal case, it is recommended to disconnect the ac load as well as the PHEV's batteries for protection and safety manners. However, the proposed controller can mitigate this issue by stabilize the dc-link voltage at its rated value as well as generate the required power to the local ac load. As also can be seen in Fig. 4.20, the MPPT algorithm is still working during the voltage sage. However, Fig. 4.20 shows that the power from the grid is increased to compensate the decreased power across the

ac load. Therefore, the power is balanced across the system and the PV charging station is isolated and can charge the PHEV's batteries during a grid's fault. When a partial grid fault is cleared at $t = 1$ sec, the controller can reject the transient dynamic and achieve stable dc bus voltage.

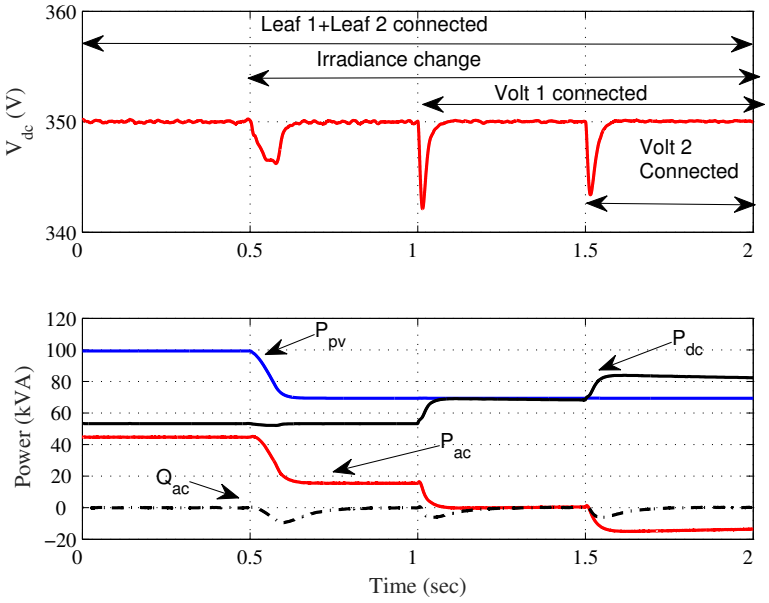

Figure 4.21. Power management of PV charging station

4.5.4 Case 4: Power Management of the PV Charging Station

An objective of the HBC is to charge PHEVs even when there is not enough PV power. The performance of the PV station is evaluated when different solar irradiations are applied. The goal of case study is to show continuous charging PHEVs even when the PV power is low. At day time the solar irradiance is assumed to be 1 kW/m^2 while at sunset the irradiance equals to 0.7 kW/m^2.

The dc load first consumes 50 kWh which represents charging of two Nissan Leaf vehicles. The two Nissan Leafs are charged before the PV power decreases as shown in Fig. 4.21. The remaining of PV power transfers to the main grid. At $t = 0.5$ seconds, the PV power reduces due to irradiance change. Two more vehicles are connected to the system consequently at $t = 1$ seconds and $t = 1.5$ sec. Fig. 4.21 shows that the PV array can provide power to the third car at $t = 1.5$ sec. The PV power is used to charge the batteries of PHEV with no dependency on the main grid.

At $t = 1.5$ seconds, the fourth electric car (Chevy Volt 2) is connected to the system. The a bidirectional feature of the three-phase HBC and the regulated dc voltage controller allow the dc load to absorb power from the main grid to charge the fourth vehicle as shown in Fig. 4.19. It is also noticed that the three-phase HBC can achieve power balance as well as maintain constant dc the voltage at 350 V. Fig. 4.21 also shows that the reactive power Q_{ac} is kept at 0. This shows that the three-phase HBC can achieve decoupled control of real and reactive power. Fig. 4.23 presents the duty cycle ratio and the modulation index in dq-axes. Fig. 4.24 presents the detailed control signals for modified PWM and the resulting switching sequences. This case study shows that the proposed control can provide a smooth transition when PHEVs are connected into the PV station.

4.5.5 Performance of Off-board dc/dc Converter

The CC-CV technique is applied to the proposed system to investigate the performance of the controller. The CC method is first selected for fast dc charging with 40 A. The battery is continuous charging unit it reaches 360 V which is the rated battery voltage of Chevy Volt vehicle [113]. When the battery voltage is equal to 360 V at $t = 2sec$, the CV control is selected while the battery's current is gradually decreased up to the cutoff region.

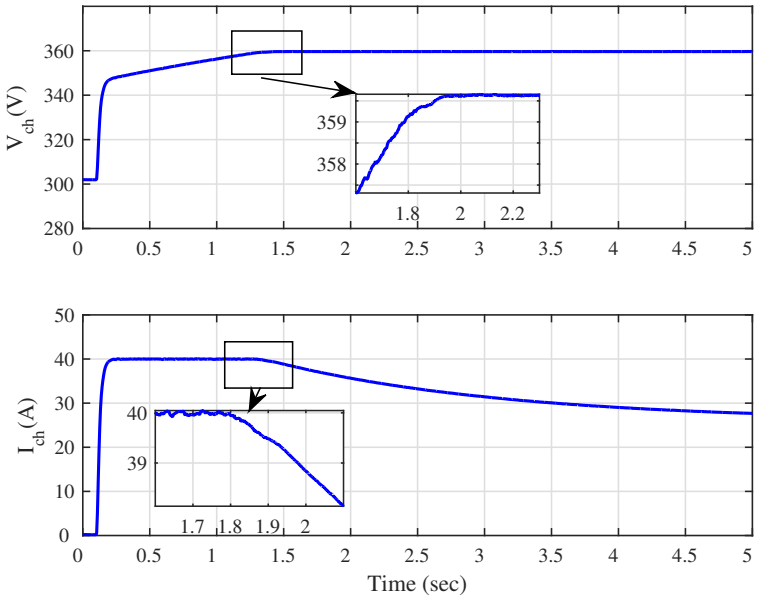

Figure 4.22. Performance of CC-CV algorithm

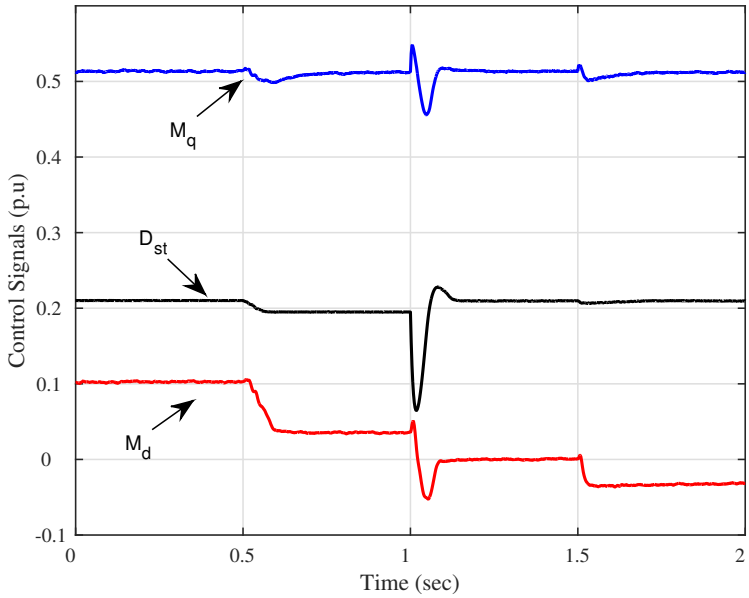

Figure 4.23. D_{st}, M_d and M_q for case 4

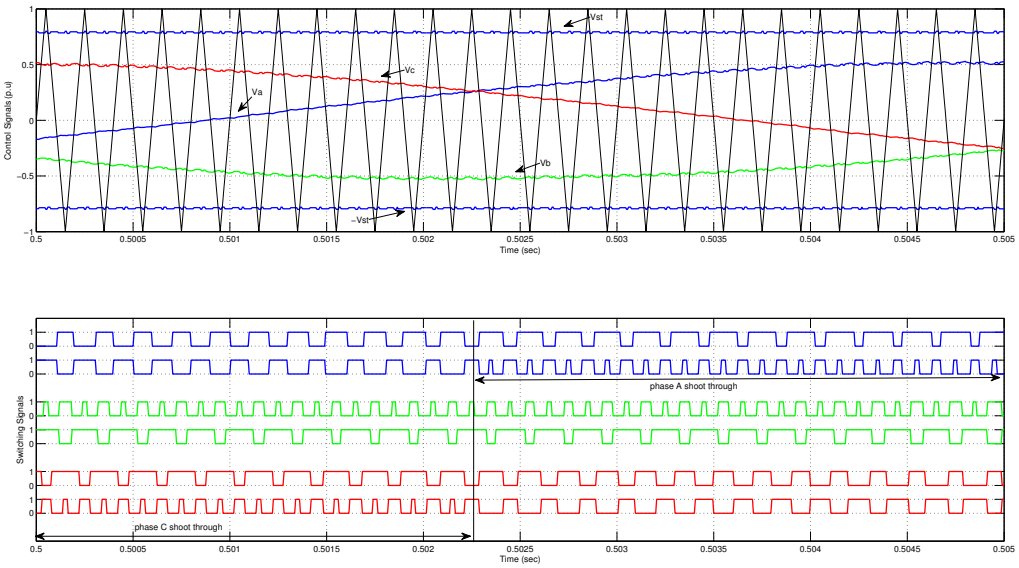

Figure 4.24. The modified PWM signals and the switching sequences

CHAPTER 5

COORDINATION OF SMART INVERTERS

5.1 Introduction

Microgrid is a distributed network that provides controllable power and supporting energy by interfacing distributed energy resources (DERs) with loads using power electronic mechanism. The microgrid can be operated at grid-connected or autonomous modes. The DER units are operated as grid-following (current controlled) or grid-forming (voltage-controlled) based on the connection mode of the microgrid [115, 116]. The microgrid's concept provides the opportunity to coordinate different types of DER units based on their rated power. However, controlling an autonomous microgrid shows challenging problems such as the difficulty to obtain equal power sharing and power balancing between generation and load [117].

Load-sharing technique for an autonomous microgrid is commonly applied using droop control method which mimics the behavior of a synchronous generator [55]. The concept of droop control depends on regulating the output voltage and frequency of DER unit based on the average load 's power. The advantages of droop control include high reliability and redundancy since the communication between DER units is not required [118]. However, implementing droop control requires an inherent trade-off between power sharing accuracy and voltage and frequency regulation. Regulating droop coefficients may also impact the stability of the system because of the slow dynamic response of droop control during the transient state. In [119], the authors confirm that droop coefficients influence on the stability of the system when the selected values of droop coefficients are closed the unstable region. The high value of droop coefficients leads to reduce the dynamic damping of the system which impacts the stability of the microgrid. Based on the aforementioned challenges, achieving equal power sharing using droop control is very difficult due

to the mismatched line impedance and different power ratings of the DER units [120, 121]. Thus, applying conventional droop controller to operate the autonomous microgrid may result in poor reactive power sharing, severe circuiting current, and power coupling issues [122, 123].

To realize accurate power sharing, several improved techniques on droop control have been proposed in the literature. In [124], the authors propose adjusting droop coefficients to improve power sharing accuracy between DER units. However, droop coefficients show poor dynamic response when load power disturbance is applied. The virtual output impedance is proposed in [125] to mitigate the impact of resistive line impedance and power coupling problems. Another proposed concept is addressed in [126] by decoupling the output current and power using pre-measured decoupling impedance. The derivation of virtual impedance and decoupling impedance are developed based on a simplified system which has considerable influence on the voltage quality due to frequent load changing. Another approach is proposed in [127] which mainly depends on an adaptive droop control. This technique can equally share the real load's power and enhance the voltage profile. However, the proposed method shows unequal reactive power sharing. The concept of master-slave control is addressed in [128] where only one DER unit (master) is responsible for generating voltage and frequency references while the other DER units (slaves) share the load power. The disadvantage of this method is that it is difficult to connect another master unit which reduces the redundancy of the system. A distributed secondary control is proposed in [129] by adding secondary control unit at each DER units. This method increases the complexity and cost of the system. It also requires central control unit for blackstart operation of an autonomous microgrid which reduces the reliability of the system. An enhanced central controller is proposed in [130] by injecting reactive and active power signals to reduce power sharing error. The central control monitors the behavior of active power and sends reactive power error signal to mitigate power coupling issue. However, this technique reduces the reliability of the system since it assumes no load disturbance during correction phase.

In the aforesaid manuscripts, the circulating current is not considered in analyzing the performance of the system at mismatched line impedance. Since droop control shows slow dynamic response during transit mode, circulating current participates in providing more oscillation to the

system. In this paper, an improved technique is proposed to realize reactive power sharing and mitigate the impact of circulating current when mismatched line impedance is presented. The novel technique is not only achieving equal power sharing, but it can improve the stability of the system by generating more dynamic damping during the transient state. The presented method consists of two-level controller which are primary and secondary levels. In this context, a droop algorithm is utilized at the primary control while an enhanced control microgrid unit (SCMU) is applied for secondary control. Sharing the information between the primary controller of DER units is realized via a communication bus. The advantage of the proposed method is that the knowledge of the line impedance value is not required which provides the opportunity to operate medium or low voltage microgrid where the line resistance is considered. The contribution of the paper lies in two aspects. The first contribution is identifying the key factor that causes poor power sharing by analyzing the mismatched line impedance issue. The derivation of circulating current is addressed based on the steady-state analysis. The second contribution is designing of primary and secondary controllers to operate an autonomous microgrid. The main purpose of designing the controller is to mitigate the impact of circulating current and enhance the transient dynamics response.

5.2 Analysis and Modeling of an Autonomous Microgrid

Controlling an autonomous microgrid is a difficult task since the role of each DER units is not only sharing the real and reactive powers but it also requires generating voltage and frequency. This section addresses a review of the primary droop control and the microgrid's configuration. The analysis of reactive power sharing and circulating current due to mismatched line impedance is presented in this section as well.

5.2.1 System Configuration

Fig. 5.1 shows a structure of the microgrid which is composed of DER units, local and global loads, network line impedance, and the main utility grid. The microgrid is connected to the main utility grid through the point of common coupling bus (PCC). DER units are connected to the local loads by dc/ac two-level three-phase converter (VSC), LC filter, and network line impedance.

When there is a fault or scheduled maintenance at the main grid, the static transfer switch (STS) is opened by a signal command from SCUM as presented in Fig. 5.1. The microgrid is then operated at autonomous mode while the SCUM changes the operational situation of DER units to grid-forming mode. This mode requires DER units to provide voltage and frequency to the local and global loads as well as sharing the total load power.

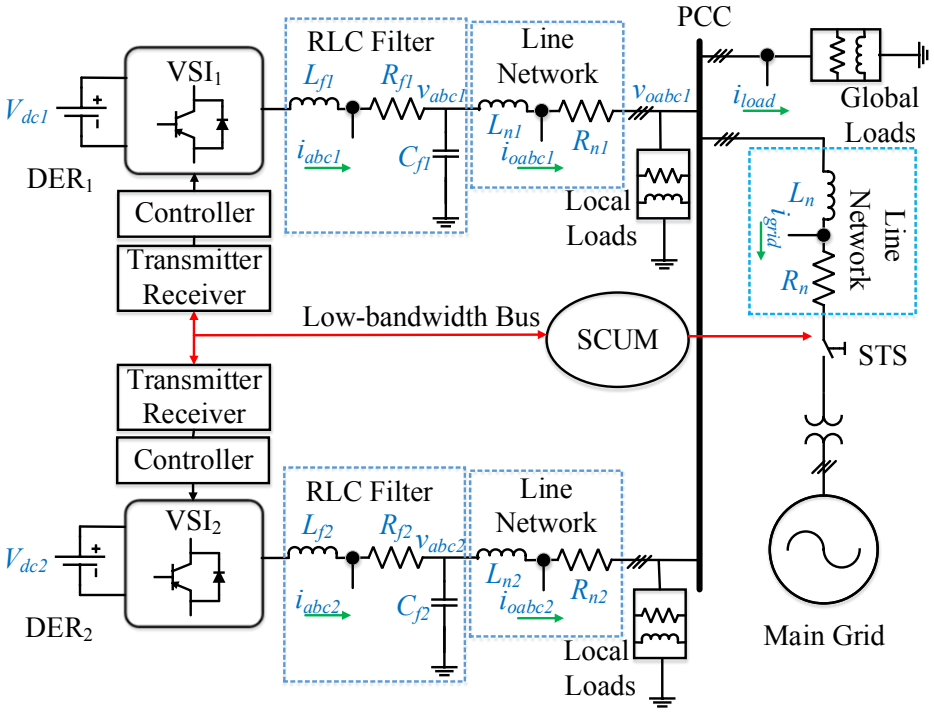

Figure 5.1. Single line-configuration of a microgrid

Controlling DER units is achieved by a hierarchal control which consists of primary and secondary central controls. The primary control includes droop control, cascaded inner voltage and current control loops as shown in Fig. 5.2 *b*. The main role of droop control is to regulating voltage and frequency of the microgrid based on the average output power. The cascaded inner voltage and frequency loops are designed to reject the high frequency disturbance as well as generate a terminal voltage reference for controlling switches of VSC. The role of secondary SCUM is to regulate the terminal output voltage of the primary droop control to achieve equal power sharing. Fig. 5.2 *b* shows a linearized model of the output voltage using hierarchal control. The figure shows that

SCUM injects a regulated voltage signal V_Q^s to achieve reactive power sharing and mitigate the circulating current which will be illustrated in section 5.3.

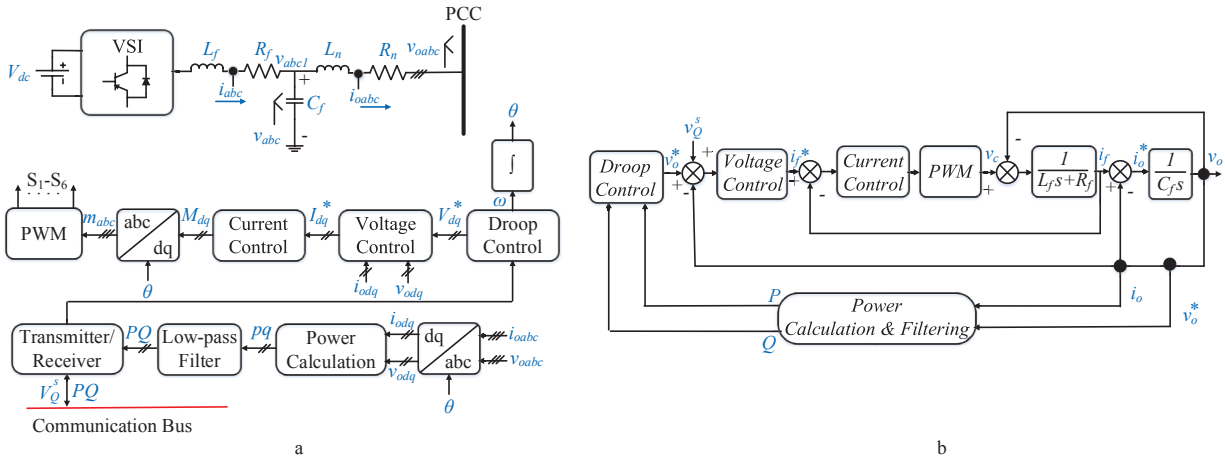

Figure 5.2. Block diagram of the autonomous microgrid

5.2.2 Control of Smart Inverter Using Primary Droop Control

This section demonstrates the concept of droop control as well as designs the vector controller for DER unit. Droop control is often implemented when at least two DER units are connected in parallel to form a microgrid. The primary control of each DER involves dual voltage and current control loops and droop algorithm as shown in Fig. 5.2 *b*. The output signal from the droop control is transferred to the cascaded inner loops to generate VSC's switching commands using PWM.

Since the microgrid contains multiple DER units, the system can be represented as multi-input and multi-output system. The DER units are operated as grid forming mode by generating voltage and frequency to the load. From Fig. 5.1, the power flow equation between DER and PCC is analyzed based on power flow equations as:

$$S_i = 3V_{oi}{I_{oi}}^* \tag{5.1}$$

$$P_i = \frac{3(R_{ni}V_{oi}^2 - R_{ni}V_{oi}V_{pcc}\cos\theta_i + X_{ni}V_{oi}V_{pcc}\sin\theta_i)}{R_{ni}^2 + X_{ni}^2} \tag{5.2}$$

$$Q_i = \frac{3(X_{ni}V_{oi}^2 - X_{ni}V_{oi}V_{pcc}\cos\theta_i - R_{ni}V_{oi}V_{pcc}\sin\theta_i)}{R_{ni}^2 + X_{ni}^2} \tag{5.3}$$

where S_i is the apparent power of the ith DER unit; P_i and Q_i are the output real and reactive powers, respectively; V_{oi} and I_{oi} are the output phase voltages and currents from ith DER unit; V_{pcc} is the voltage across PCC bus; R_{ni} and X_{ni} are the resistance and inductance line impedances; θ_i is the phase angle voltage difference between DER unit and PCC.

In order to simplify the concept of droop control, it is assumed that the line impedance (X/R) ratio is high; so the line resistance impedance can be ignored. Equations (5.2) and (5.3) are then modified based on the previous assumption where the output real power regulates the output frequency and the reactive power controls the output voltage magnitude as illustrated below:

$$P_i = \frac{3V_{oi}V_{pcc}}{X_{ni}}\sin(\theta_i) \tag{5.4}$$

$$Q_i = \frac{3(V_{oi}^2 - V_{oi}V_{pcc}\cos(\theta_i))}{X_{ni}} \tag{5.5}$$

Equations (5.4) and (5.5) show that the real power is proportional to the voltage phase angle while the reactive power is related to the voltage difference magnitude between DER units and PCC bus. Accordingly, the proportional droop gains are used to generate the voltage and frequency as:

$$\omega_i = \omega_i^* - k_{Pi}P_{oi} \tag{5.6}$$

$$V_{oi} = V_i^* - k_{Qi}Q_{oi} \tag{5.7}$$

where ω_i and ω_i^* are the output frequency and the rated frequency of the microgrid; V_{oi} and V_i^* are the output phase and the preset voltages; k_{Pi} and k_{Qi} are the droop coefficients for frequency and voltage controllers.

In conventional droop control, the constant droop coefficients k_{Pi} and k_{Qi} are selected based on the deviation of the output voltage and frequency over the maximum power [131]. The optimal value of droop coefficients are derived as:

$$k_{Pi} = \frac{\omega_{max} - \omega_{min}}{P_{oi_{max}}} \tag{5.8}$$

$$k_{Qi} = \frac{V_{max} - V_{min}}{Q_{oi_{max}}} \tag{5.9}$$

Vector control methodology is used to control the voltage and frequency of VSC. The concept of vector control depends on transferring symmetrical signals from three-phase time domain into two-phase rotating synchronous reference frame DQ [132]. Fig. 5.2 *a* is analyzed to model the primary droop control and inner voltage and current loops. The dynamic equations of the system are represented in synchronous rotating reference frame DQ as following:

$$\frac{di_{dqi}}{dt} = \frac{-R_{fi}}{L_{fi}} i_{dqi} \pm \omega_0 i_{qdi} + \frac{1}{L_{fi}}(v_{dqi} - v_{odqi}) \tag{5.10}$$

$$\frac{dv_{odqi}}{dt} = \pm\omega_0 v_{oqdi} + \frac{1}{C_{fi}}(i_{dqi} - i_{odqi}) \tag{5.11}$$

$$\frac{di_{odqi}}{dt} = \frac{-R_{ni}}{L_{oi}} i_{odqi} \pm \omega_0 i_{noqdi} + \frac{1}{L_{ni}}(v_{odqi} - v_{pccdq}) \tag{5.12}$$

where v_{dqi} and i_{dqi} are the filtered voltages and currents of inner loops of ith DER unit at DQ axes; v_{odqi} and i_{odqi} are the output voltages and currents of ith DER unit at DQ axes; v_{pccdq} are the voltages on PCC bus; R_{fi}, L_{fi}, and C_{fi} are the resistance, inductance, and capacitance components of LC filter; R_{ni} and L_{ni} are the resistance and inductance of the line impedance between DER unit and PCC bus.

Vector control is used to calculate the instantaneous real and reactive powers. As shown in Fig. 5.2 *a*, equations (5.4) and (5.5) are adjusted based on the output voltages and currants as:

$$p_i = \frac{3}{2}(v_{odi} i_{odi} + v_{oqi} i_{oqi}) \tag{5.13}$$

$$q_i = \frac{3}{2}(-v_{odi} i_{oqi} + v_{oqi} i_{odi}) \tag{5.14}$$

The droop coefficients have a proportional relationship with the load power. The measured instantaneous output powers are not sufficient to be applied for droop control. So, a low-pass filter is used to extract the average active and reactive output powers as shown below:

$$P_i = \frac{\omega_c}{s + \omega_c} p_i \tag{5.15}$$

$$Q_i = \frac{\omega_c}{s + \omega_c} q_i \tag{5.16}$$

where ω_c is the cutoff frequency of low-pass filter. The operation of filtering the instantaneous output power is given in power calculation block in Fig. 5.2 *a*. Since the output voltage contains two components on DQ axes, the magnitude of the output phase voltage is obtained as:

$$|V_{oi}| = \sqrt{v_{odi}^2 + v_{oqi}^2} \tag{5.17}$$

It is recommended to mention that the concept of vector control aims to align the output voltage on D axis which leads to $v_{oiq} = 0$. So, the output phase voltage will equal the voltage on D axis.

The derivation of droop coefficients depends on a balanced system which defines as total generated power from DER units should equal the total required power from the loads. Selecting optimal value of droop coefficient on equations (5.8) and (5.9) needs to consider an inherent trade-off between voltage and frequency regulation and power-sharing accuracy. Fig. 5.2 *a* shows that a low-pass filters are used to calculate the average value of the active and reactive powers. These main components of droop control need to be carefully designed to avoid stability issues [133]. Poor designing of droop coefficients k_{Pi}/k_{Qi} and cutoff frequency ω_c leads to reduce the dynamic damping response as well as generate unequal reactive power sharing and circulating current.

5.2.3 Reactive Power Sharing

This section analyzes the key factor that influences on the accuracy of reactive power sharing. As shown in Fig. 5.3, the power sharing between DER and the rest of the microgrid depends on the characteristics of the line impedance. The voltage drop across the line impedance is analyzed based on the output powers and voltages of each DER. Since the voltage angle frequency is a global variable, sharing active power can be achieved by properly selecting an accurate k_{Pi} coefficient of the $P - \omega$ droop control as given in equation (5.4). However, equally sharing the reactive power cannot be achieved by only tuning the k_{Qi} gain of the $(Q - V)$ droop control as seen in equations (5.5) and (5.9). The reason is that the reactive power depends on the voltage difference between the output voltage of DER unit and the voltage across PCC bus. So, the voltage drop on the line impedance influences on the reactive power sharing when there is a mismatched line impedance.

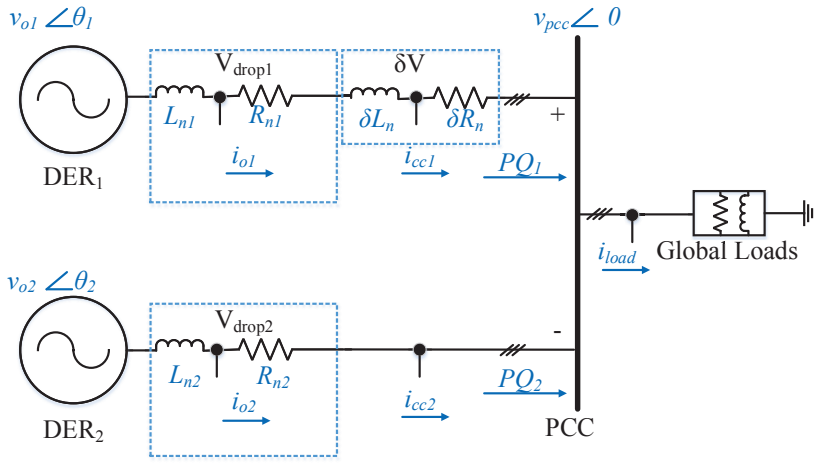

Figure 5.3. Simplified two-DER units microgrid with mismatched line impedance

Because of the complexity of the microgrid, it is assumed that the two DER units have identical power capacity and the local and global loads have no impact on the reactive power sharing. A simplified two DER units microgrid is shown in Fig. 5.3. Each DER unit is designed as an ideal voltage source. The output voltage of DER unit V_{oi} is a factor of wire and internal impedance, DC voltage, fundamental frequency and amplitude voltage component. The voltage drop on the line impedance is calculated as [55]:

$$V_{drop1} \approx \frac{X_{n1}Q_1 + R_{n1}P_1}{V_{o1}} \tag{5.18}$$

$$V_{drop2} \approx \frac{X_{n2}Q_2 + R_{n2}P_2}{V_{o2}} \tag{5.19}$$

where V_{drop1} and V_{drop2} are the drop voltages on the two different line impedances; X_{n1}, X_{n2}, R_{n1} and R_{n2} are different values of the inductance and resistance of the line impedances. Assuming the line impedances of the two DER units are given from Fig. 5.3 as:

$$X_{n1} = X_{n2} + \delta X \tag{5.20}$$

$$R_{n1} = R_{n2} + \delta R \tag{5.21}$$

where δX and δR are the mismatched line inductance and resistance between two DER units.

By adding the mismatched line impedance into equations (5.18) and (5.19), the output voltage is calculated based on Fig. 5.3 as:

$$V_{drop1} \approx \frac{(X_{n1} + \delta X)Q_1 + (R_{n1} + \delta R)P_1}{V_{o1}} \tag{5.22}$$

$$\approx \frac{X_{n1}Q_1 + R_{n1}P_1}{V_{o1}} + \frac{\delta XQ_1 + \delta RP_1}{V_{o1}} \tag{5.23}$$

$$V_{o1} = V_{pcc} + V_{drop1} + \delta V \tag{5.24}$$

$$V_{o2} = V_{pcc} + V_{drop2} \tag{5.25}$$

where δV is the voltage drop across the mismatched line impedance. It is noticed from equations (5.24) and (5.25) that the voltage across PCC (V_{pcc}) is facing two different values of the voltages from DER units because of the mismatched voltage drop (δV). These voltages will produce different values of reactive power across PCC bus [134, 135]. The output reactive power can be given by rewriting equation (5.7) as:

$$Q_i = \frac{V_{oi}^* - V_{oi}}{k_{Qi}} \tag{5.26}$$

Based on the aforesaid equations (5.20)-(5.26), three variables may impact on the reactive power sharing accuracy which are the mismatch line impedance, the output voltage difference magnitude between DER units, and the reactive droop coefficient. In real applications, achieving identical line impedance between DER units is a difficult task due to the distance difference and locations of DER units. Besides, increasing the droop gain k_{Qi} may reduce the reactive power based on equation (5.26). However, a large value of the droop coefficient causes large voltage variation from the nominal value [136]. This variation is restricted with a limitation of voltage amplitude deviation of each unit which has to be 10% of the nominal voltage according to IEEE standards [52]. In fact, the mismatched voltage drop could not be mitigated by only regulating the droop factor k_{Qi}. The reason is that the droop factor is proportional to the load power and any disturbance may lead to change the output voltage of DER unit. Another feasible solution is to adjust the output voltage difference magnitude between DER units which can achieve balanced voltage at PCC. Regulating

the voltage difference between the output DER voltage and the reference voltage may reduce the reactive power error as seen in equations (5.24) and (5.25).

The linearized model in Fig. 5.2 *b* shows that injected voltage V_Q^s can compensate the impact of the line impedance's drop voltage δV by regulating the output voltage of the primary droop control. Hence, equation (5.24) can be driven as:

$$V_{o1} + V_{Q1}^s = V_{pcc} + V_{drop1} + \delta V \tag{5.27}$$

where V_{Q1}^s is the injected voltage from the central controller (SCUM). The operation and design of the SCUM will be demonstrated in section 5.3. If the controller is well design to mitigate the impact of the mismatched voltage drop, the output voltage of equation (5.24) is given as:

$$V_{o1} = V_{pcc} + V_{drop1}, V_{Q1}^s = \delta V \tag{5.28}$$

The unequal reactive power sharing appears because of the different voltage drop across the mismatch line impedance. This mismatched line voltage δV will generate a circulating current between DER units. Equation (5.27) points out the injected voltage from SCUM V_Q^s can compensate the mismatched line voltage δV by adjusting the output voltage of DER units.

5.2.4 Circulating Current Analysis

The mismatched line voltage δV presents a poor power sharing which generates the circulating current between units. The relation between circulating current and reactive power is given as:

$$S_i = 3V_{oi}I_{oi}^* = 3V_{oi}(\frac{V_{oi} - V_{pcc}}{Z_{ni}})^* \tag{5.29}$$

In [138], the authors define the circulating current between two DER units as:

$$I_{cc1} = \frac{I_{o1} - I_{o2}}{2} \tag{5.30}$$

$$I_{cc2} = \frac{I_{o2} - I_{o1}}{2} \tag{5.31}$$

However, this definition is only valid when the line impedances are the similarities between DER units. Since it is assumed that the line impedance is not identical, the definition of the circulating current needs to be changed based on the power-sharing ratio of each DER unit. To illustrate of the different power sharing ratio of DER units, Fig. 5.3 shows the circulating current of a microgrid which consists of two DER units. A new definition of the circulating current for multiple DER units is given from Fig. 5.3 as:

$$I_{oi} = I_{cci} + n_i I_{load} \tag{5.32}$$

$$I_{load} = \frac{V_{pcc}}{Z_{load}} \tag{5.33}$$

$$\sum_{j=1}^{i} n_j = 1 \tag{5.34}$$

where n_i is the ratio of shared power of each DER unit; I_{load} is the shared load current; Z_{load} is the load impedance. The term of $(n_i I_{load})$ on equation (5.32) represents the equivalent shared ratio of the load power of each DER unit. Kirchhoff law is applied on Fig. 5.3 to find the derivation of circulating current based on voltage terms shown below:

$$I_{cci} = I_{oi} - n_i I_{load} = \frac{V_{oi} - V_{pcc}}{Z_{ni}} \tag{5.35}$$

Equation (5.35) shows that the load power will also impact on the circulating current. Since the line impedance between two DER units is not identical because of the voltage δV as given in equation (5.24), the PCC bus is facing two different values of DER's voltages. According to the relation between the output voltage V_{oi} and the PCC voltage V_{pcc}, equation (5.35) is changed based on the mismatched line voltage δV as:

$$I_{cci} = \frac{\delta V}{Z_{ni}} \tag{5.36}$$

According to the analyzing of reactive power and circulating current in equations (5.24) and (5.36), the mismatched line voltage has a major impact on circulating current. Substituting equa-

tions (5.35) and (5.36) into equation (5.29), the total output power from DER units at mismatched line impedance is given as:

$$S_{oi} = 3(V_{oi} + \delta V)({I_{cci}}^* + n_i {I_{load}}^*) \tag{5.37}$$

$$= 3\left(V_{oi}(\frac{\delta V^*}{Z_{ni}^*}) + V_{oi} n_i I_{load}^* + \frac{\delta V \delta V^*}{Z_{ni}^*} + \delta V n_i I_{load}^*\right) \tag{5.38}$$

Equation (5.38) shows that the voltage drop across the mismatched line impedance presents additional terms on the output DER's power. The output complex powers include actual power and circulating-current power which is driven from equation (5.38) as:

$$S_{oi} = 3V_{oi} n_i I_{load}^* \tag{5.39}$$

$$S_{cci} = 3\left(V_{oi}(\frac{\delta V^*}{Z_{ni}^*}) + \frac{V_{oi}\delta V^*}{Z_{ni}^*} + \delta V n_i I_{load}^*\right) \tag{5.40}$$

This section verifies that the mismatched line voltage generates the poor reactive power sharing and circulating current. When the secondary controller SCUM achieves to compensate the mismatched line voltage $\delta V = 0$, the circulating-current power will disappear as shown in equation (5.40). Thus, the complex output power consists only the actual load's power. So, designing sufficient central controller needs also to reject the impact of the load disturbance on the circulating current as shown in equation (5.35).

5.3 Proposed Secondary Control

5.3.1 Concept and Topology

Coordination of parallel DER units using droop control may cause a couple of issues such as poor reactive power sharing and circulating current. Due to the impact of network impedance, conventional droop control provides a poor reactive power sharing. Circulating current analysis shows that voltage drop δV has a huge impact on the reactive power sharing. So, secondary central control is implemented using SCUM to reject the impact of mismatched line voltage δV. The secondary control SCUM is realized by communication bus to achieve equal reactive power sharing.

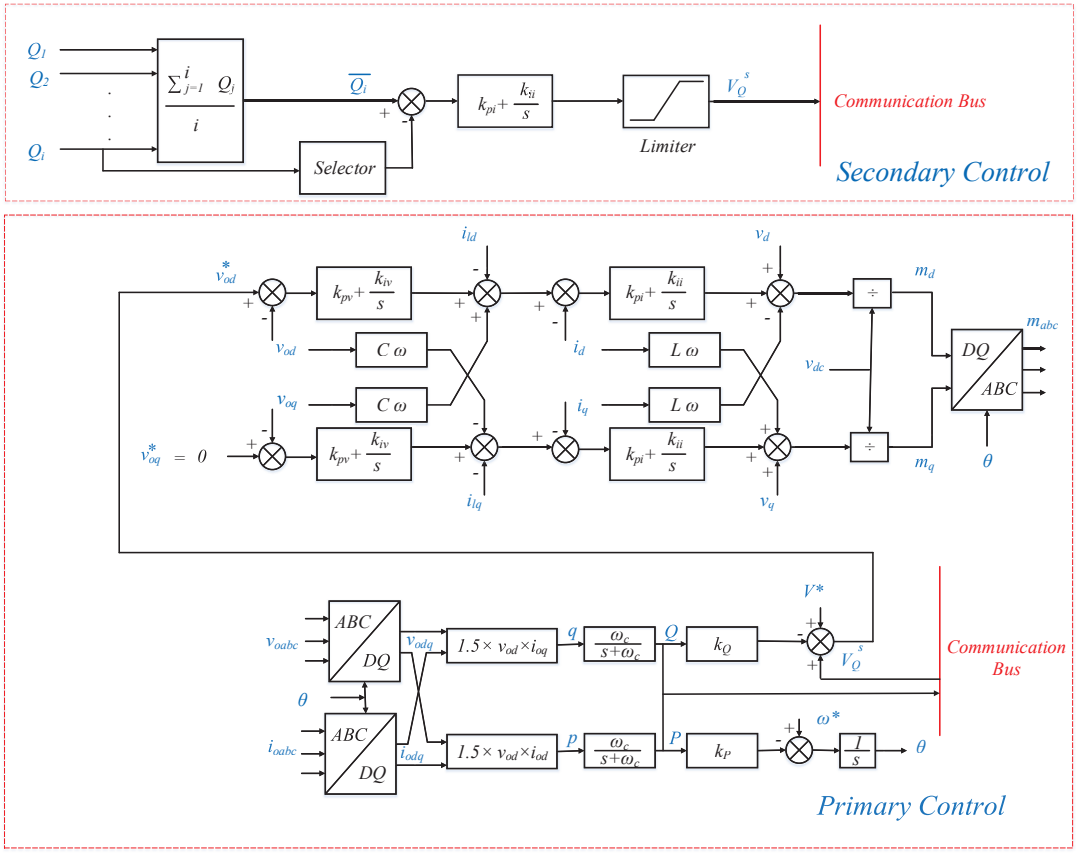

Figure 5.4. Detailed primary and secondary controllers for autonomous microgrid

The detailed controlling block diagram of controlling the microgrid is shown in Fig. 5.4 which includes primary and secondary controllers. The primary control measures the output voltage and frequency to calculate the average powers. The average powers are extracted using a low-pass filter with a bandwidth frequency (ω_c). The reference voltage and frequency are then determined based on assigned droop gains based on the vector control concept on Fig. 5.4. The cascaded inner loops are controlled on DQ reference frame using PI compensators. The controller is implemented in synchronous rotating frame DQ as shown in Fig. 5.4. Designing the cascaded inner loops can be found in [139], being out of the scope of this paper. Each DER unit needs to calculate average powers to share the information with the SCUM via a communication bus. The SCUM calculates the average reactive power and sends the corrected voltage k^s_{iQi} to the primary control.

The simple design of proposed controller aims to decrease the cost and complexity of the system. As shown in equation (5.35), load changing influences on the circulating current. Thus, design PI controller of the SCUM requires achieving disturbance rejection as well as equal reactive power sharing. It is important to mention that when there is an error in transmitting the information using communication bus, the microgrid still generating voltage and frequency using the primary control.

Sharing the information between SCUM and DER units is achieved via the communication bus. Each DER unit needs to calculate the average output power from the primary control and it to SCUM. The corrected voltage reference SCUM V_{Qi}^{s} is transmitted back to each DER unit via communication bus as shown in Fig. 5.4. This voltage can mitigate the impact of mismatched line voltage even at frequent load disturbance. This technique can also be used for high or low R/X microgrid since it does not require information of the line impedance. Generally, the bandwidth of communication link has to decrease in higher levels of controlling a microgrid. Since the transferred signals are averaged and fundamental, low-bandwidth communication is only required for transferring information. This feature can reduce the cost of communication bus as well as increase the reliability of the microgrid.

5.3.2 Controlling Strategy

The averaged reactive power of all DER units is calculated by SCUM and compared with the fundamental output power from each DER unit via low-bandwidth communication bus as shown in Fig 5.4. The error between the average reactive power and the fundamental reactive power is regulated by PI compensator of the SCUM. PI controller guarantees that the steady state error equals zero. The selector block aims to identify each signal from DER unit in order to generate a corrected voltage. The regulated voltage $V_{Q_i}^{s}$ is calculated based on the following equation as:

$$V_{Q_i}^{s} = k_{pQi}^{s}(\bar{Q} - Q_{oi}) + k_{iQi}^{s}\int(\bar{Q} - Q_{oi})dt \tag{5.41}$$

$$\bar{Q} = \frac{\sum_{j=1}^{i} Q_{oj}}{i} \tag{5.42}$$

where $V^s_{Q_i}$ is the injected voltage from SCUM to each ith DER unit; k^s_{pQi} and k^s_{iQi} are the parameters of PI compensator of SCUM; $\bar{Q}$ is the average reactive power required by the load.

The control block diagram of the reactive power loop with voltage profile using SCUM and primary control is shown in Fig. 5.5. The reactive power control includes SCUM to process equal power sharing by comparing the error of calculated average reactive power with the measured power. The primary control has been modeled based on equation (5.9) where a low-pass filter (ω_c) is applied to extract the fundamental reactive power from the instantaneous one.

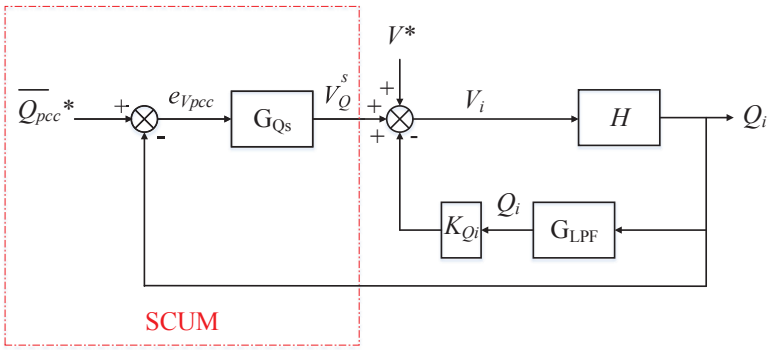

Figure 5.5. Block diagram of reactive power control

The block diagram of the voltage control using SCUM and primary control is shown in Fig. 5.5. The figure shows the controlling technique for reactive power control. The SCUM monitors the average reactive power at PCC and sends a corrected voltage to gain equal power sharing. The closed-loop characteristic of reactive power control is given from Fig. 5.5 as:

$$Q_i = \frac{HV^*}{1 + HG_{Qs}Hk_{Qi}G_{LPF}} + \frac{HG_{Qs}}{1 + HG_{Qs}Hk_{Qi}G_{LPF}}Q^*_{pcc} \tag{5.43}$$

where

$$G_{V^s} = G_{Qs} = k^s_{pQ} + \frac{k^s_{iQ}}{s}, G_{LPF} = \frac{\omega_c}{s + \omega_c}$$
$$H = \frac{V_{oi} - V_{oi}V_{pcc}\cos(\theta_i)}{X_{ni}}$$

5.4 Simulation Results

The mismatched line impedance presents poor reactive power sharing and circulating current when droop control is applied. The circulating current adds more oscillation to the microgrid since the droop control shows a slow dynamic response. This section simulates the proposed method in order to verify the analysis of the circulating current. The performance of the proposed method is investigated at two operational situations of the system which are stable and oscillator modes. The proposed controller needs to provide equal power sharing during steady state as well as improve the dynamic response during the transient state. The realization of primary and secondary control is achieved via low-bandwidth communication bus.

Table 5.1. System parameters of three DER units forming autonomous microgrid

Symbol	Value	Unit	Comment
S	10	KVA	Power Rating for DER units.
V_o	120	V	Nominal Phase Voltage for the microgrid.
ω	377	Hz	Nominal Frequency for the microgrid.
V_{dc}	500	V	Dc-link Voltage for DER units.
F_s	5	kHz	Switching Frequency for DER units.
L_f	5	mH	Filter Inductance for DER units.
C_f	250	uF	Filter Capacitance for DER units.
L_{n1}	0.5	mH	Line Inductance for first DER unit.
R_{n1}	200	mΩ	Line Resistance for first DER unit.
L_{n2}	1.5	mH	Line Inductance for second DER unit.
R_{n2}	600	mΩ	Line Resistance for second DER unit.
L_{n3}	1	mH	Line Inductance for third DER unit.
R_{n3}	400	mΩ	Line Resistance for third DER unit.
R_{load}	10	kW	Global Linear Load

Implementing central controller (SCUM) of the microgrid in Fig. 5.1 is modeled in Matlab/SimPowerSystems software. The system and control parameters are listed in Tables 5.1 and 5.2. The system includes three DER units to generate voltage and frequency as well as sharing the load power. A mismatched line network is presented in Table 5.1 by assigning different values of each line impedance. It is assumed that the three DER units have similar power ratings. So, the controlling parameters of the primary and secondary controllers for the three DER units are

Table 5.2. Control parameters of primary and secondary controllers

Symbol	Value	Unit	Comment
k_P	0.05-0.0.5	mHz/W	$(P-\omega)$ Droop for DER units.
k_Q	1-1.5	V/Var	$(V-Q)$ Droop for DER units.
k_{pi}	33.3	Ω	Proportional Gain for Current Loop.
k_{ii}	266.7	Ω/s	Integral Gain for Current Loop.
k_{pv}	0.56	Ω^{-1}	Proportional Gain for Voltage Loop.
k_{iv}	411.5	Ω^{-1} /s	Integral Gain for Voltage Loop.
ω_c	30	Hz	Cutoff Frequency
k^s_{pQ}	0.01	uF	Proportional Gain for SCUM Loop.
k^s_{iQ}	0.5	mH	Integral Gain for SCUM Loop.
n_1	0.576		Ratio of Power for First DER unit.
n_2	0.385		Ratio of Power for Second DER unit.
n_3	0.0385		Ratio of Power for Third DER unit.

identical. Two case studies are given in this section to investigate the performance of the proposed system based on circulating current and reactive power analysis.

5.4.1 Case1: SCUM Operation

Circuiting current and unequal reactive power sharing have commonly appeared when mismatched line impedance is considered between DER units. Droop coefficients are carefully selected based on the power rating of each DER unit. As seen in Fig. 5.6 *a*, equal real power sharing is achieved by selecting optimal values of power droop gain as given in equations (5.8) and (5.9). However, Fig. 5.6 *b* shows a huge difference of the output reactive powers of DER units. This circulating reactive power may overheat the VSC devices as shown in Fig. 5.6 b, when the second DER unit absorbs $3000Var$ of reactive power. The ratio factors of power-sharing of DER units are calculated based on the power-sharing as given in Table 5.2. The different power ratios which are caused by mismatched line impedance, are used to calculate the circulating current. The circulating current equals 5A based on equation (5.32). The voltage drops on the line impedances of DER units are calculated using equation (5.18) which equal $18V$, $35V$, and $26V$, respectively. So, the mismatched impedance voltage is calculated from equation (5.24) which equals 9V. This value generates $5A$ circulating current which needs to be mitigated to achieve equal power.

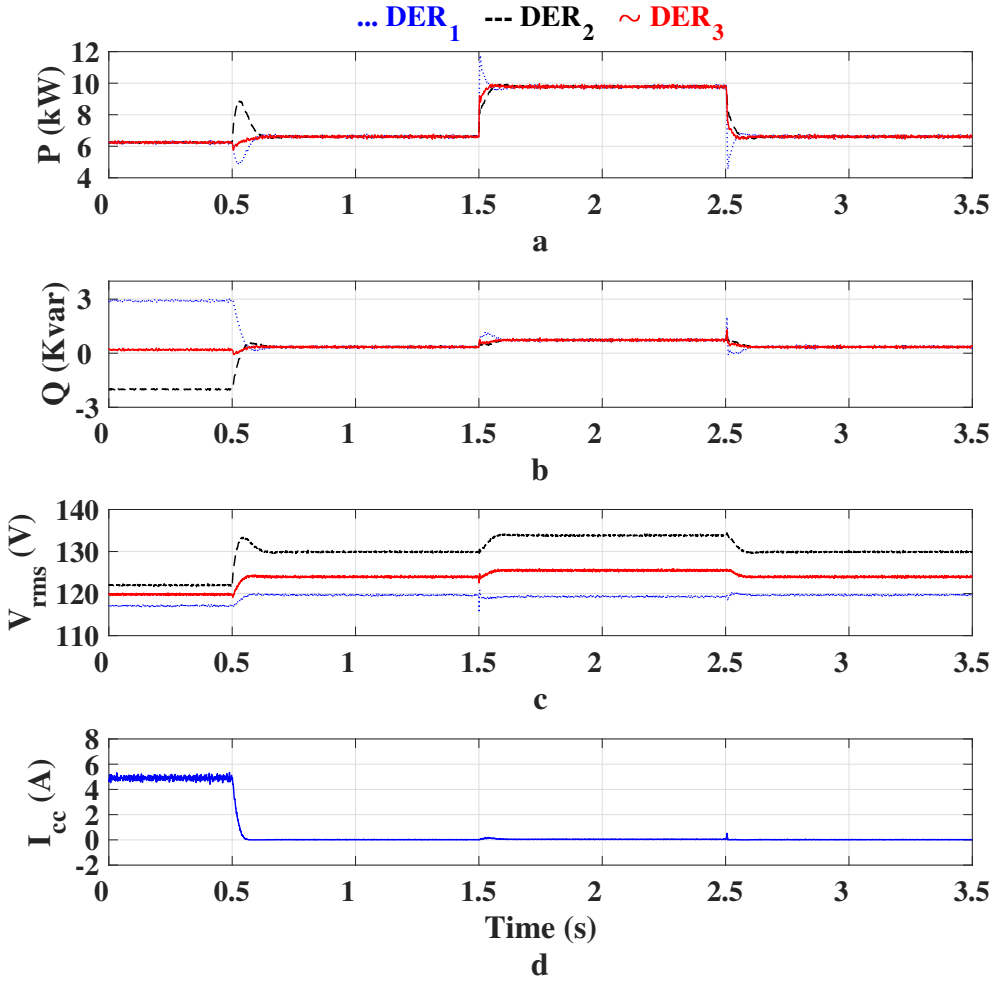

Figure 5.6. Simulation results for case 1 at stable system

To prevent this dangerous circulating current, SCUM is activated at $t = 0.5sec$ by measuring the output average reactive powers and sending a corrected voltage to DER units via the communication bus. This injected voltage compensates the impact of mismatched line voltage δV which is calculated to equal $9V$. Regulating the reactive power is applied using the PI controller while the control signal regulates the output voltage reference of the primary control of each DER unit. By applying SCUM, the mismatched voltage drop δV is mitigated and equal reactive power is achieved as shown in Fig. 5.6 b. Fig. 5.6 d, shows that the circulating current is reduced to $0A$. Fig. 5.6 c, shows the output voltages of DER units. Even these values are different because of the

mismatched line impedance, the proposed controller can mitigate δV which verifies the analysis in subsection 5.2.3. The variation of the voltages is within the 10% limitation of the rated voltage as it is recommended by IEEE standards.

The advantage of the proposed controller is achieving equally reactive power sharing even when the load is a disturbance. As given in equation (5.35), disturbance in the load leads to changing the circulating current. Fig. 5.6 shows an additional $10kW$ load is connected to the system at $t = 1.5sec$. This load disturbance activates the controller in SCUM to regulate the voltage reference on droop controller for each DER unit. Even when the second load is disconnected at $t = 2.5sec$, the SCUM can achieve equal reactive power sharing as well as remove the circulating current.

5.4.2 Case2: SCUM Operation Under Ocillator System

This paper claims that the proposed controller SCUM cannot only achieve equal power sharing, but it can provide more damping to the system during the transient state. Circulating current generates more oscillation to the system when the droop coefficients and low-pass filter of the primary control are not well designed. This case study aims to identify the behavior of the microgrid when the system has high oscillation based on the circulating current. The high value of droop parameters and the high circulating current reduce the dynamic damping of the system when disturbance is applied to the microgrid. The droop coefficients for the three DER units k_P and k_Q are increased from 0.05 to $0.5mHz/W$ and 0.1 to $1.5mV/Var$, respectively. This increasing reduces the dynamic damping response of the system which affects dynamic response at any disturbance.

Fig. 5.7 *a*, shows the system is operated at steady state. A load disturbance is applied at $0.5sec$. It can be seen from Fig. 5.7 that the system has high oscillation around the operating point because of the high circulating current and poor designing of the primary controller. The slow dynamic damping during transient state takes more than $1sec$ to be damped which will reduce the stability of the system. As shown in Fig. 5.7 *d*, the oscillation is affected by the circulating current while this behavior of the system is not recommended behavior based on IEEE standards. This transient behavior affects also the output voltages as shown in Fig. 5.7 *c*. Since the damping response of the system takes more than 1 second, implementing SCUM is essential for system stability.

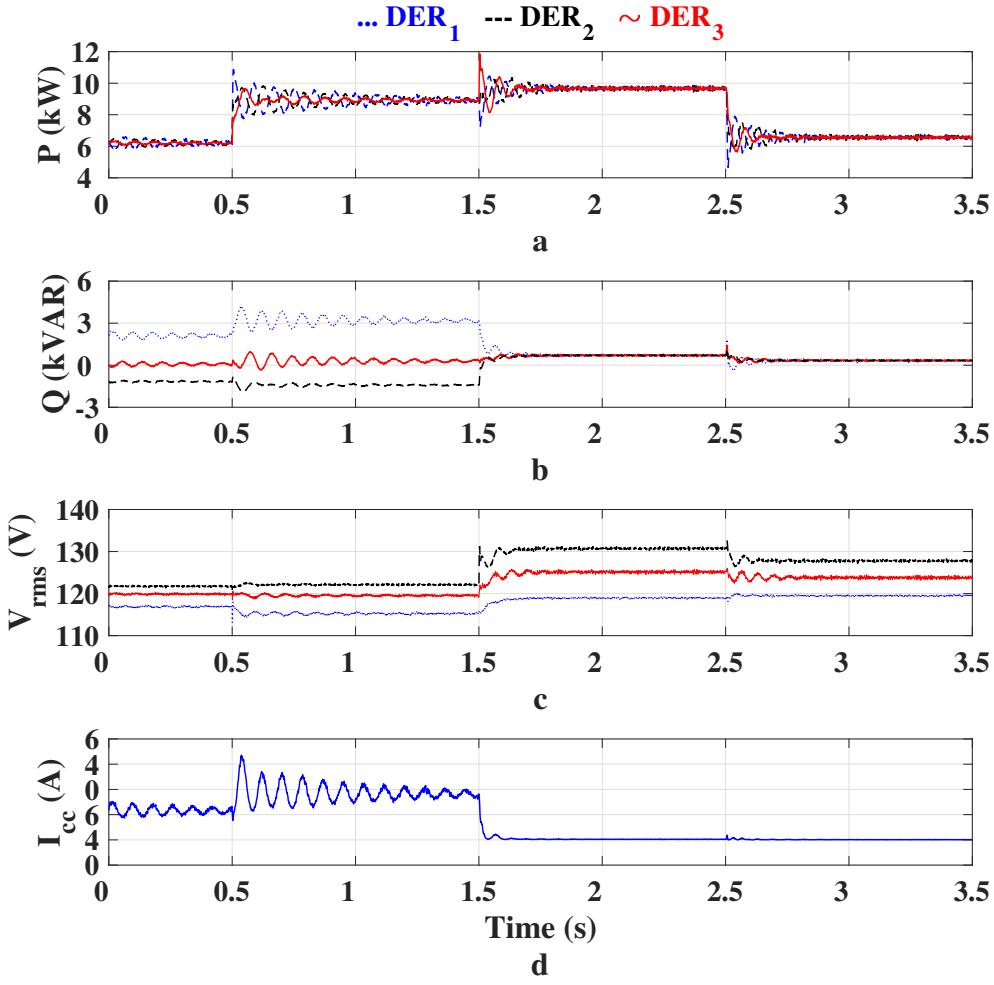

Figure 5.7. Simulation results for case 2 at high oscillated system

At $t = 1.5sec$, the proposed SCUM controller is activated to mitigate the behavior of circulating current by injected a corrected voltage V_Q^s to mitigate the impact of mismatched line voltage δV. It can be seen from Fig. 5.7 that the proposed controller can minimize the circulating current from $5A$ to $0A$ as well as compensate the oscillation in less than $0.2sec$. Removing the circulating current leads to reduce the oscillation of the system. This feature proves that the proposed controller can provide mode dynamic damping at the high oscillated system. The simulation also shows that the proposed method can overcome the slow dynamic behavior of the primary controller. At $t = 2.5sec$,

Fig. 5.7 shows that more damping is realized when the load is changing. Fig. 5.7 shows that the circulating current is removed even when there is load disturbance.

5.5 Conclusion

Implementing conventional droop control may generate potential obstacles for an autonomous microgrid at mismatched line impedance such as load power-sharing inaccuracy and circulating currents. The slow dynamic response of droop control generates a stability issue when circulating current is addressed during the transient state. This paper develops modeling and analysis of a proposed microgrid control using the secondary central unit (SCUM) for paralleled DER units. It also drives the reactive power sharing and circulating current analysis when mismatched line impedance is presented. The proposed power-sharing using SCUM which is realized via a communication bus, can improve the reactive power sharing as well as remove the circulating current. Regarding tuning the primary droop parameters, SCUM enhances the dynamic performance of the system without affecting the static droop gains. The simulation results show that the proposed technique improves the dynamic response and reactive power sharing of the system by compensating the impact of mismatched line voltage δV.

CHAPTER 6

CONCLUSIONS AND FUTURE WORK

6.1 Conclusion

This dissertation can be concluded in five parts as follows.

First, the detailed controller design of smart inverter and VSC is derived in chapter 2. The topology of the inverter and designing of filters, dc-link capacitor, and PLL are also provided. Tuning technique is proposed in this chapter to regulate the compensator of the smart inverter's controller. Two main connection mode are presented which are autonomous mode and grid-connected mode. Each operational mode requires a specific control algorithm which has been driven and presented in detailed.

Second, the smart inverter control of motor drives is provided in chapter 3. Two applications are presented in this chapter. The issues of blackstart and CMV are also demonstrated. The issue of controlling of a weak autonomous microgrid is also presented. Different techniques are used to mitigate the impact of starting current of induction motor's load. In this chapter, black start problem of the induction motor when connecting to a weak microgrid is presented. The consequences of applying the reduced CMV-PWM method for smart inverter at grid-connected mode with induction motor load are well reviewed as well. In this chapter, implementation of AZPWM based VSC at an autonomous mode is presented. The research provides a method to reduce CMV for control VF and switching states of the smart inverter at the terminal induction motor's load.

Third, the novel topology of smart inverter is [resented in chapter 4. The control of three-phase HBC in a PV charging station is also proposed. The three-phase HBC can save switching losses by integration a dc/dc booster and a dc/ac converter into a single converter structure. A new control for the three-phase HBC is designed to achieve MPPT, dc voltage regulation, and reactive power

tracking. The MPPT control utilizes modified incremental conductance-PI based MPPT method. The dc voltage regulation and reactive power tracking are realized using vector control.

Finally, coordination of smart inverters to form a microgrid is demonstrated in chapter 5. The low-level and high-level controlling techniques provide more smart features to the microgrid. Implementing conventional droop control may generate potential obstacles at an autonomous microgrid such as load power-sharing inaccuracy, voltage, and frequency variation, circulating currents and power coupling issue. This chapter develops modeling and analysis of a proposed microgrid control using the secondary central unit (SCUM) for paralleled inverter-based distributed generation (DER) units. The high circulating current leads to more oscillation behavior on the system. The proposed power sharing using SCUM can achieve voltage and frequency restoration as well as equally reactive power sharing. Regarding tuning the primary droop parameters, SCUM enhances the dynamic performance of the system without affecting the static droop gains. The proposed technique guarantees power oscillations at different operation modes

6.2 Future Work

The future work of this dissertation can contain the following parts.

First, a smart inverter based microgrid with different renewable energy resources can be implemented in real applications using LabView software. The PV charging station can also be issued to distribute a technology of charging PHEV batteries. The central controller of the microgrid will be implemented in the real microgrid to investigate the impact of data transmission and communication between DER units.

Second, the stability of a weak microgrid needs more investigation. The impact of the induction motor's load and the participation of central control require more analysis. Under weak system scenario, the operation of the microgrid is unstable and more stability analysis is required.

Finally, hierarchical control algorithms will be implemented in a real application of the microgrid. For example, the central controller will improve to involve distributed control instead of a central control unit. Cost function and optimization will be implemented in tertiary control.

REFERENCES

[1] R. Teodorescu, M. Liserre, and P. Rodriguez, *Grid converters for photovoltaic and wind power systems*. John Wiley & Sons, 2011, vol. 29.

[2] T. Esram and P. L. Chapman, "Comparison of photovoltaic array maximum power point tracking techniques," *IEEE Transactions on energy conversion*, vol. 22, no. 2, pp. 439–449, 2007.

[3] B. Yang, W. Li, Y. Zhao, and X. He, "Design and analysis of a grid-connected photovoltaic power system," *IEEE Transactions on Power Electronics*, vol. 25, no. 4, pp. 992–1000, 2010.

[4] F. Liu, Y. Kang, Y. Zhang, and S. Duan, "Comparison of p&o and hill climbing mppt methods for grid-connected pv converter," in *Industrial Electronics and Applications, 2008. ICIEA 2008. 3rd IEEE Conference on*. IEEE, 2008, pp. 804–807.

[5] W. Xiao and W. G. Dunford, "A modified adaptive hill climbing mppt method for photovoltaic power systems," in *Power Electronics Specialists Conference, 2004. PESC 04. 2004 IEEE 35th Annual*, vol. 3. Ieee, 2004, pp. 1957–1963.

[6] D. Hohm and M. Ropp, "Comparative study of maximum power point tracking algorithms using an experimental, programmable, maximum power point tracking test bed," in *Photovoltaic Specialists Conference, 2000. Conference Record of the Twenty-Eighth IEEE*. IEEE, 2000, pp. 1699–1702.

[7] J. H. Lee, H. Bae, and B. H. Cho, "Advanced incremental conductance mppt algorithm with a variable step size," in *Power Electronics and Motion Control Conference, 2006. EPE-PEMC 2006. 12th International*. IEEE, 2006, pp. 603–607.

[8] Y.-C. Kuo, T.-J. Liang, and J.-F. Chen, "Novel maximum-power-point-tracking controller for photovoltaic energy conversion system," *IEEE transactions on industrial electronics*, vol. 48, no. 3, pp. 594–601, 2001.

[9] M. Ciobotaru, R. Teodorescu, and F. Blaabjerg, "Control of single-stage single-phase pv inverter," *EPE Journal*, vol. 16, no. 3, pp. 20–26, 2006.

[10] B. Liu, S. Duan, and T. Cai, "Photovoltaic dc-building-module-based bipv system?concept and design considerations," *IEEE Transactions on Power Electronics*, vol. 26, no. 5, pp. 1418–1429, 2011.

[11] M. A. Eltawil and Z. Zhao, "Grid-connected photovoltaic power systems: Technical and potential problems?a review," *Renewable and Sustainable Energy Reviews*, vol. 14, no. 1, pp. 112–129, 2010.

[12] Y. Xue, K. C. Divya, G. Griepentrog, M. Liviu, S. Suresh, and M. Manjrekar, "Towards next generation photovoltaic inverters," in *Energy Conversion Congress and Exposition (ECCE), 2011 IEEE*. IEEE, 2011, pp. 2467–2474.

[13] S.-J. Chiang, K. Chang, and C. Yen, "Residential photovoltaic energy storage system," *IEEE Transactions on industrial electronics*, vol. 45, no. 3, pp. 385–394, 1998.

[14] M. Bragard, N. Soltau, S. Thomas, and R. W. De Doncker, "The balance of renewable sources and user demands in grids: Power electronics for modular battery energy storage systems," *IEEE Transactions on Power Electronics*, vol. 25, no. 12, pp. 3049–3056, 2010.

[15] S. Vazquez, S. M. Lukic, E. Galvan, L. G. Franquelo, and J. M. Carrasco, "Energy storage systems for transport and grid applications," *IEEE Transactions on Industrial Electronics*, vol. 57, no. 12, pp. 3881–3895, 2010.

[16] B. Zakeri and S. Syri, "Electrical energy storage systems: A comparative life cycle cost analysis," *Renewable and Sustainable Energy Reviews*, vol. 42, pp. 569–596, 2015.

[17] H. Mahmood, D. Michaelson, and J. Jiang, "A power management strategy for pv/battery hybrid systems in islanded microgrids," *IEEE Journal of Emerging and Selected topics in Power electronics*, vol. 2, no. 4, pp. 870–882, 2014.

[18] D. Guasch and S. Silvestre, "Dynamic battery model for photovoltaic applications," *Progress in Photovoltaics: Research and applications*, vol. 11, no. 3, pp. 193–206, 2003.

[19] T. Dragičević, J. M. Guerrero, J. C. Vasquez, and D. Škrlec, "Supervisory control of an adaptive-droop regulated dc microgrid with battery management capability," *IEEE Transactions on Power Electronics*, vol. 29, no. 2, pp. 695–706, 2014.

[20] G. L. Soloveichik, "Battery technologies for large-scale stationary energy storage," *Annual review of chemical and biomolecular engineering*, vol. 2, pp. 503–527, 2011.

[21] S. Lee, J. Kim, J. Lee, and B. Cho, "State-of-charge and capacity estimation of lithium-ion battery using a new open-circuit voltage versus state-of-charge," *Journal of power sources*, vol. 185, no. 2, pp. 1367–1373, 2008.

[22] V. Ramadesigan, P. W. Northrop, S. De, S. Santhanagopalan, R. D. Braatz, and V. R. Subramanian, "Modeling and simulation of lithium-ion batteries from a systems engineering perspective," *Journal of The Electrochemical Society*, vol. 159, no. 3, pp. R31–R45, 2012.

[23] L. Gao, S. Liu, and R. A. Dougal, "Dynamic lithium-ion battery model for system simulation," *IEEE transactions on components and packaging technologies*, vol. 25, no. 3, pp. 495–505, 2002.

[24] K. Sikes, T. Gross, Z. Lin, J. Sullivan, T. Cleary, and J. Ward, "Plug-in hybrid electric vehicle market introduction study: final report," Oak Ridge National Laboratory (ORNL), Tech. Rep., 2010.

[25] M. Yilmaz and P. T. Krein, "Review of battery charger topologies, charging power levels, and infrastructure for plug-in electric and hybrid vehicles," *IEEE Transactions on Power Electronics*, vol. 28, no. 5, pp. 2151–2169, May 2013.

[26] M. Ehsani, Y. Gao, and A. Emadi, *Modern electric, hybrid electric, and fuel cell vehicles: fundamentals, theory, and design.* CRC press, 2009.

[27] P. Goli and W. Shireen, "Pv integrated smart charging of phevs based on dc link voltage sensing," *IEEE Transactions on Smart Grid*, vol. 5, no. 3, pp. 1421–1428, 2014.

[28] G. Gamboa, C. Hamilton, R. Kerley, S. Elmes, A. Arias, J. Shen, and I. Batarseh, "Control strategy of a multi-port, grid connected, direct-dc pv charging station for plug-in electric vehicles," in *Energy Conversion Congress and Exposition (ECCE), 2010 IEEE*. IEEE, 2010, pp. 1173–1177.

[29] M. S. Rahman, M. Hossain, and J. Lu, "Coordinated control of three-phase ac and dc type ev–esss for efficient hybrid microgrid operations," *Energy Conversion and Management*, vol. 122, pp. 488–503, 2016.

[30] F. Katiraei, C. Sun, and B. Enayati, "No inverter left behind: Protection, controls, and testing for high penetrations of pv inverters on distribution systems," *Power and Energy Magazine, IEEE*, vol. 13, no. 2, pp. 43–49, March 2015.

[31] EPRI, "Common functions for smart inverters: 4th edition," 2016. [Online]. Available: http://www2.epri.com/abstracts/Pages/ProductAbstract.aspx?ProductId=000000003002008217

[32] E. Malashenko, S. Appert, and W. al Mukdad, "Advanced inverter technologies report," *California Public Utilities Commission*, pp. 1–13, 2013.

[33] SAE, "Security for plug-in electric vehicle communications," 2017. [Online]. Available: http://standards.sae.org/j2931/7_201710/

[34] B. Seal, "Common functions for smart inverters, version 2," *EPRI, Palo Alto, CA*, vol. 1026809, 2012.

[35] "Ieee recommended practice for industrial and commercial power systems analysis (brown book)," *IEEE Std 399-1997*, pp. 1–488, Aug 1998.

[36] M. Swamy, K. Yamada, and T. Kume, "Common mode current attenuation techniques for use with pwm drives," *Power Electronics, IEEE Transactions on*, vol. 16, no. 2, pp. 248–255, Mar 2001.

[37] G. Skibinski, R. Kerkman, and D. Schlegel, "Emi emissions of modern pwm ac drives," *Industry Applications Magazine, IEEE*, vol. 5, no. 6, pp. 47–80, Nov 1999.

[38] O. Ray and S. Mishra, "Boost-derived hybrid converter with simultaneous dc and ac outputs," *IEEE Transactions on Industry Applications*, vol. 50, no. 2, pp. 1082–1093, March 2014.

[39] ——, "Integrated hybrid output converter as power router for renewable-based nanogrids," in *Industrial Electronics Society, IECON 2015 - 41st Annual Conference of the IEEE*, Nov 2015, pp. 001 645–001 650.

[40] O. Ray, V. Dharmarajan, S. Mishra, R. Adda, and P. Enjeti, "Analysis and pwm control of three-phase boost-derived hybrid converter," in *2014 IEEE Energy Conversion Congress and Exposition (ECCE)*, Sept 2014, pp. 402–408.

[41] S. Vazquez, J. A. Sanchez, J. M. Carrasco, J. I. Leon, and E. Galvan, "A model-based direct power control for three-phase power converters," *IEEE Transactions on Industrial Electronics*, vol. 55, no. 4, pp. 1647–1657, 2008.

[42] M. Malinowski, M. P. Kazmierkowski, S. Hansen, F. Blaabjerg, and G. Marques, "Virtual-flux-based direct power control of three-phase pwm rectifiers," *IEEE Transactions on industry applications*, vol. 37, no. 4, pp. 1019–1027, 2001.

[43] M. Malinowski, M. Jasinski, and M. P. Kazmierkowski, "Simple direct power control of three-phase pwm rectifier using space-vector modulation (dpc-svm)," *IEEE Transactions on Industrial Electronics*, vol. 51, no. 2, pp. 447–454, 2004.

[44] L. Zhang, L. Harnefors, and H.-P. Nee, "Power-synchronization control of grid-connected voltage-source converters," *IEEE Transactions on Power systems*, vol. 25, no. 2, pp. 809–820, 2010.

[45] ——, "Interconnection of two very weak ac systems by vsc-hvdc links using power-synchronization control," *IEEE transactions on power systems*, vol. 26, no. 1, pp. 344–355, 2011.

[46] A. Yazdani and R. Iravani, *Voltage-sourced converters in power systems: modeling, control, and applications*. John Wiley & Sons, 2010.

[47] J. Rodriguez, E. Pena, P. Larrea, H. Duarte, and A. Rodriguez, "Dynamic performance of a statcom under grid disturbances for two different linear controllers," in *IECON 2012 - 38th Annual Conference on IEEE Industrial Electronics Society*, Oct 2012, pp. 356–361.

[48] L. Zhang, L. Harnefors, and H.-P. Nee, "Power-synchronization control of grid-connected voltage-source converters," *Power Systems, IEEE Transactions on*, vol. 25, no. 2, pp. 809–820, May 2010.

[49] M. Kazmierkowski and L. Malesani, "Current control techniques for three-phase voltage-source pwm converters: a survey," *Industrial Electronics, IEEE Transactions on*, vol. 45, no. 5, pp. 691–703, Oct 1998.

[50] N. Mohan and T. M. Undeland, *Power electronics: converters, applications, and design*. John Wiley & Sons, 2007.

[51] "Ieee recommended practices and requirements for harmonic control in electrical power systems," *IEEE Std 519-1992*, pp. 1–112, April 1993.

[52] "Ieee standard for interconnecting distributed resources with electric power systems," *IEEE Std 1547-2003*, pp. 1–28, July 2003.

[53] N. Li, N. Zhi, H. Zhang, Y. Wang *et al.*, "A novel output lc filter design method of high power three-level npc converter," in *Power Electronics and Application Conference and Exposition (PEAC), 2014 International*. IEEE, 2014, pp. 68–71.

[54] M. M. de Oliveira, "Power electronics for mitigation of voltage sags and improved control of ac power systems," Ph.D. dissertation, Citeseer, 2000.

[55] J. M. Guerrero, J. C. Vasquez, J. Matas, L. G. De Vicuña, and M. Castilla, "Hierarchical control of droop-controlled ac and dc microgrids?a general approach toward standardization," *IEEE Transactions on Industrial Electronics*, vol. 58, no. 1, pp. 158–172, 2011.

[56] J. M. Guerrero, J. C. Vasquez, J. Matas, M. Castilla, and L. G. de Vicuna, "Control strategy for flexible microgrid based on parallel line-interactive ups systems," *IEEE Transactions on Industrial Electronics*, vol. 56, no. 3, pp. 726–736, 2009.

[57] J. M. Guerrero, J. Matas, L. G. D. V. De Vicuna, M. Castilla, and J. Miret, "Wireless-control strategy for parallel operation of distributed-generation inverters," *IEEE Transactions on Industrial Electronics*, vol. 53, no. 5, pp. 1461–1470, 2006.

[58] J. C. Vasquez, R. A. Mastromauro, J. M. Guerrero, and M. Liserre, "Voltage support provided by a droop-controlled multifunctional inverter," *IEEE Transactions on Industrial Electronics*, vol. 56, no. 11, pp. 4510–4519, 2009.

[59] M. C. Chandorkar, D. M. Divan, and R. Adapa, "Control of parallel connected inverters in standalone ac supply systems," *IEEE Transactions on Industry Applications*, vol. 29, no. 1, pp. 136–143, 1993.

[60] A. Madureira, C. Moreira, and J. P. Lopes, "Secondary load-frequency control for microgrids in islanded operation," in *Proc. Int. Conf. Renewable Energy Power Quality*, 2005.

[61] J. P. Lopes, C. Moreira, and A. Madureira, "Defining control strategies for microgrids islanded operation," *IEEE Transactions on power systems*, vol. 21, no. 2, pp. 916–924, 2006.

[62] A. Mehrizi-Sanir and R. Iravani, "Secondary control for microgrids using potential functions: Modeling issues," *Proceedings of the Conseil International des Grands Résaux Électriques (CIGRE)*, vol. 182, 2009.

[63] K. Vanthournout, K. De Brabandere, E. Haesen, J. Van den Keybus, G. Deconinck, and R. Belmans, "Agora: Distributed tertiary control of distributed resources," in *Proc. 15th Power Systems Computation Conf*, 2005, pp. 1–7.

[64] A. Madureira and J. P. Lopes, "Voltage and reactive power control in mv networks integrating microgrids," in *Proc. Int. Conf. Renewable Energy Power Quality*, 2007.

[65] F. Gao and M. Iravani, "A control strategy for a distributed generation unit in grid-connected and autonomous modes of operation," *Power Delivery, IEEE Transactions on*, vol. 23, no. 2, pp. 850–859, April 2008.

[66] A. Ghoshal and V. John, "A method to improve pll performance under abnormal grid conditions," 2007.

[67] V. Kaura and V. Blasko, "Operation of a phase locked loop system under distorted utility conditions," *IEEE Transactions on Industry Applications*, vol. 33, no. 1, pp. 58–63, Jan 1997.

[68] C. Bajracharya, M. Molinas, J. A. Suul, T. M. Undeland *et al.*, "Understanding of tuning techniques of converter controllers for vsc-hvdc," in *Nordic Workshop on Power and Industrial Electronics (NORPIE/2008), June 9-11, 2008, Espoo, Finland*. Helsinki University of Technology, 2008.

[69] A. Williams and M. Griffith, "Evaluating the effects of motor starting on industrial and commercial power systems," *Industry Applications, IEEE Transactions on*, vol. IA-14, no. 4, pp. 292–305, July 1978.

[70] F. M. Bruce, R. J. Graefe, A. Lutz, and M. D. Panlener, "Reduced-voltage starting of squirrel-cage induction motors," *Industry Applications, IEEE Transactions on*, vol. IA-20, no. 1, pp. 46–55, Jan 1984.

[71] J. Holtz, "Pulsewidth modulation-a survey," *Industrial Electronics, IEEE Transactions on*, vol. 39, no. 5, pp. 410–420, 1992.

[72] H. W. Van Der Broeck, H.-C. Skudelny, and G. V. Stanke, "Analysis and realization of a pulsewidth modulator based on voltage space vectors," *Industry Applications, IEEE Transactions on*, vol. 24, no. 1, pp. 142–150, 1988.

[73] A. M. Hava and E. Un, "Performance analysis of reduced common-mode voltage pwm methods and comparison with standard pwm methods for three-phase voltage-source inverters," *Power Electronics, IEEE Transactions on*, vol. 24, no. 1, pp. 241–252, 2009.

[74] P. C. Sen, *Principles of electric machines and power electronics*. John Wiley & Sons, 2007.

[75] "Ieee guide for planning dc links terminating at ac locations having low short-circuit capacities," *IEEE Std 1204-1997*, pp. i–, 1997.

[76] A. M. Hava, R. J. Kerkman, and T. A. Lipo, "Simple analytical and graphical methods for carrier-based pwm-vsi drives," *Power Electronics, IEEE Transactions on*, vol. 14, no. 1, pp. 49–61, 1999.

[77] W. Price, C. Taylor, and G. Rogers, "Standard load models for power flow and dynamic performance simulation," *IEEE Transactions on power systems*, vol. 10, no. CONF-940702–, 1995.

[78] W.-F. Zhang and Y.-H. Yu, "Comparison of three svpwm strategies," *Journal of electronic science and technology of china*, vol. 5, no. 3, pp. 283–287, 2007.

[79] R. H. Lasseter, "Microgrids," in *Power Engineering Society Winter Meeting, 2002. IEEE*, vol. 1. IEEE, 2002, pp. 305–308.

[80] J. M. Carrasco, L. G. Franquelo, J. T. Bialasiewicz, E. Galván, R. C. P. Guisado, M. Á. M. Prats, J. I. León, and N. Moreno-Alfonso, "Power-electronic systems for the grid integration of renewable energy sources: A survey," *Industrial Electronics, IEEE Transactions on*, vol. 53, no. 4, pp. 1002–1016, 2006.

[81] L. Zhang, K. Sun, Y. Xing, L. Feng, and H. Ge, "A modular grid-connected photovoltaic generation system based on dc bus," *IEEE Transactions on Power Electronics*, vol. 26, no. 2, pp. 523–531, Feb 2011.

[82] A. Emadi, K. Rajashekara, S. S. Williamson, and S. M. Lukic, "Topological overview of hybrid electric and fuel cell vehicular power system architectures and configurations," *Vehicular Technology, IEEE Transactions on*, vol. 54, no. 3, pp. 763–770, 2005.

[83] R. C. Green, L. Wang, and M. Alam, "The impact of plug-in hybrid electric vehicles on distribution networks: A review and outlook," *Renewable and sustainable energy reviews*, vol. 15, no. 1, pp. 544–553, 2011.

[84] ——, "The impact of plug-in hybrid electric vehicles on distribution networks: a review and outlook," in *IEEE PES General Meeting*, July 2010, pp. 1–8.

[85] M. Tabari and A. Yazdani, "Stability of a dc distribution system for power system integration of plug-in hybrid electric vehicles," *IEEE Transactions on Smart Grid*, vol. 5, no. 5, pp. 2564–2573, Sept 2014.

[86] D. Aggeler, F. Canales, H. Zelaya, D. La Parra, A. Coccia, N. Butcher, and O. Apeldoorn, "Ultra-fast dc-charge infrastructures for ev-mobility and future smart grids," in *Innovative Smart Grid Technologies Conference Europe (ISGT Europe), 2010 IEEE PES*. IEEE, 2010, pp. 1–8.

[87] A. Arancibia and K. Strunz, "Modeling of an electric vehicle charging station for fast dc charging," in *Electric Vehicle Conference (IEVC), 2012 IEEE International*. IEEE, 2012, pp. 1–6.

[88] S. Bai and S. M. Lukic, "Unified active filter and energy storage system for an mw electric vehicle charging station," *IEEE Transactions on Power Electronics*, vol. 28, no. 12, pp. 5793–5803, 2013.

[89] H.-M. Neumann, D. Schär, and F. Baumgartner, "The potential of photovoltaic carports to cover the energy demand of road passenger transport," *Progress in Photovoltaics: Research and Applications*, vol. 20, no. 6, pp. 639–649, 2012.

[90] P. J. Tulpule, V. Marano, S. Yurkovich, and G. Rizzoni, "Economic and environmental impacts of a pv powered workplace parking garage charging station," *Applied Energy*, vol. 108, pp. 323–332, 2013.

[91] M. Tabari and A. Yazdani, "Stability of a dc distribution system for power system integration of plug-in hybrid electric vehicles," *IEEE Transactions on Smart Grid*, vol. 5, no. 5, pp. 2564–2573, 2014.

[92] F. Z. Peng, M. Shen, and Z. Qian, "Maximum boost control of the z-source inverter," *IEEE Transactions on Power Electronics*, vol. 20, no. 4, pp. 833–838, July 2005.

[93] S. H. Hwang and J. M. Kim, "Dead time compensation method for voltage-fed pwm inverter," *IEEE Transactions on Energy Conversion*, vol. 25, no. 1, pp. 1–10, March 2010.

[94] S. Mishra, R. Adda, and A. Joshi, "Inverse watkins–johnson topology-based inverter," *IEEE Transactions on Power Electronics*, vol. 27, no. 3, pp. 1066–1070, 2012.

[95] ——, "Switched-boost inverter based on inverse watkins-johnson topology," in *Energy Conversion Congress and Exposition (ECCE), 2011 IEEE*. IEEE, 2011, pp. 4208–4211.

[96] U. Eicker, *Solar technologies for buildings*. John Wiley & Sons, 2006.

[97] N. Femia, G. Petrone, G. Spagnuolo, and M. Vitelli, *Power electronics and control techniques for maximum energy harvesting in photovoltaic systems.* CRC press, 2012.

[98] M. R. Patel, *Wind and solar power systems: design, analysis, and operation.* CRC press, 2005.

[99] R. W. Erickson and D. Maksimovic, *Fundamentals of power electronics.* Springer Science & Business Media, 2007.

[100] O. Ellabban, J. V. Mierlo, and P. Lataire, "Comparison between different pwm control methods for different z-source inverter topologies," in *Power Electronics and Applications, 2009. EPE '09. 13th European Conference on*, Sept 2009, pp. 1–11.

[101] J. Khazaei, Z. Miao, L. Piyasinghe, and L. Fan, "Real-time digital simulation-based modeling of a single-phase single-stage pv system," *Electric Power Systems Research*, vol. 123, pp. 85–91, 2015.

[102] C. Dorofte, U. Borup, and F. Blaabjerg, "A combined two-method mppt control scheme for grid-connected photovoltaic systems," in *Power electronics and applications, 2005 European conference on.* IEEE, 2005, pp. 10–pp.

[103] D. Dong, B. Wen, D. Boroyevich, P. Mattavelli, and Y. Xue, "Analysis of phase-locked loop low-frequency stability in three-phase grid-connected power converters considering impedance interactions," *IEEE Transactions on Industrial Electronics*, vol. 62, no. 1, pp. 310–321, Jan 2015.

[104] A. Tazay, Z. Miao, and L. Fan, "Blackstart of an induction motor in an autonomous microgrid," in *2015 IEEE Power Energy Society General Meeting*, July 2015, pp. 1–5.

[105] F. Fröhr and F. Orttenburger, *Introduction to electronic control engineering.* Heyden, 1982.

[106] Y. Hu, S. Yurkovich, Y. Guezennec, and B. Yurkovich, "A technique for dynamic battery model identification in automotive applications using linear parameter varying structures," *Control Engineering Practice*, vol. 17, no. 10, pp. 1190–1201, 2009.

[107] P. Fan, B. Sainbayar, and S. Ren, "Operation analysis of fast charging stations with energy demand control of electric vehicles," *IEEE Transactions on Smart Grid*, vol. 6, no. 4, pp. 1819–1826, July 2015.

[108] C. C. Grant, *US National Electric Vehicle Safety Standards Summit: Summary Report.* Fire Protection Research Foundation, 2010.

[109] C. Toepfer, "Sae electric vehicle conductive charge coupler, sae j1772," *Society of Automotive Engineers*, 2009.

[110] D. Linden, "Handbook of batteries and fuel cells," *New York, McGraw-Hill Book Co., 1984, 1075 p. No individual items are abstracted in this volume.*, vol. 1, 1984.

[111] J. Y. Yong, V. K. Ramachandaramurthy, K. M. Tan, and J. Selvaraj, "Experimental validation of a three-phase off-board electric vehicle charger with new power grid voltage control," *IEEE Transactions on Smart Grid*, 2016.

[112] N. Leaf, "2011 leaf owner's manual revised," 2011. [Online]. Available: http://www.nissan-techinfo.com/refgh0v/og/leaf/2011-nissan-leaf.pdf

[113] G. Motors, "2016 chevrolet volt battery system," 2016. [Online]. Available: https://media.gm.com/content/dam/Media/microsites/product/Volt_2016/doc/VOLT_BATTERY.pdf

[114] "Ieee standard for performance criteria and test methods for plug-in (portable) multiservice (multiport) surge-protective devices for equipment connected to a 120 v/240 v single phase power service and metallic conductive communication line(s)," *IEEE Std C62.50-2012*, pp. 1–63, Sept 2012.

[115] K. Moslehi and R. Kumar, "A reliability perspective of the smart grid," *IEEE Transactions on Smart Grid*, vol. 1, no. 1, pp. 57–64, 2010.

[116] P. C. Loh, D. Li, Y. K. Chai, and F. Blaabjerg, "Autonomous operation of hybrid microgrid with ac and dc subgrids," *IEEE transactions on power electronics*, vol. 28, no. 5, pp. 2214–2223, 2013.

[117] D. De and V. Ramanarayanan, "Decentralized parallel operation of inverters sharing unbalanced and nonlinear loads," *IEEE Transactions on Power Electronics*, vol. 25, no. 12, pp. 3015–3025, 2010.

[118] J. M. Guerrero, M. Chandorkar, T.-L. Lee, and P. C. Loh, "Advanced control architectures for intelligent microgrids?part i: Decentralized and hierarchical control," *IEEE Transactions on Industrial Electronics*, vol. 60, no. 4, pp. 1254–1262, 2013.

[119] Y. A.-R. I. Mohamed and E. F. El-Saadany, "Adaptive decentralized droop controller to preserve power sharing stability of paralleled inverters in distributed generation microgrids," *IEEE Transactions on Power Electronics*, vol. 23, no. 6, pp. 2806–2816, 2008.

[120] Y. A.-R. I. Mohamed and A. A. Radwan, "Hierarchical control system for robust microgrid operation and seamless mode transfer in active distribution systems," *IEEE Transactions on Smart Grid*, vol. 2, no. 2, pp. 352–362, 2011.

[121] C.-T. Lee, C.-C. Chu, and P.-T. Cheng, "A new droop control method for the autonomous operation of distributed energy resource interface converters," *IEEE Transactions on Power Electronics*, vol. 28, no. 4, pp. 1980–1993, 2013.

[122] Y. Han, H. Li, P. Shen, E. A. A. Coelho, and J. M. Guerrero, "Review of active and reactive power sharing strategies in hierarchical controlled microgrids," *IEEE Transactions on Power Electronics*, vol. 32, no. 3, pp. 2427–2451, March 2017.

[123] Y. A. R. I. Mohamed and A. A. Radwan, "Hierarchical control system for robust microgrid operation and seamless mode transfer in active distribution systems," *IEEE Transactions on Smart Grid*, vol. 2, no. 2, pp. 352–362, June 2011.

[124] R. Majumder, B. Chaudhuri, A. Ghosh, R. Majumder, G. Ledwich, and F. Zare, "Improvement of stability and load sharing in an autonomous microgrid using supplementary droop control loop," *IEEE Transactions on Power Systems*, vol. 25, no. 2, pp. 796–808, May 2010.

[125] Y. W. Li and C.-N. Kao, "An accurate power control strategy for power-electronics-interfaced distributed generation units operating in a low-voltage multibus microgrid," *IEEE Transactions on Power Electronics*, vol. 24, no. 12, pp. 2977–2988, 2009.

[126] S. Xu, J. Wang, and J. Xu, "A current decoupling parallel control strategy of single-phase inverter with voltage and current dual closed-loop feedback," *IEEE Transactions on Industrial Electronics*, vol. 60, no. 4, pp. 1306–1313, 2013.

[127] M. Hamzeh, H. Mokhtari, and H. Karimi, "A decentralized self-adjusting control strategy for reactive power management in an islanded multi-bus mv microgrid," *Canadian Journal of Electrical and Computer Engineering*, vol. 36, no. 1, pp. 18–25, Winter 2013.

[128] D. Wu, F. Tang, J. M. Guerrero, J. C. Vasquez, G. Chen, and L. Sun, "Autonomous active and reactive power distribution strategy in islanded microgrids," in *2014 IEEE Applied Power Electronics Conference and Exposition - APEC 2014*, March 2014, pp. 2126–2131.

[129] Q. Shafiee, J. M. Guerrero, and J. C. Vasquez, "Distributed secondary control for islanded microgrids?a novel approach," *IEEE Transactions on Power Electronics*, vol. 29, no. 2, pp. 1018–1031, 2014.

[130] J. He and Y. W. Li, "An enhanced microgrid load demand sharing strategy," *IEEE Transactions on Power Electronics*, vol. 27, no. 9, pp. 3984–3995, Sept 2012.

[131] Y. A. R. I. Mohamed and E. F. El-Saadany, "Adaptive decentralized droop controller to preserve power sharing stability of paralleled inverters in distributed generation microgrids," *IEEE Transactions on Power Electronics*, vol. 23, no. 6, pp. 2806–2816, Nov 2008.

[132] T. Ahmad and Z. Miao, "Common mode voltage reduction schemes for voltage source converters in an autonomous microgrid," in *North American Power Symposium (NAPS), 2015*. IEEE, 2015, pp. 1–5.

[133] A. Kahrobaeian and Y. A.-R. I. Mohamed, "Analysis and mitigation of low-frequency instabilities in autonomous medium-voltage converter-based microgrids with dynamic loads," *IEEE Transactions on Industrial Electronics*, vol. 61, no. 4, pp. 1643–1658, 2014.

[134] J. Kim, J. M. Guerrero, P. Rodriguez, R. Teodorescu, and K. Nam, "Mode adaptive droop control with virtual output impedances for an inverter-based flexible ac microgrid," *IEEE Transactions on Power Electronics*, vol. 26, no. 3, pp. 689–701, 2011.

[135] J. He, Y. W. Li, J. M. Guerrero, F. Blaabjerg, and J. C. Vasquez, "An islanding microgrid power sharing approach using enhanced virtual impedance control scheme," *IEEE Transactions on Power Electronics*, vol. 28, no. 11, pp. 5272–5282, 2013.

[136] X. Guo, Z. Lu, B. Wang, X. Sun, L. Wang, and J. M. Guerrero, "Dynamic phasors-based modeling and stability analysis of droop-controlled inverters for microgrid applications," *IEEE Transactions on Smart Grid*, vol. 5, no. 6, pp. 2980–2987, 2014.

[137] W. Yao, M. Chen, J. Matas, J. M. Guerrero, and Z.-M. Qian, "Design and analysis of the droop control method for parallel inverters considering the impact of the complex impedance on the power sharing," *IEEE Transactions on Industrial Electronics*, vol. 58, no. 2, pp. 576–588, 2011.

[138] M. Gao, C. Zhang, M. Qiu, W. Li, M. Chen, and Z. Qian, "An accurate power-sharing control method based on circulating-current power model for voltage-source-inverter parallel system," in *Applied Power Electronics Conference and Exposition (APEC), 2015 IEEE*. IEEE, 2015, pp. 1815–1821.

[139] A. Tazay, Z. Miao, and L. Fan, "Blackstart of an induction motor in an autonomous microgrid," in *Power & Energy Society General Meeting, 2015 IEEE*. IEEE, 2015, pp. 1–5.

APPENDICES

Appendix A Reuse Permissions of Published Papers for Chapters 2 and 3

Appendix A (Continued)

Appendix B List of Abbreviations and Symbols

ac	alternate current
dc	direct current
DER	Distributed Energy Resource
DG	Distributed Generator
HVDC	High Voltage Direct Current
IEEE	Institute of Electrical and Electronics Engineers
IGBT	Insulated-Gate Bipolar Transistor
KVL	Kirchhoff's Voltage Law
KCL	Kirchhoff's Current Law
LCC	Line-Commutated Converters
MATLAB	Matrix Laboratory
PSCAD	Power Systems Computer Aided Design
MPPT	Point of Common Coupling
PV	Photovoltaic
PCC	Point of common coupling.
PID	Proportional-Integral-Differential
PI	Proportional-Integral
PLL	Phase Lock Loop
PQ	Active power/Reactive power
VF	Voltage/Frequency
PWM	Space vector pulse width modulation.
SVPWM	Pulse Width Modulation
SPWM	Sinusoidal pulse width modulation.
HBC	Hybrid boost converter.
DOL	Direct online method.

Appendix B (Continued)

RHP	Right-Half-Plane
LHP	Left-Half-Plane
RLC	Resistor-Inductor-Capacitor
RMS	Root Mean Square
SOC	State of Charge
STATCOM	Static Compensator
VSC	Voltage-Source Converters
FACTS	Flexible ac Transmission Systems
HVDC	High-Voltage direct-current
IM	Induction Motor
SCR	short-circuit ratio
P.U.	Per Unit
DS	Distributed Storages
PHEV	plug-in hybrid vehicle
MMC	modular multilevel converter
IC	Incremental Conductance
PO	Perturb and Observe
HC	Hill Climbing
DOD	depth of discharge
Li-ion	Lithium Ion
CMV	common mode voltage
SCMU	Secondary Central Unit Microgrid
CC-CV	Constant Current-Constant Voltage charging method.

ABOUT THE AUTHOR

Ahmad Tazay was born in 1985 in Jeddah, Saudi Arabia. He obtained his bachelor degree in Electrical Engineering from Umm Al-Qura University, Saudi Arabia in 2007 and his dual masters degree in Master of Science in Electrical Engineering and Master of Science in Engineering Management from University of South Florida, USA in 2013. He received his Ph.D. degree in Electrical Engineering from the University of South Florida in October, 2017. His research interests include: modeling and controlling of smart inverter and VSC, controlling of photovoltaic system based microgrid, stability analysis of microgrids, operation and control of hybrid converter based PV charging station and PHEV, and hardware implementation and controlling of microgrid.